Federico Accornero

Structural Health Monitoring for Preservation and Safeguard of Architectural Cultural Heritage

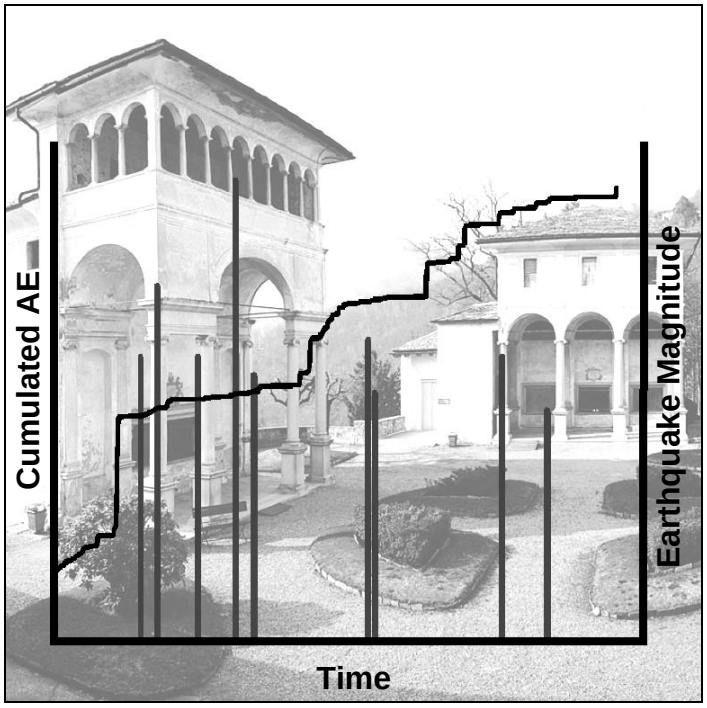

Dottorato di Ricerca in Ingegneria delle Strutture
Politecnico di Torino

Federico Accornero

Structural Health Monitoring for Preservation and Safeguard of Architectural Cultural Heritage

Tesi per il conseguimento del titolo di Dottore di Ricerca
XXVI Ciclo (2011 - 2012 - 2013)

Dottorato di Ricerca in Ingegneria delle Strutture
Politecnico di Torino

December, 2013

PhD in Structural Engineering
Politecnico di Torino, 24 Corso Duca degli Abruzzi, 10129 Turin, Italy

Tutors: Prof. Alberto Carpinteri, Prof. Giuseppe Lacidogna

Coordinator: Prof. Alberto Carpinteri

Summary

The preservation of architectural cultural heritage is a complex problem that requires the use of innovative Structural Health Monitoring (SHM) and non-destructive investigation methodologies to assess the integrity of decorated artworks without altering their state of conservation. A complete diagnosis of crack pattern regarding not only the external decorated surface but also the internal support is of great importance due to the criticality of internal defects and damage phenomena, which may suddenly degenerate into irreversible failures

Objective of the research is to use the Acoustic Emission monitoring to assess the support of the decorated mural surfaces of the Sacred Mountain of Varallo Renaissance Complex (Italy), developing the application aspects of this technique, which has been widely studied from a theoretical and experimental point of view by some Authors in the safeguard of civil and historical buildings.

Moreover, a correlation exists between the regional seismic activity and the AE signals collected during structural monitoring. Therefore, the AET can be also used for the preservation of decorated artworks from the seismic risk.

Then, the assessment of damage by electrical resistance measurements on laboratory mortar specimens and terracotta statues belonging to Chapel XVII of the Sacred Mountain of Varallo experiencing different stress conditions is presented. The evolution of damage based on changing electrical resistance shows agreement with theoretical predictions of continuum damage mechanics. The continuum damage models provide also theoretical support to estimate statues' residual lifetime by correlating in situ electrical resistance measurements with measurements on the laboratory specimens.

Finally, the collapse mechanisms of sculpture and building decoration materials is investigated by means of the Overlapping Crack Model and AE technique. These methods permit to explain the size and slenderness effects on the structural ductility and to show that the energy release during the cracks evolution is a surface-dominated phenomenon.

Sommario

La conservazione del patrimonio architettonico è un problema complesso che richiede l'utilizzo di sistemi di monitoraggio strutturale innovativi e metodologie di indagine non distruttive per valutare l'integrità delle opere d'arte, senza alterare il loro stato di conservazione. Una diagnosi completa del danneggiamento, non solo delle superfici decorate ma anche dei supporti strutturali, è di grande importanza per le criticità che presentano i difetti del materiale da costruzione e per i possibili fenomeni fessurativi, che all'improvviso possono degenerare in collassi irreversibili.
Obiettivo di questa ricerca è utilizzare il monitoraggio tramite la tecnica delle Emissioni Acustiche per valutare lo stato di conservazione del supporto strutturale e delle superfici decorate del Complesso Rinascimentale del Sacro Monte di Varallo, sviluppando gli aspetti applicativi della tecnica AE, studiata dal punto di vista teorico e sperimentale nel campo della salvaguardia di edifici storici e monumentali.
In questo lavoro viene altresì indagata la correlazione tra l'attività sismica regionale ed i segnali di Emissione Acustica raccolti durante il periodo di monitoraggio strutturale: la tecnica AE può infatti essere utilizzata anche per la salvaguardia del patrimonio architettonico nei confronti del rischio sismico.
Inoltre, viene presentata una valutazione del danneggiamento tramite misure di resistenza elettrica effettuate su campioni di malta in laboratorio e sulle statue in terracotta presenti nella Cappella XVII del Sacro Monte di Varallo, sottoposte a diverse condizioni di stress. Il monitoraggio dell'evoluzione del danneggiamento basato sul cambiamento di resistenza elettrica si dimostra in accordo con le previsioni teoriche fornite dalla meccanica del danneggiamento del continuo. I modelli di danneggiamento forniscono infatti un supporto teorico per stimare la vita residua delle statue analizzate, tramite la correlazione delle misure di resistenza elettrica in situ con le misure eseguite sui campioni di laboratorio.
Infine, i meccanismi di collasso di materiali da decorazione e scultorei vengono

indagati mediante l’Overlapping Crack Model e la tecnica di monitoraggio tramite Emissioni Acustiche. Questi metodi consentono di spiegare gli effetti dimensionali della duttilità strutturale e dimostrano che il rilascio di energia durante l'evoluzione del danneggiamento è un fenomeno che si sviluppa principalmente su una superficie.

Contents

Chapter 1

Acoustic Emission Testing

1.1 Structural Health Monitoring (SHM) and Non-destructive Evaluations (NDE)

Structural Health Monitoring (SHM) is a process aimed at providing accurate and in-time information concerning structural health condition and performance. SHM is structure's equivalent of nervous system: Its purpose is to detect unusual structural behaviors in quasi-real-time, indicate the approximate position of problem on the structure, determine the importance of problem, and trigger the safety and remedial actions.

The information obtained from monitoring is generally used to plan and design maintenance activities, increase the safety, verify hypotheses, reduce uncertainty,

and to widen the knowledge concerning the structure being monitored. SHM helps prevent the social, economical, ecological, and aesthetical impact that may occur in the case of structural deficiency, and supports idea of sustainable civil and environmental engineering.

Generally speaking, damage is defined as changes to the material and/or geometric properties of structural systems, including changes to the boundary conditions and system connectivity, which adversely affect the system's performance. A wide variety of highly effective local Non-destructive Evaluation (NDE) tools are available for such monitoring (Balageas, 2010; Boller, 2009; Bruneau and Potel, 2009; Carpinteri and Lacidogna, 2008d).

Non-Destructive Evaluation (NDE) plays a part at several levels in the SHM process of a structure. The part played by the tests is important, and establishing norms and recommendations enables us to ensure a priori rigorous information. Most of the time, in situ measurements are compared to results obtained with reference samples. Some models can also be used to quantify a safety indicator and to compare it to required levels in order to determine the remaining life potential of the structure. It should be noted that, during the measurement, the huge variability of some non-controlled parameters of the material, or of environmental conditions, imposes the need for caution when considering the absolute threshold. Heterogeneity and the variety of flaws or characteristics to estimate generate a widely open set of prospecting techniques. Techniques based on generation and propagation of mechanical waves, so-called acoustic waves, constitute an important part of the NDE applied to building materials.

Non-Destructive Evaluation (NDE) and Non-Destructive Testing (NDT) of materials are set apart by their respective objectives. NDE aims to measure or

characterize certain properties of materials, namely mechanical and/or structural ones. NDT aims to search for and characterize the flaws likely to diminish the mechanical quality, and even to lead to the failure of the material or structure. However, these two fields are deeply linked, as each measurement of property can be used for testing (Bruneau and Potel, 2009).

In NDT, a material or a structure will be considered "healthy" if, during a scanning, the parameters chosen as indicators do not show significant variation with respect to a reference threshold fixed beforehand. In spite of its qualitative nature, this definition of a healthy material is by far the most used by the community of engineers and researchers in NDT. In some cases, this approach is not quite satisfactory, namely in mechanics and in material engineering where more quantitative information are searched and studied because their developments might give judicious information about the micro-structural state and for the healthy state of the material, namely in presence of a diffuse damage. In the frame of health monitoring, NDE can offer more adapted solutions, namely for complex materials such as the composite materials for which the search of reliable testing and evaluation methods are the purpose of intensive researches.

Generally, NDE methods are based on the interaction of a physical field with the material, its micro-structure and the potential flaws it contains. Depending on cases, we can use electromagnetic radiation (Foucault current, microwaves, X-Rays, etc.), or mechanical waves (ultrasound, sound). Acoustic and ultrasonic methods are preferred when the testing concerns some parts of large dimensions or of large thicknesses. Moreover, these waves are intimately related to the elastic properties of the media supporting the propagation. These properties can be identified and followed as a function of the different stresses (mechanical,

hygrothermal, etc). Among these characteristics, the elasticity constants are important data for several mechanical as well as metallurgical reasons.

Moreover, Acoustic Emission Testing (AET), by means of the characteristics that this work allows us to identify, represents a competitive tool of structural health testing and monitoring of structures and materials, namely having been in service for many years. In parallel, recent progress in AET shows that this method allows us to follow, in real time while a part is being stressed, the damage, and to quantitatively and qualitatively characterize these mechanisms (Bruneau and Potel, 2009).

1.2 Acoustic Emission Testing (AET) and Critical Phenomena in Structural Elements

1.2.1 Acoustic Emission and Detection of Crack Evolution in Damaged Structures

The health monitoring of building and construction materials in use for Architectural Cultural Heritage is a necessity today. The goal of an effective health monitoring is to detect and quantify on-site and in laboratory the damage of the material. The methods of health monitoring must also, eventually, lead to the determination of whether the damaged structure must be replaced or can still be used. In the former case, it is necessary to determine its remaining lifetime (Carpinteri and Lacidogna, 2008d).

To reach these objectives, the Acoustic Emission (AE), which corresponds to the elastic energy radiated by the stressed material, has many advantages, in particular

that of being a passive testing mean applicable on structures in use. Figure 1.1 illustrates its principle. However, this very competitive tool for the health monitoring of materials is, most of the time, only used in a qualitative way as a global damaging indicator.

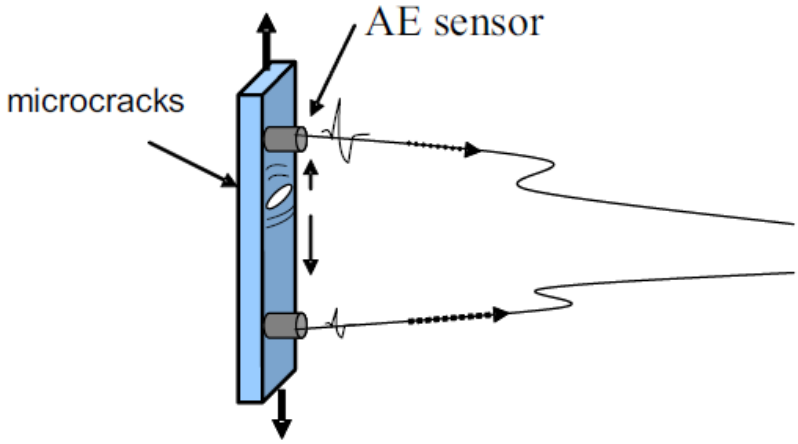

Figure 1.1 – Principle of AET: Stressed material generating an elastic wave.

Then, the current research works on AE are mostly dedicated to the identification and discrimination of damaging mechanisms, and to the estimation of the remaining lifetime of materials and structures, from the relevant parameters extracted from AE signals (Grosse and Ohtsu, 2008; Carpinteri and Lacidogna, 2008d, Bruneau and Potel, 2009).

Most of the analyses of data from acoustical emission are based on a conventional analysis of the temporal parameters such as signal amplitude, energy, count number etc. Figure 1.2 represents a typical AE signal. On these signals, several

parameters can be defined as indicated by RILEM (RILEM, 1986; RILEM, 2010a; RILEM, 2010b; RILEM, 2010c).

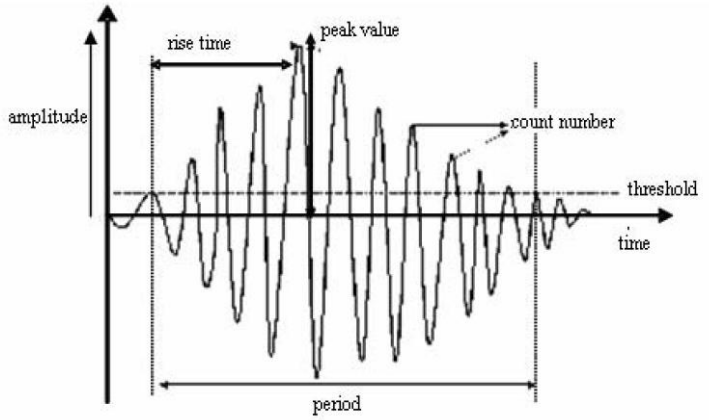

Figure 1.2 – Principal parameters of a discrete burst of AE.

In the following, we will show that a conventional analysis of these parameters enables us to link AE signals to well-identified damages. However, for disordered materials, the identification of damaging mechanisms requires a multivariable analysis of relevant parameters, due to the complexity of the phenomena involved (Carpinteri and Lacidogna, 2008d).

Moreover, in the state-of-the-art of many sectors (terrestrial transport, aerospace, nuclear, civil engineering, etc.), the damage of structural materials is a key point for the mastery of durability and reliability of structures and components in use. If ultrasonic methods are very competitive for the characterization of damage, Acoustic Emission can turn out to be a very efficient quantitative and qualitative method, working in real time, for enabling the identification of damage

mechanisms, using their acoustic signatures (Aggelis, 2011b; Aggelis et al., 2012a; Aggelis et al., 2012d; Aggelis et al., 2012e; Carpinteri et al., 2013c).
Beyond these characterization problems, for which some great steps have been made (Grosse and Ohtsu, 2008; Carpinteri and Lacidogna, 2008d), the problem which appears in the most cases as crucial is the estimation of the remaining lifetime of materials and structures in use. In fact, in order to reach this objective, it is necessary not only to quantify the damage, but also to identify the different precursor mechanisms which are responsible for it and which we can follow on-site (Carpinteri and Lacidogna, 2008d). To answer to this problem, AET methods are very effective, namely because of its capability to follow the damage in real time, and also to detect and characterize precursor events (Carpinteri et al., 2007d; Carpinteri et al., 2013c).

1.2.2 AE Source Location

Acoustic Emissions fall within the class of phenomena in which transient elastic waves are generated by the rapid release of elastic energy by localized sources in material bulk. All building and construction materials, as it is well known, produce AE during the generation and propagation of cracks. Elastic waves propagate through the solid to the surface, where they are detected by AE sensors. Processing these signals, it is possible to get information on the existence and location of AE sources, i.e. where the solid is damaging.
In the most cases, during AE data analysis, the wave propagation speed v is considered as constant in the material and its value is an input data for the resolution of the AE source location problem. So, from the point of view of the

propagation of elastic waves, the solid is seen as an homogeneous and isotropic medium, in which the wave fronts propagate along straight rays, in a similar way to what happens in geometrical optics. It is possible to apply the laws of kinematics of uniform rectilinear motion to describe the propagation of these rays (Lagrange, 1788). The assumptions of point source and of homogeneity (rectilinear propagation) and isotropy (the velocity of propagation is the same in all directions) of the analyzed material make it possible to consider the wavefronts as spherical surfaces.

When a solid has a dominant dimension with respect to the other two, the problem can be reduced as one-dimensional: we consider that the sensors and the source are on the same axis that is the axis of the solid. It is assumed that the source *S* is located between the two sensors S_1 and S_2 as shown in Figure 1.3.

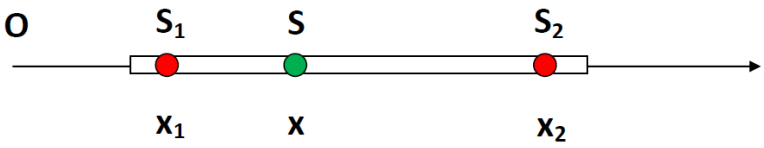

Figure 1.3 – AE source localization: One-dimensional solid, with $x_1 < x < x_2$.

From kinematics, we have:

$$\begin{cases} x - x_1 = v(t_1 - t_0) \\ x_2 - x = v(t_2 - t_0) \end{cases} \tag{1.1}$$

in which *v* is the wave speed. Therefore:

$$x = \frac{1}{2}(x_2 + x_1) - \frac{1}{2}v(t_2 - t_1) \tag{1.2}$$

It is observed, from the latter equation, that the problem of locating the AE source *S* is completely solved if you know the instants of detection of the AE signal by the two sensors, and their positions. Consider now the situation in which the source *S* is located outside of the portion of the solid between the two sensors. Let consider the case $x_1 < x_2 < x$ summarized in Figure 1.4.

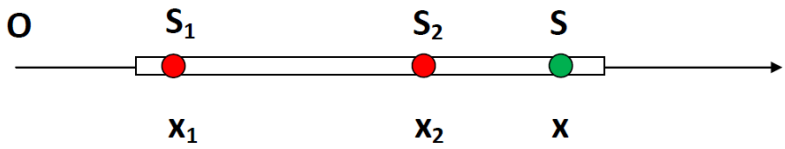

Figure 1.4 – AE source localization: One-dimensional solid, with $x_1 < x_2 < x$.

From kinematics, we have:

$$\begin{cases} x - x_2 = v(t_2 - t_0) \\ x - x_1 = v(t_1 - t_0) \end{cases} \tag{1.3}$$

And, therefore

$$2x = v(t_1 + t_2 - 2t_0) + (x_1 + x_2) \,. \tag{1.4}$$

From the latter equation it can be seen that, unless the instant t_0 of the signal emission is known, the location of the AE source *S* is a problem that admits infinite solutions, compatible with the data of the problem. In other words, it

expresses the obvious fact that x is defined up to an arbitrary additive constant: in fact, if S moves along the axis, the paths that the ray makes to get to the two sensors differ always of the same quantity, for which the relative delay between the instants of detection remains unchanged. It can be concluded that in the one-dimensional case, to locate S is necessary to position the sensors at the ends of the beam, otherwise the solution is indefinite.

To locate AE sources in a thin flat plate, the problem can be represented in two dimensions: the sensors and the source S are lying on the same plane, where the propagation of elastic waves takes place on.

Generally speaking, it is not possible to locate S in the plane if you have the instants of detection of two sensors only. In fact, if plane polar coordinates (r, θ) are used, we have:

$$\begin{cases} r_1 = v(t_1 - t_0) \\ r_2 = v(t_2 - t_0) \end{cases} \tag{1.5}$$

And, therefore

$$r_2 - r_1 = v(t_2 - t_1) = v\Delta t_{21}. \tag{1.6}$$

The experimental data provide Δt_{21} for which you can only obtain the difference r_2 - r_1 of the paths which strike from S sensors. The experimental data can be associated to AE occurred in another place and at a different instant, such that it is still:

$$r_2' - r_1' = v(t_2 - t_0') - v(t_1 - t_0') = v\Delta t_{21}. \tag{1.7}$$

And, therefore

$$r_2^{'} - r_1^{'} = r_2 - r_1 = \cos t \,. \tag{1.8}$$

Recalling that hyperbola is the locus of points on the plane for which constant is the difference of the distances from two fixed points F_1 and F_2, called foci, it follows that the geometric locus on which the source may be compatible with t_2 and t_1 is a hyperbola branch that has to ring the points in which sensors S_1 and S_2 are positioned.

In a plane, the coordinates that identify a point are two, for which you have to set up a system for solving two equations in two unknowns that identify S. So, it is necessary to have two information in terms of time, i.e. the relative delays between the two sensors with respect to a third, taken as reference. The problem, outlined in the following figure, is set in the plane polar coordinates (r, θ):

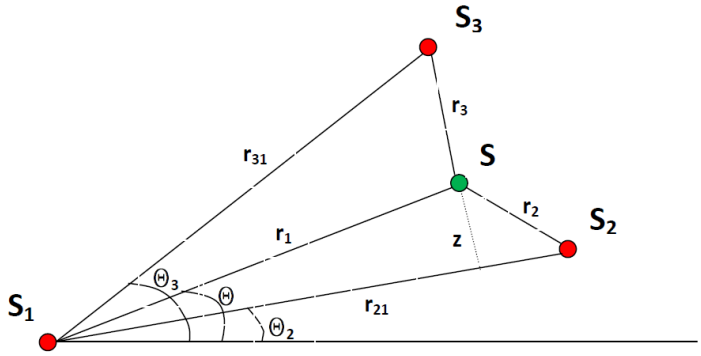

Figure 1.5 – AE source and sensors: Polar coordinates system.

From Figure 1.5, considering the triangle S,S_1,S_2, we have:

$$r_2 - r_1 = v\Delta t_{21}, \tag{1.9}$$

$$z = r_1 \sin(\theta - \theta_2), \tag{1.10}$$

$$z^2 = r_2^2 - [r_{21} - r_1 \cos(\theta - \theta_2)]^2. \tag{1.11}$$

Substituting Eq.(1.10) in Eq.(1.11), we have:

$$r_1^2 = r_2^2 - r_{21}^2 + 2r_{21}r_1 \cos(\theta - \theta_2). \tag{1.12}$$

Eliminating r_2 and taking into account $r_1 = v(t_1 - t_0)$:

$$r_1 = \frac{r_{21}^2 - \Delta t_{21}^2 v^2}{2(\Delta t_{21} v + r_{21} \cos(\theta - \theta_2))}. \tag{1.13}$$

In a similar way, considering the triangle S,S_1,S_3 and taking into account that:

$$r_3 - r_1 = (t_3 - t_1)v = \Delta t_{31} v, \tag{1.14}$$

we have

$$r_1 = \frac{r_{31}^2 - \Delta t_{31}^2 v^2}{2(\Delta t_{31} v + r_{31} \cos(\theta_3 - \theta))}. \tag{1.15}$$

Eqs.(1.13) and (1.15) allow to localize *S*. From the geometric point of view the solution represents the intersection between two branches of two hyperbolas: the first having foci in S_1 and S_2; the second, in S_1 and S_3. The solution is not necessarily unique: that is deductible from the non-linearity of Eqs.(1.13) and (1.15) in r_1 and θ. The problem of double intersections should be addressed on a

case by case basis: the problem goes away when one of the two solutions is physically unacceptable, that is, when it detects a point external to the plane.

If we have AE data from four sensors belonging to a plane, we have the opportunity to write three linearly independent equations with the delays of three sensors compared to the fourth. It sets three linear equations in three unknowns of which two are spatial and one is temporal. Assuming that an AE in S at time t_0 is picked up by the four sensors, the following equations are deduced ($\Delta t_i = t_i - t_0$):

$$\begin{aligned} v^2(\Delta t_1)^2 &= (x-x_1)^2 + (y-y_1)^2 \\ v^2(\Delta t_2)^2 &= (x-x_2)^2 + (y-y_2)^2 \\ v^2(\Delta t_3)^2 &= (x-x_3)^2 + (y-y_3)^2 \\ v^2(\Delta t_4)^2 &= (x-x_4)^2 + (y-y_4)^2 \end{aligned} . \qquad (1.16)$$

from which, by developing the square and subtracting the first equation from the other:

$$\begin{aligned} v^2(\Delta t_1)^2 &= (x-x_1)^2 + (y-y_1)^2 \\ v^2(\Delta t_2)^2 &= (x-x_2)^2 + (y-y_2)^2 \\ v^2(\Delta t_3)^2 &= (x-x_3)^2 + (y-y_3)^2 \\ v^2(\Delta t_4)^2 &= (x-x_4)^2 + (y-y_4)^2 \end{aligned} . \qquad (1.17)$$

Eqs.(1.17) constitute a linear system in the unknowns x, y, Δt_1 that determines the position (x, y) and the instant of emission t_0 of the source S. Note that, due to the linearity of the equations, the position (x, y) is uniquely determined. The critical case is that in which the rank of the coefficient matrix is < 3: in this case the system admits infinite solutions, i.e. the system is indeterminate. Typically critical

cases are the cases in which four sensors are aligned and the case in which three sensors are aligned.

The initial assumptions of homogeneity and isotropy of the material are subjected to some criticism. In fact, the solid homogeneous and isotropic model is an approximation of reality, and the way the waves actually propagate in the material is more similar to that shown in Figure 1.6.

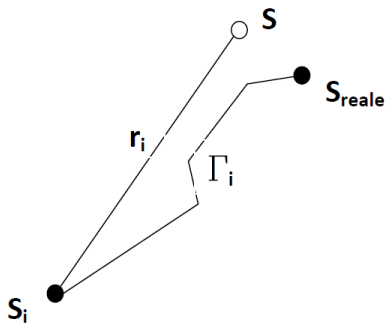

Figure 1.6 – AE wave propagation path model.

This concept is summarized by Eq.(1.18), where Γ_i is the actual path of the beam from the real source S_{reale} to the sensor S_i, u_t it is the local unit vector tangent to Γ_i and r_i is the modulus of the radius vector from the estimated source S to S_i:

$$\int_{\Gamma_i} \vec{u}_T \, d\vec{r} \equiv \int_{\Gamma_i} ds \neq r_i \,. \tag{1.18}$$

In fact, the relationship between the adopted model of homogeneous and isotropic solid and the real solid is the following:

$$\Delta t_i = t_i - t_0 = \int_{\Gamma_i} \frac{ds}{\vec{v}(r)} + m_i = \frac{r_i}{\bar{v}}. \tag{1.19}$$

where m_i is the error that affects the experimental data and v is the propagation speed chosen as constant for the model. Eq.(1.19) has only formal value because both Γ_i and $\vec{v}(r)$, that define exactly the propagation of waves in the solid, remain unknown. Eq.(1.18) still shows that we are unable to determine the exact position of the source: only an approximation is possible.

Moreover, the wave propagation speed is considered as a constant and it is fixed at the beginning of each AE data analysis. So a false estimation of this speed can lead to considerable errors in the AE source localization. Furthermore, even if we have correctly estimated a sort of global average value of wave speed, the described approach could not take into account any local gradients of propagation velocity.

1.2.3 Assessment Scheme for AET

Acoustic Emission (AE) is a non-destructive monitoring method which takes advantage of the elastic energy after crack propagation events (Grosse and Ohtsu, 2008; Carpinteri et al., 2013c). The micro-motion of the tip of the crack excites elastic waves which are acquired by sensors on the surface of the material. The number of recorded signals during loading is connected to the number of active sources within the material (Kurz et al., 2006). Additionally, the signals depend on their source, and specifically the intensity and the mode of fracture. Therefore, key waveform features, like the amplitude, energy and frequency carry information from the damage mode and the fracture process (Shiotani et al., 1994). In general, tensile mode of failure generally develops before shear (Aggelis, 2011b); therefore, the characterization of cracks as to their mode provides a warning before failure. The received wave depends on the motion of the crack tip, as well as on the orientation of the crack relatively to the receivers and the distance between the cracking source and the sensor. When a cracking event occurs, all possible wave modes (longitudinal, transverse and Rayleigh if the crack is surface breaking) are excited. A tensile cracking incident (Fig.1.8) excites most of the energy in the form of longitudinal waves. Therefore, most of the energy arrives in the initial part of the acquired waveform since longitudinal waves are the fastest type. When shear cracking occurs, the percentage of energy emitted in the shear wave mode is increased resulting in a delay of the main energy cycles of the waveform. This leads in a long Rise Time (*RT*), and quite low rise angle of the waveform, see Fig.1.8 (Aggelis, 2011b; Carpinteri et al., 2013c). AE duration is the time delay between the first and last threshold crossings. Amplitude, *A* is the maximum voltage of the waveform, as seen again in Fig.1.8 and *AE energy* is the area under

the rectified signal envelope. Some frequency features of interest, derived after fast Fourier transformation of the signals are the Central Frequency (*CF*) and the Peak Frequency (*PF*). Central Frequency is the centroid of the spectrum while *PF* is the frequency with the highest magnitude (Aggelis and Matikas, 2012c).

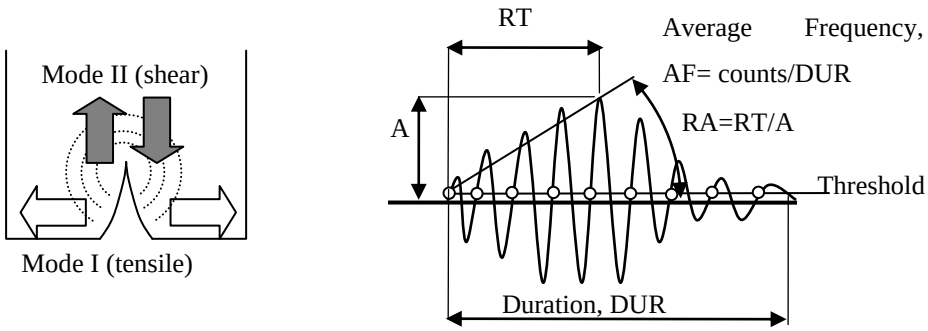

Figure 1.8 – Cracking modes and typical AE signals.

The applicability of the above mentioned points depends on the geometric conditions, orientation of the cracks and the heterogeneity of the medium. In laboratory scale, it has been shown that damage characterization can be conducted with relative success (Aggelis et al., 2012f; Carpinteri et al., 2008b). However, the expansion of the laboratory criteria to real structures is not easy mainly due to geometry factors and the texture of the material (Scholey et al., 2010). These factors prevent from general application and make the combined study of AE and elastic wave propagation necessary in an effort to quantify the distortion effect on the waveform features. In some works (Carpinteri et al., 2013c) mortar specimens are fractured in three point bending and the AE behavior is recorded by two sensors at different locations from the crack. The results show that the change in

the waveform features is quite strong in terms of frequency and energy and should not be neglected from any characterization approach.

As it emerges from the abovementioned work, attenuation properties of AE waves in non homogeneous materials such as mortar and concrete −but this concept can also be easily extended to other quasi-brittle materials like rocks− influence critical AE parameters. Hence, taking into account the attenuation and distortion phenomena in the travel path between the source of the signal and the sensor, in order to apply these theories it should be ensured that the measuring system is able to detect the most relevant AE events reflecting the cracking process of the material. Higher frequency components propagate in quasi-brittle materials with a greater attenuation. Based on experimental results on mortar and concrete, if the wavelength is larger than the maximum inhomogeneity, the wave "passes over" without significant modifications in its waveform (Landis and Shah, 1995). In general, for a measuring area at a distance of 10 m from the sensor, only AE waves with frequency components lower than 100 kHz are detectable. Therefore, the employed AE sensors, and the volume of material analyzed should take into account these limitations. In other words, it is necessary to employ broadband or resonant sensors, with the right amplification, depending on the size and the damage level of the monitored structure (Grosse and Ohtsu, 2008).

Starting from these considerations, two different approaches are proposed to obtain indirect estimation of the physical fractal dimension of the damage domain up to the peak load of quasi-brittle materials, such as concrete and rocks. First, an energy density approach is presented, based on the size-effects of the energy release determined by the AE technique. Then, a complementary method is proposed, based on the *b*-value analysis of AE events (Scholz, 1968). Since the *b*-

value is size-independent, its evaluation evidences the similarity between the damage process in a structure and the seismic activity in a region of the Earth crust (Scholz, 1968). Finally, by considering the described methods, an effective AET Assessment Scheme can be proposed (Fig.1.8).

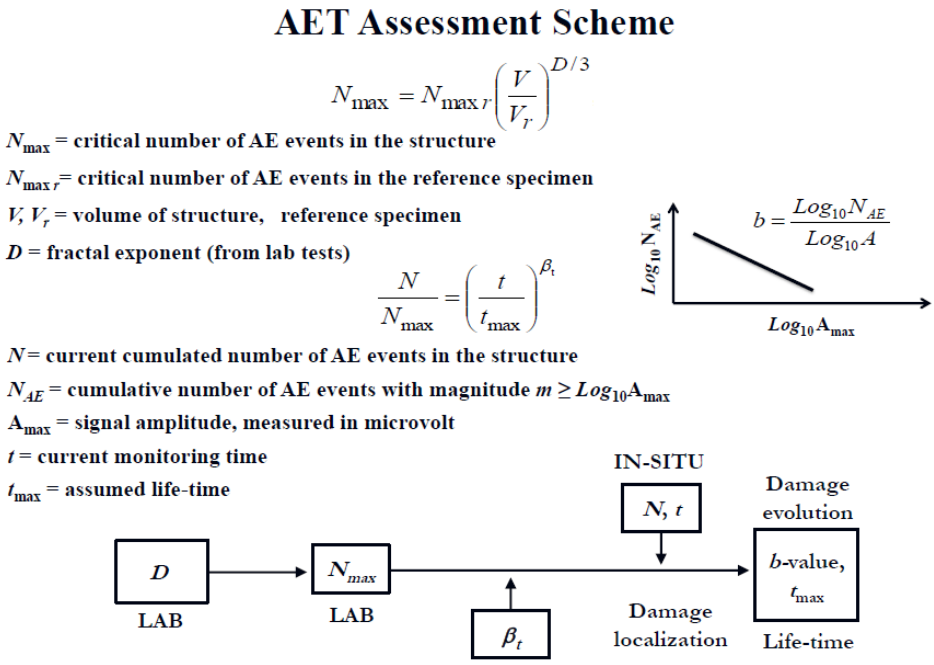

Figure 1.7 – Assessment Scheme for AET.

1.2.4 Energy Density Criterion

Acoustic Emission data have been interpreted by means of statistical and fractal analysis, considering the multiscale aspect of cracking phenomena (Carpinteri et al., 2007d). Consequently, a multiscale criterion to predict the damage evolution has been formulated. Recent developments in fragmentation theories (Carpinteri et al., 2002) have shown that the energy W during microcrack propagation is dissipated over a fractal domain comprised between a surface and the specimen volume V.

The following size-scaling law has been assumed during the damage process:

$$W \propto N \propto V^{D/3}. \tag{1.20}$$

In Eq.(2.1) D is the so-called fractal exponent comprised between 2 and 3, and N is the cumulative number of AE events that the structure provides during the damage monitoring.

Some Authors have also shown that energy dissipation, as measured with the AE technique during the damaging process, follows the time-scaling law (Carpinteri et al., 2005):

$$W \propto N \propto t^{\beta_t}, \tag{1.21}$$

where β_t is the time-scaling exponent for the dissipated energy in the range (0, 3) and N is the number of AE events.

By working out the exponent β_t from the data obtained during the observation period, we can make a prediction on the structure's stability conditions: if $\beta_t < 1$ the structure evolves toward stability conditions; if $\beta_t \approx 1$ the process is metastable; if $\beta_t > 1$ the process is unstable.

1.2.5 Statistical Distribution of AE Events

A statistical interpretation to the variation in the *b*-value during the evolution of damage detected by AE has been proposed, which is based on a treatment originally proposed by Carpinteri and co-workers (Carpinteri, 1994; Carpinteri et al., 2008b). The proposed model captures the transition from the condition of diffused criticality to that of imminent failure localisation.

By analogy with seismic phenomena, in the AE technique the magnitude may be defined as follows:

$$m = Log_{10} A_{max} + f(r), \tag{1.22}$$

where A_{max} is the amplitude of the signal expressed in volts, and *f(r)* is a correction factor taking into account that the amplitude is a decreasing function of the distance *r* between the source and the sensor.

In seismology the empirical Gutenberg-Richter's law (Richter, 1958):

$$Log_{10} N(\geq m) = a - bm, \text{ or } N(\geq m) = 10^{a-bm}, \tag{1.23}$$

expresses the relationship between magnitude and total number of earthquakes with the same or higher magnitude in any given region and time period, and it is the most widely used statistical relation to describe the scaling properties of seismicity. In Eq. (1.23), *N* is the cumulative number of earthquakes with magnitude ≥ *m* in a given area and within a specific time range, whilst *a* and *b* are positive constants varying from a region to another and from a time interval to another. Equation (1.23) has been used successfully in the AE field to study the scaling laws of AE wave amplitude distribution. This approach evidences the

similarity between structural damage phenomena and seismic activities in a given region of the Earth's crust, extending the applicability of the Gutenberg-Richter's law to Structural Engineering. According to Eq. (1.23), the *b*-value changes systematically at different times in the course of the damage process and therefore can be used to estimate damage evolution modalities.

Equation (1.23) can be rewritten in order to draw a connection between the magnitude *m* and the size *L* of the defect associated with a AE event. By analogy with seismic phenomena, the AE crack size-scaling entails the validity of the relationship:

$$N(\geq L) = cL^{-2b}, \tag{1.24}$$

where *N* is the cumulative number of AE events generated by source defects with a characteristic linear dimension $\geq L$, *c* is a constant of proportionality, and $2b = D$ is the fractal dimension of the damage domain.

It has been evidenced that this interpretation rests on the assumption of a dislocation model for the seismic source and requires that $2.0 \leq D \leq 3.0$, i.e., the cracks are distributed in a fractal domain comprised between a surface and the volume of the analysed region (Turcotte, 1997; Rundle et al., 2003).

The cumulative distribution (1.24) is substantially identical to the cumulative distribution proposed by Carpinteri (Carpinteri, 1994), which gives the probability of a defect with size $\geq L$ being present in a body:

$$P(\geq L) \propto L^{-\gamma}. \tag{1.25}$$

Therefore, the number of defects with size ≥ L is:

$$N^*(\geq L) = cL^{-\gamma}. \tag{1.26}$$

where γ is a statistical exponent measuring the degree of disorder, i.e. the scatter in the defect size distribution, and c is a constant of proportionality. By equating distributions (1.24) and (1.26) it is found that: $2b = \gamma$. At the collapse, the size of the maximum defect is proportional to the characteristic size of the structure. As shown by Carpinteri and co-workers (Carpinteri et al., 2008b), the related cumulative defect size distribution (referred to as self-similarity distribution) is characterized by the exponent $\gamma = 2.0$, which corresponds to $b = 1.0$. It was also demonstrated by Carpinteri (Carpinteri et al., 2008b) that $\gamma = 2.0$ is a lower bound which corresponds to the minimum value $b = 1.0$, observed experimentally when the load bearing capacity of a structural member has been exhausted.

Therefore, by determining the b-value it is possible to identify the energy release modalities in a structural element during the monitoring process. The extreme cases envisaged by Eq. (1.20) are $D = 3.0$, which corresponds to the critical condition $b = 1.5$, when the energy release takes place through small defects homogeneously distributed throughout the volume, and $D = 2.0$, which corresponds to $b = 1.0$, when energy release takes place on a fracture surface. In the former case diffused damage is observed, whereas in the latter two-dimensional cracks are formed leading to the separation of the structural element.

1.2.6 Regional Seismicity and AE Structural Monitoring

Among the various studies on the earthquakes space-time correlation, there is a statistical method that allows to calculate the degree of correlation both in space and time between a series of AE and the local seismic recordings, collected in the same period. This analysis is based on the generalization of the space-time correlation known as the integral of Grassberger-Procaccia (Grassberger and Procaccia, 1983), defined as follows:

$$C(r,\tau) \equiv \frac{1}{N_{EQ}N_{AE}} \sum_{k=1}^{N_{EQ}} \sum_{j=1}^{N_{AE}} \Theta(r - |x_k - x_j|)\Theta(\tau - |t_k - t_j|) \quad , \tag{1.26}$$

where N_{AE} is the number of peaks of AE activity registered in site, and in a defined time window, N_{EQ} is the number of earthquakes recorded in the surrounding area during the same time window, and Θ is the step function of Heaviside ($\Theta(x) = 0$ if $x \le 0$, $\Theta(x) = 1$ if $x > 0$). The index k refers to the recorded seismic events $\{x_k, t_k\}$, while the index j refers to the recorded AE events $\{x_j, t_j\}$.

Therefore, between all possible pairs of recorded AE and seismic events, the sum expressed by the integral of Grassberger-Procaccia can be calculated for those having the epicentral distance $|x_k - x_j| \le r$ and the temporal distance $|t_k - t_j| \le \tau$.

Hence, $C(r,\tau)$ is the probability of occurrence of two events, an earthquake and an AE event, whose mutual spatial distances are smaller than r and mutual temporal distances are smaller than τ.

Note that, in order to evaluate Eq.(1.26), the numbers of N_{AE} and N_{EQ} are not required to assume the same value, and that x_j correspond to the geographic

position of the monitoring site.

Anyway, this approach does not consider the chronological order of the two types of event. Since the AE time series and the earthquake sequences are closely intertwined in the time domain, the problem of the predictive ability of the AE peaks is still open. The records of AE could be both the consequences of the progressive development of micro damage, or the effect of widespread micro-seismicity. Therefore, a probabilistic analysis can be carried out discriminating between the AE events prior to the earthquake, which are precursors, and the AE following the earthquake, which are aftershocks. This analysis can be performed adopting a modified correlation integral (Carpinteri et al., 2007c):

$$C_{\pm}(r,\tau) \equiv \frac{1}{N_{EQ}N_{AE}} \sum_{k=1}^{N_{EQ}} \sum_{j=1}^{N_{AE}} \Theta\left(r - \left|x_k - x_j\right|\right) \Theta\left(\tau - \left|t_k - t_j\right|\right) \Theta\left(\pm\left(t_k - t_j\right)\right), \qquad (1.27)$$

where "+" and "−" in the Heaviside function are used to take into account that the AE events could be respectively seismic precursors and aftershocks.

In this way, the function $C^{+}(r, \tau)$ gives the probability that a peak of AE, detected at a certain time, will be followed by an earthquake in the subsequent days within a radius of r kilometers from the AE monitoring site. Varying the thresholds r and τ in Eq. (1.27), two cumulative probability distributions can been constructed, one for each condition (sign "+" or "−") and then the corresponding probability density functions can been derived and represented.

Chapter 2

Case Study: SHM of the Sacred Mountain of Varallo Renaissance Complex

2.1 Introduction: The RE-FRESCOS Project

The project RE-FRESCOS "Preservation, Safeguard and Valorisation of Masonry Decorations in the Architectural Historical Heritage of Piedmont" has found in the Sacri Monti of Piedmont in Italy (belonging to the UNESCO World Heritage List since 2003) different case-histories where develop joint multidisciplinary researches. The idea was that the proposed analysis could assume a key role for preservation and maintenance of these monuments.

The research activity was conducted by different subjects: the Politecnico di Torino, the National Research Institute of Metrology (INRiM), and involving the Special Natural Reserve of the Sacro Monte di Varallo as co-proponent.

In actuality, public awareness of the need to preserve, protect and enhance the Historical Heritage, on account of its intrinsic cultural value and its relevance to

environmental concerns, is a well-established fact.

While the devastating, irreversible damage wrought by inappropriate intervention methods are right under our eyes, the experience acquired over a quarter of a century of strengthening and restoration works has led to the following conclusions:

(a) Repair and restoration interventions must be conducted on the basis of careful investigations into the composition of the materials, construction history, deterioration mechanisms.

(b) The investigation must focus on the relationships and interactions between the decorative apparatus and the supporting masonry, the microclimate and the soil in direct contact with the structure.

(c) In Piedmont, as anywhere, it is possible to identify a multiplicity of local practices in terms of masonry construction, finishing and decoration methods that are able to make use of local materials and resources.

(d) Each local technique gives rise to special problems of compatibility with some of the integration and bonding systems to be adopted.

(e) In designing rehabilitation and restoration works it is necessary to resort to systems that have been specifically tested for compatibility, durability, and, possibly, reversibility.

The co-proponent laboratories of the Politecnico di Torino and the National Research Institute of Metrology (INRiM), by conducting the research activities related to this project, developed integrated investigation, using non invasive methods, specially designed for dealing with the highly diversified historic heritage of Piedmont, with the aim to remedy current shortcomings in the identification of effective and compatible restoration and maintenance techniques.

The physical-chemical decay and the damage evolution of materials constituting the decorated surfaces and the support were found caused by infiltrations of water, thermo-elastic stresses, or seismic and environmental vibrations. The physical-chemical degradation was dealt by Materials Science and Chemical Engineering techniques.

The stability of the decorated surfaces was investigated by innovative Structural Health Monitoring (SHM) with Acoustic Emission (AE) and ultrasonic methods already experimentally tested in the field of artistic and monumental Italian cultural heritage. The ultrasonic investigation techniques allowed to assess separations, defects and damage phenomena regarding the decorated surfaces and the masonry supports. Innovative SHM and acoustic methods allowed to distinguish a well preserved artwork in comparison to a damaged one.

The data collected during the experimental tests conducted in situ were interpreted with Fracture Mechanics models and methodologies.

Finally, the research activity has shown how the design of the most appropriate technique turns out to be crucial as well as the selection of the most suitable repair products in terms of durability and compatibility. The duration of the Project was 36 months.

The project was divided in 6 Work Packages, the WPs Leaders are Professors and Researchers of the Politecnico di Torino and Researchers of INRiM; in each work phase, Researchers of the different Departments are involved. The WP indication is listed in the following:

- WP1) Characterization of historical surface finishing and execution techniques. Study of materials and their mixing ratios. Definition of specific interventions.

- WP2) Damage analysis of decorated surface structural support by Structural Health Monitoring (SHM) with Acoustic Emission Technique (AET).

- WP3) On site monitoring of mural decorative artworks using advanced ultrasonic techniques - Laboratory prequalification of injection grouts to be used in repair works.

- WP4) Upgrading and recovery of mural painting assets in Piedmont: the problem of reliability and durability of the media.

- WP5) Analysis of debonding phenomena in decorated mural elements by numerical models based on Fracture Mechanics.

- WP6) Dissemination and diffusion of the results.

The aim of the WP2 "Damage analysis of decorated surface structural support by the Acoustic Emission technique" is to reveal by means of the Acoustic Emission Technique (AET) the damage evolution in the support of the decorated surfaces of the Sacred Mountain of Varallo. In particular, the data coming from the "in situ" monitoring of the Chapel XVII, hosting "The Transfiguration of Christ on Mount Tabor", were utilized in order to preserve the artworks from seismic risk and eventual collapses due to earthquake actions.
A complete diagnosis of crack pattern regarding not only the external decorated surface but also the internal support is of great importance due to the criticality of

internal defects and damage phenomena, which may suddenly degenerate into irreversible failures.

2.2 The Sacred Mountain of Varallo

2.2.1 History

The Sacro Monte of Varallo architectural complex (Varallo Sesia, Italy) is the work of two great churchmen and of a number of artists headed by Gaudenzio Ferrari (Fig.2.1). The two churchmen are: the Franciscan friar, Blessed Bernardino Caìmi, and St. Charles Borromeo, Archbishop of Milan. At Varallo Fra Bernardino Caìmi put into practice the idea that he had been turning over in his mind during his stay in the Holy Land (Alessi, 1974; De Filippis, 2009).

His aim was to erect buildings that would recall the "holy places" of Palestine (Fig.2.2), those places which evoke the characteristic monuments of Christ's stay on earth (the Stable at Bethlehem, the House in Nazareth, the Last Supper, Calvary and the Holy Sepulchre). He began his work in 1491 and carried on with it as long as he lived (i.e. until the end of 1499), assisted by Gaudenzio Ferrari who continued the idea and decorated a number of chapels with frescos and statues (Fig.2.3).

St. Charles Borromeo appreciated the work already done when he paid a visit to the Sacro Monte in 1578 and, giving the place the appropiate name of "New Jerusalem", made it more widely known among his contemporaries. Returning there at the end of October 1584, he decided to develop the idea by building new chapels which would illustrate the work of Jesus more completely.

For the great Bishop of Milan it was an effective means of his time, giving them greater religious fervour and protecting them from the heresies that threatened northern Italy. He utilised the project for the rearrangement of the Sacro Monte drawn up by Galeazzo Alessi in 1592 and, adapting it to his own plan, gave instructions for the resumption of work.

The work continued until 1765. During this century and a half new artists added their names to Gaudenzio Ferrari's: Morazzone, Tanzio, the Fiamminghini and the Danedi where painting was concerned; Giovanni d'Enrico and Tabacchetti for sculputure, to mention only the most noted of them (Fig.2.3). St. Charles Borromeo's idea and the efforts which derived from it made the Sacro Monte of Varallo the prototype of those other Sacri Monti that arose in the area during the 17th Century (Sacri Monti of Orta, Varese, Oropa, Crea and Locarno).

Today the Sacro Monte of Varallo continues to be a school of Christian thruth and life, while at the same time it is the most precious treasury of art in Valsesia.

Figure 2.1 – The Sacred Mountain of Varallo, Italy: View.

Figure 2.2 – The Sacred Mountain of Varallo, Italy: Square of Tribunals.

Figure 2.3 – The Sacred Mountain of Varallo, Italy: Chapel 33, *Ecce Homo*, by Pier Francesco Mazzucchelli called "Il Morazzone" and Giovanni d'Enrico.

2.2.2 Chapel XVII: The Transiguration of Christ on Mount Tabor

This chapel (Fig.2.4), object of the present AET monitoring, houses the scene of the Transfiguration of Christ, who appeared to the Apostles at the foot of the Mount Tabor, in radiant light between Elijah and Moses; the apostles then perform miracles (Fig.2.5).

This stage of the narrative and the relative chapel were also foreseen in the *Book of Mysteries* by Galeazzo Alessi 1565-1569 (Alessi, 1974), from which the group of sculptures located high on the mountain takes its inspiration. The relative foundations were already begun in 1572, but the chapel was not completed until the 1660s.

The statues are attributed to Pietro Francesco Petera of Varallo and to Giovanni Soldo of Camasco (about 1670s), whilst the frescoes (about 1666-1675) are the work of the brothers Montaldo, known as “I Danedi”, also responsible for the decoration of the cupola of the Basilica of Sacro Monte of Varallo.

Figure 2.4 – The Sacred Mountain of Varallo, Italy: Chapel 17.

Figure 2.5 – The Sacred Mountain of Varallo, Italy: Chapel 17, *The Transfiguration of Christ on Mount Tabor*, frescoes by brothers Montaldo called "I Danedi.

Figure 2.6 – The Sacred Mountain of Varallo, Italy: Chapel 17, *The Transfiguration of Christ on Mount Tabor*, statues by Pietro Francesco Petera of Varallo, and Giovanni Soldo of Camasco.

2.3 Cultural Heritage and its Preservation

The preservation of architectural cultural heritage is a complex problem that requires the use of innovative Structural Health Monitoring (SHM) and non-destructive investigation methodologies to assess the integrity of decorated artworks without altering their state of conservation. A complete diagnosis of crack pattern regarding not only the external decorated surface but also the internal support is of great importance due to the criticality of internal defects and damage phenomena, which may suddenly degenerate into irreversible failures (Carpinteri et al., 2009b; Carpinteri et al., 2009c; Carpinteri et al., 2010b).

A great deal of NDE techniques is introducing some type of energy into the system to be analyzed. On the contrary, in AET tests, the input is the mechanical energy release generated by the material itself during the damage evolution, so that no perturbation is induced and the integrity of the system may be guaranteed. By monitoring the support of a decorated surface by means of the AET, it becomes possible to detect the occurrence and evolution of surface vs support separation and of stress-induced cracks.

Cracking in fact is accompanied by the emission of elastic waves, which propagate through the bulk of the material. These waves can be received and recorded by piezoelectric (PZT) transducers applied to the external surface of the artwork support.

Objective of the research is to use the AET to assess the support of the decorated mural surfaces, developing the application aspects of this technique, which has been widely studied from a theoretical and experimental point of view by some Authors in the safeguard of civil and historical buildings (Carpinteri et al., 2009d; Carpinteri et al., 2011b; Carpinteri et al., 2011c; Carpinteri et al., 2012b; carpinteri et al., 2008a; Lacidogna et al., 2013b; Niccolini et al., 2013a; Niccolini et al., 2013b; Occhi Villavecchia, 2013). In a first stage, it is essential to recognize the artwork to be monitored, its conservation state and the severity of its conditions at the beginning of the monitoring and restoration processes. The AET makes it also possible to predict and localize the presence of cracks and analyze the damage evolution in supports such as decorated masonry wall and vaults (Carpinteri et al., 2007d).

The research activity will focus on methods aimed at the localization and quantification of Acoustic Emission sources in the structural support of decorated

surfaces. These highly advanced procedures are also used in seismology, where the seismic moment is a parameter directly correlated with fracture problems in Earth's crust. To this purpose, a computer-based procedure including the AE source location algorithm is adopted. The procedure can perform automatic AE data processing by means of dedicated software. The final output of the code returns a complete decription of the decorated surface preservation state, giving precise information about the damage characterization and evolution of the support stability. In addition, during the research activity, the AET monitoring is fine tuned for the use of an automated working procedure.

In a common case, a huge structure can be monitored by means of sensors of new type, using wireless transmission systems and efficient algorithms for processing large amount of data. Thus it is possible to use a centralized station to control continuously, simultaneously, and in real time, individual decorated surfaces, possibly situated in different locations.

A correlation exists between the regional seismic activity and the AE signals collected during structural monitoring. Therefore, the AET can be also used for the preservation of decorated artworks from the seismic risk. In this framework, the AE collected on sensor networks installed during the activity, can be directly connected to regional center for the environomental forecast and monitoring.

2.4 AET Monitoring Setup

2.4.1 Structural Conditions of Chapel XVII

The object of AET monitoring is Chapel XVII of the Sacred Mountain of Varallo, hosting "The Transfiguration of Christ on Mount Tabor". As regards the structural integrity, Chapel XVII shows a vertical crack of about 3.00 m in length and a detachment of frescos both on the North wall, which are the object of the present monitoring campaign by means of AE. Structural health conditions of Chapel XVII are synthesized in the schedule below, drown up by Emanuele Giletti on April 2009 (Fig.2.7). Six AE sensors are employed to monitor the damage evolution of the structural support of the decorated surfaces of the Chapel XVII: four are positioned around the vertical crack while two are positioned near the frescos detachment (Fig.2.8a,b). For the sensor pasting on decorated surfaces, a suitable methodology is applied. Moreover, Chapel XVII shows another vertical crack on the South wall, symmetric to the previous one with respect to the pronao of the building (Fig. 2.7).

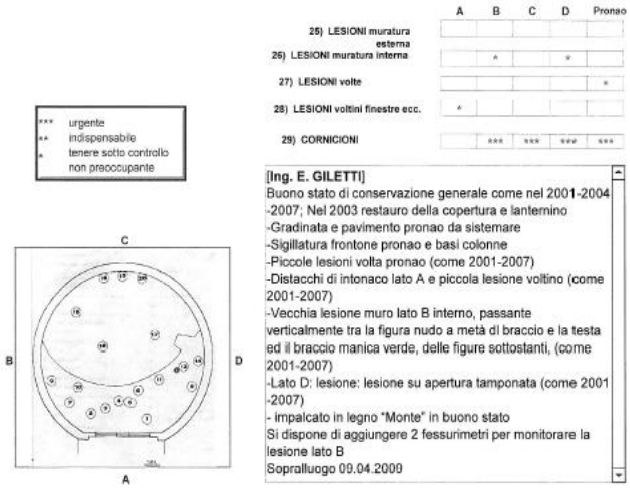

Figure 2.7a – The Sacred Mountain of Varallo, Italy: Chapel 17, structural health conditions schedule (Giletti, 2009).

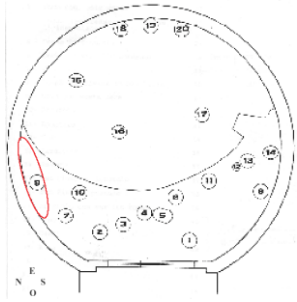

Figure 2.7b – The Sacred Mountain of Varallo, Italy: Chapel 17, monitoring region.

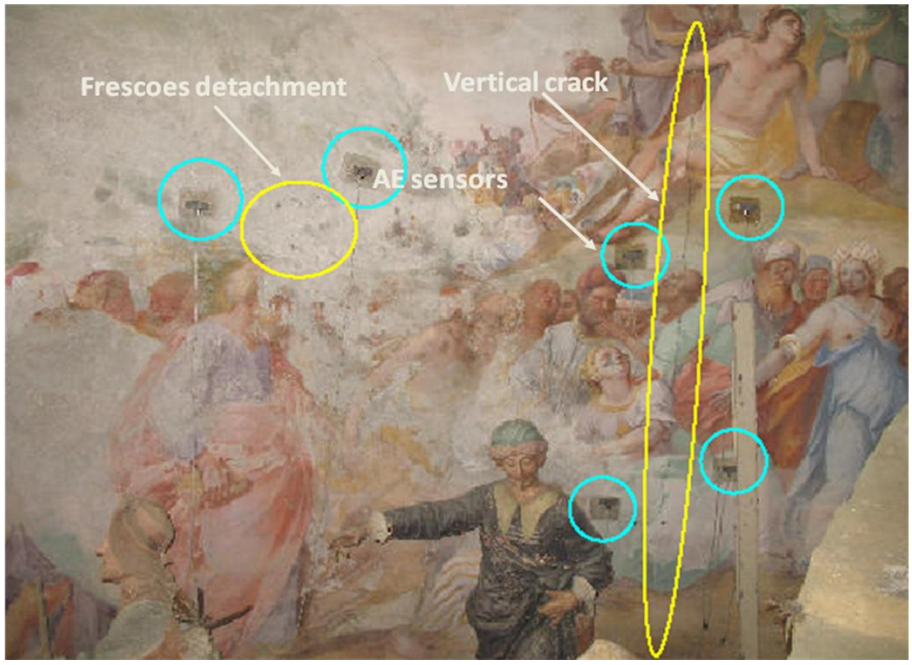

Figure 2.8 – The Sacred Mountain of Varallo, Italy: Chapel 17, North wall, view of the monitored area. Left side: Frescoes detachment monitored by two sensors. Right side: Vertical crack monitored by four sensors.

2.4.2 Monitoring Equipment and Sensor Positioning

The equipment used for signal acquisition and processing consists of six USAM units (Fig.2.9). Each of these units analyses in real time, and transmits to a PC, all the characteristic parameters of an ultrasonic event. In this manner, each AE event is identified by a progressive number and characterised by a series of data giving the amplitude and time duration of the signal and the number of oscillations (Fig.2.10). Moreover, the absolute acquisition time and signal frequency are also given, so that, through an analysis of signal frequency and time of arrival at the

transducers, it is possible to identify the group of signals belonging to the same AE event and to localise it. Each unit is equipped with a pre-amplified wide-band piezoelectric sensor (PZT), which is sensitive in a frequency range between 50 kHz and 800 kHz. The signal acquisition threshold can be set in a range between 100 μV and 6.4 mV.

Within the RE-FRESCOS Project −Preservation, Safeguard and Valorisation of Masonry Decorations in the Architectural Historical Heritage of Piedmont− AE sensors positioning is carried out from March 30 until April 6, 2011.

In particular, on the monitoring areas of the decorated masonry walls, protective films made of washi (obtained from fibers of the bark of the "gampi" tree) are placed by expert restorers (Fig.2.11). The protective films are covered by a coat of "Paraloid" (Fig.2.12) and then the AE sensors are positioned.

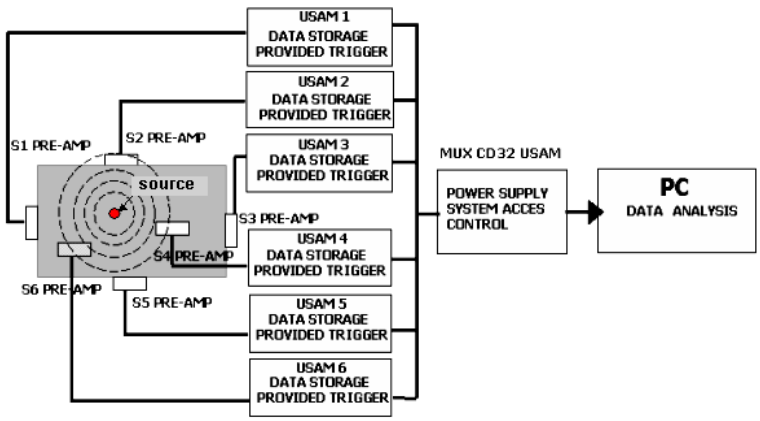

Figure 2.9 – AE data acquisition system - USAM units.

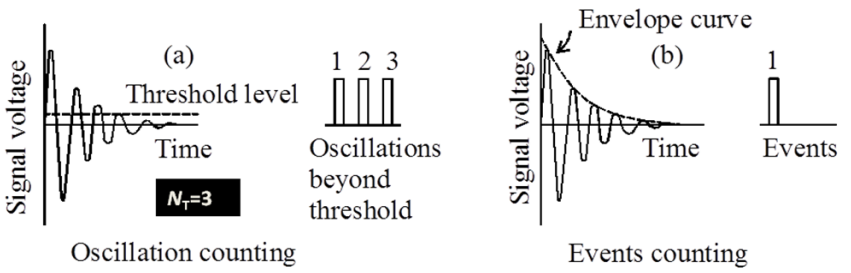

Figure 2.10 – AE counting method: The event intensity is measured by the oscillation number N_T. The oscillation number N_T increases with the signal amplitude.

Figure 2.11 – AE sensor positioning on decorated surfaces.

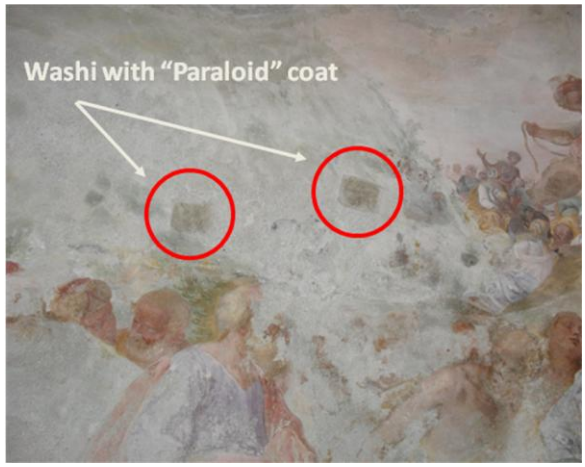

Figure 2.12 – AE sensor positioning: Washi Paper with Paraloid coat.

2.5 Data Acquisition and Analysis

The monitoring period of the structural supports of the chapel began on April 28, 2011 and ended September 5, 2011. The AE collected data are grouped into two different time windows. The first time window started May 9, 2011 and finished June 16, 2011. The second time window started July 5, 2011 and finished September 5, 2011. Both time windows involved the monitoring of the vertical crack and of the frescos detachment. The results obtained by the application of the AE sensors are presented in the following.

Acoustic Emission data have been interpreted by means of statistical and fractal analysis, considering the multiscale aspect of cracking phenomena (Carpinteri et al., 2007d). Consequently, a multiscale criterion to predict the damage evolution has been formulated. Recent developments in fragmentation theories (Carpinteri et

al., 2002) have shown that the energy W during microcrack propagation is dissipated over a fractal domain comprised between a surface and the specimen volume V.

The following size-scaling law has been assumed during the damage process:

$$W \propto N \propto V^{D/3}. \tag{2.1}$$

In Eq.(2.1) D is the so-called fractal exponent comprised between 2 and 3, and N is the cumulative number of AE events that the structure provides during the damage monitoring.

Some Authors have also shown that energy dissipation, as measured with the AE technique during the damaging process, follows the time-scaling law (Carpinteri et al., 2005):

$$W \propto N \propto t^{\beta_t}, \tag{2.2}$$

where β_t is the time-scaling exponent for the dissipated energy in the range (0, 3) and N is the number of AE events.

By working out the exponent β_t from the data obtained during the observation period, we can make a prediction on the structure's stability conditions: if $\beta_t < 1$ the structure evolves toward stability conditions; if $\beta_t \approx 1$ the process is metastable; if $\beta_t > 1$ the process is unstable.

Moreover, a statistical interpretation to the variation in the b-value during the evolution of damage detected by AE has been proposed, which is based on a treatment originally proposed by Carpinteri and co-workers (Carpinteri, 1994; Carpinteri et al., 2008b). The proposed model captures the transition from the condition of diffused criticality to that of imminent failure localisation.

By analogy with seismic phenomena, in the AE technique the magnitude may be defined as follows:

$$m = Log_{10} A_{max} + f(r), \tag{2.3}$$

where A_{max} is the amplitude of the signal expressed in volts, and *f(r)* is a correction factor taking into account that the amplitude is a decreasing function of the distance *r* between the source and the sensor.

In seismology the empirical Gutenberg-Richter's law (Richter, 1958):

$$Log_{10} N(\geq m) = a - bm, \text{ or } N(\geq m) = 10^{a-bm}, \tag{2.4}$$

expresses the relationship between magnitude and total number of earthquakes with the same or higher magnitude in any given region and time period, and it is the most widely used statistical relation to describe the scaling properties of seismicity. In Eq. (2.4), *N* is the cumulative number of earthquakes with magnitude $\geq m$ in a given area and within a specific time range, whilst *a* and *b* are positive constants varying from a region to another and from a time interval to another. Equation (2.4) has been used successfully in the AE field to study the scaling laws of AE wave amplitude distribution. This approach evidences the similarity between structural damage phenomena and seismic activities in a given region of the Earth's crust, extending the applicability of the Gutenberg-Richter's law to Structural Engineering. According to Eq. (2.4), the *b*-value changes systematically at different times in the course of the damage process and therefore can be used to estimate damage evolution modalities.

Equation (2.4) can be rewritten in order to draw a connection between the magnitude *m* and the size *L* of the defect associated with a AE event. By analogy

with seismic phenomena, the AE crack size-scaling entails the validity of the relationship:

$$N(\geq L) = cL^{-2b}, \tag{2.5}$$

where N is the cumulative number of AE events generated by source defects with a characteristic linear dimension $\geq L$, c is a constant of proportionality, and $2b = D$ is the fractal dimension of the damage domain.

It has been evidenced that this interpretation rests on the assumption of a dislocation model for the seismic source and requires that $2.0 \leq D \leq 3.0$, i.e., the cracks are distributed in a fractal domain comprised between a surface and the volume of the analysed region (Turcotte, 1997; Rundle et al., 2003).

The cumulative distribution (2.5) is substantially identical to the cumulative distribution proposed by Carpinteri (Carpinteri, 1994), which gives the probability of a defect with size $\geq L$ being present in a body:

$$P(\geq L) \propto L^{-\gamma}. \tag{2.6}$$

Therefore, the number of defects with size $\geq$ L is:

$$N^{*}(\geq L) = cL^{-\gamma}. \tag{2.7}$$

where γ is a statistical exponent measuring the degree of disorder, i.e. the scatter in the defect size distribution, and c is a constant of proportionality. By equating distributions (2.5) and (2.7) it is found that: $2b = \gamma$. At the collapse, the size of the maximum defect is proportional to the characteristic size of the structure. As shown by Carpinteri and co-workers (Carpinteri et al., 2008b), the related cumulative defect size distribution (referred to as self-similarity distribution) is

characterized by the exponent $\gamma = 2.0$, which corresponds to $b = 1.0$. It was also demonstrated by Carpinteri (Carpinteri et al., 2008b) that $\gamma = 2.0$ is a lower bound which corresponds to the minimum value $b = 1.0$, observed experimentally when the load bearing capacity of a structural member has been exhausted.

Therefore, by determining the b-value it is possible to identify the energy release modalities in a structural element during the monitoring process. The extreme cases envisaged by Eq. (2.1) are $D = 3.0$, which corresponds to the critical condition $b = 1.5$, when the energy release takes place through small defects homogeneously distributed throughout the volume, and $D = 2.0$, which corresponds to $b = 1.0$, when energy release takes place on a fracture surface. In the former case diffused damage is observed, whereas in the latter two-dimensional cracks are formed leading to the separation of the structural element.

In the following, the data obtained from the monitoring are mainly interpreted by Eqs (2.2) and (2.4).

2.6 Monitoring Results

2.6.1 AE Sources: Bulk Cracks and Frescoes Detachments

The results obtained by the application of the AE sensors for the first time window of the SHM, starting May 9, 2011, and finishing June 16, 2011, are presented in Figs. 2.13 and 2.14.

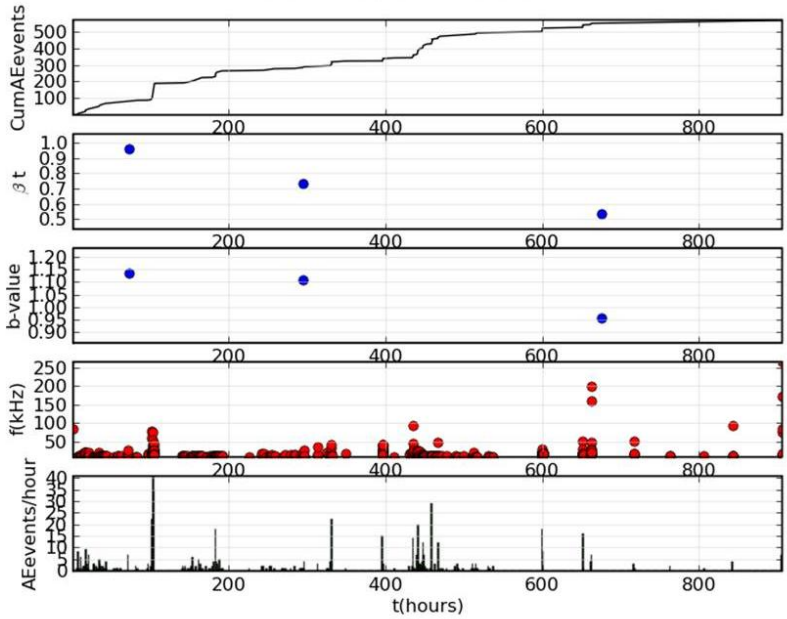

Figure 2.13 – Chapel XVII: AE from vertical crack monitoring.

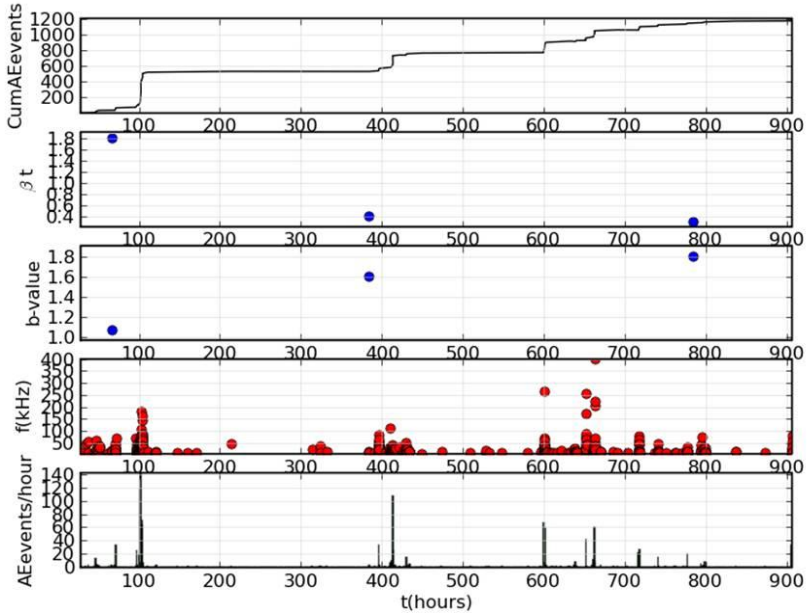

Figure 2.14 – Chapel XVII: AE from frescos detachment monitoring.

As can be seen from Fig. 2.13, the vertical crack monitored on the North wall of the chapel presents a stable condition during the acquisition period ($0.5 < \beta_t < 1.0$) and a distribution of cracks on a surface domain is clearly proved by the *b*-value in the range (0.95, 1.10). The evidence for the presence of a large crack is offered by the low frequency signals registered (< 200 kHz): as a matter of fact, considering the velocity as a constant and applying the Lamb ratio (Lamb, 1917), the wavelength needs to be larger than the size of the maximum inhomogeneity in order for the wave to pass through without significant modifications in its waveform. It is reasonable to assume that for a high frequency wave it is possible only to propagate through a small inhomogeneity; on the contrary for a low frequency wave it is possible also to propagate through a large inhomogeneity

(Landis and Shah, 1995; Carpinteri et al., 2007d). Concerning the monitored frescos detachment (Fig.2.14), the decorated surface tends to evolve towards metastable conditions ($0.5 < \beta_t < 1.8$) and the signals acquired show high frequency characteristics (< 400 kHz): therefore a distribution of microcracks in the volume is assumed for the analysed region.

Concerning the AE sources localization, the confidence regions shown in Fig.2.15 are identified by applying the following localization algorithms.

The time T_A taken for an Acoustic Emission signal to travel between the source position (x_0, y_0, z_0) and a sensor in position (x_A, y_A, z_A) is calculated using the following relationship, considering the wave velocity c as a constant:

$$T_A = \left[(x_0 - x_A)^2 + (y_0 - y_A)^2 + (z_0 - z_A)^2 \right]^{1/2} / c \,. \tag{2.8}$$

The above equation presents three unknowns. Therefore, AE source localization requires that at least three sensors pick up the same event. In order to identify the instant of emission is necessary to fourth reference sensor and the corresponding AE arrival time T_R:

$$\Delta t_A = T_A - T_R = \left[(x_0 - x_A)^2 + (y_0 - y_A)^2 + (z_0 - z_A)^2 \right]^{1/2} / c - T_R \,. \tag{2.9}$$

Considering the triangle S,S_1,S_2 , where S is the AE source, S_1 and S_2 represent two sensors (Fig.2.16) in polar coordinates, we have:

$$r_2 - r_1 = c\Delta t_{1,2} \,, \tag{2.10}$$

$$z = r_1 \sin(\theta - \theta_2) \,, \tag{2.11}$$

$$z^2 = r_2^2 - \left[r_{2,1} - r_1 \cos\left(\theta - \theta_2\right)\right]^2 . \tag{2.12}$$

Introducing Eq.(2.11) in Eq.(2.12):

$$r_1^2 = r_2^2 - r_{2,1}^2 + 2r_{2,1}r_1 \cos\left(\theta - \theta_2\right). \tag{2.13}$$

Neglecting r_2 and remembering that $r_1 = c(t_1\text{-}t_0)$, we have the following equation:

$$r_1 = \frac{r_{2,1}^2 - \Delta t_{2,1}^2 c^2}{2\left(\Delta t_{2,1} c + r_{2,1} \cos\left(\theta - \theta_2\right)\right)}, \tag{2.13}$$

that identifies the regions if Fig.2.15.

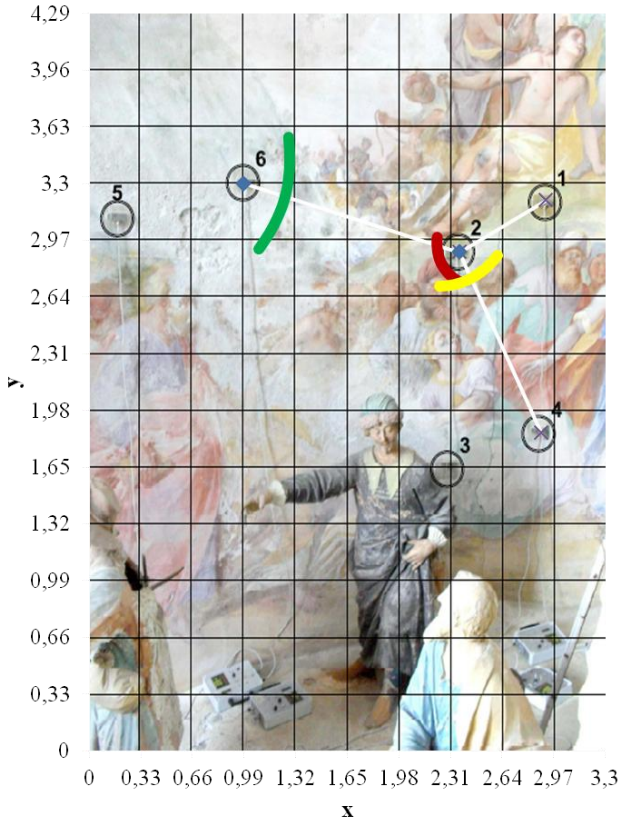

Figure 2.15 – Chapel XVII: AE sources and confidence regions**.**

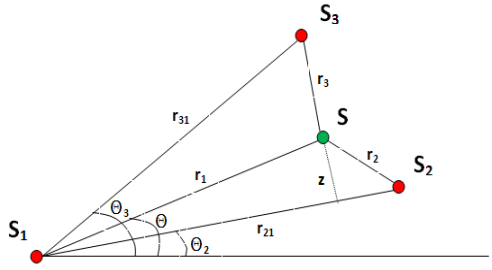

Figure 2.16 – AE source and sensors: Polar coordinates system**.**

2.6.2 Correlation between AE and Local Seismicity

Among the various studies on the earthquakes space-time correlation, there is a statistical method that allows to calculate the degree of correlation both in space and time between a series of AE and the local seismic recordings, collected in the same period. This analysis is based on the generalization of the space-time correlation known as the integral of Grassberger-Procaccia (Grassberger and Procaccia, 1983), defined as follows:

$$C(r,\tau) \equiv \frac{1}{N_{EQ}N_{AE}} \sum_{k=1}^{N_{EQ}} \sum_{j=1}^{N_{AE}} \Theta(r - |x_k - x_j|)\Theta(\tau - |t_k - t_j|) \quad , \tag{2.14}$$

where N_{AE} is the number of peaks of AE activity registered in site, in this case Chapel XVII, and in a defined time window, N_{EQ} is the number of earthquakes recorded in the surrounding area during the same time window, and Θ is the step function of Heaviside ($\Theta(x) = 0$ if $x \leq 0$, $\Theta(x) = 1$ if $x > 0$). The index *k* refers to the recorded seismic events $\{x_k, t_k\}$, while the index *j* refers to the recorded AE events $\{x_j, t_j\}$.

Therefore, between all possible pairs of recorded AE and seismic events, the sum expressed by the integral of Grassberger-Procaccia can be calculated for those having the epicentral distance $|x_k - x_j| \leq r$ and the temporal distance $|t_k - t_j| \leq \tau$. Hence, *C(r,τ)* is the probability of occurrence of two events, an earthquake and an AE event, whose mutual spatial distances are smaller than *r* and mutual temporal

distances are smaller than τ.

Note that, in order to evaluate Eq.(2.14), the numbers of N_{AE} and N_{EQ} are not required to assume the same value, and that x_j correspond to the geographic position of Chapel.

Anyway, this approach does not consider the chronological order of the two types of event. Since the AE time series and the earthquake sequences are closely intertwined in the time domain, the problem of the predictive ability of the AE peaks is still open. The records of AE could be both the consequences of the progressive development of micro damage, or the effect of widespread micro-seismicity. Therefore, a probabilistic analysis can be carried out discriminating between the AE events prior to the earthquake, which are precursors, and the AE following the earthquake, which are aftershocks. This analysis can be performed adopting a modified correlation integral (Carpinteri et al., 2007c):

$$C_{\pm}(r,\tau) \equiv \frac{1}{N_{EQ}N_{AE}} \sum_{k=1}^{N_{EQ}} \sum_{j=1}^{N_{AE}} \Theta\left(r - \left|x_k - x_j\right|\right) \Theta\left(\tau - \left|t_k - t_j\right|\right) \Theta\left(\pm\left(t_k - t_j\right)\right), \qquad (2.15)$$

where "+" and "−" in the Heaviside function are used to take into account that the AE events could be respectively seismic precursors and aftershocks.

In this way, the function $C^{+}(r, \tau)$ gives the probability that a peak of AE, detected at a certain time, will be followed by an earthquake in the subsequent days within a radius of r kilometers from the AE monitoring site. Varying the thresholds r and τ in Eq. (2.15), two cumulative probability distributions can been constructed, one for each condition (sign "+" or "−") and then the corresponding probability density

functions can been derived and represented (see Fig.2.17 and Tables 2.1-2.6, in which the radius r ranges between 60 and 100 kilometers, and the time interval τ varies from 1 week up to a maximum of 9 weeks).

The data series of analyzed AE are shown in Figs. 2.18 and 2.19, and are related to the abovementioned time intervals. The seismic events are taken from the website http://iside.rm.ingv.it/iside/standard/result.jsp?page=EVENTS#result (seismic catalog of INGV, National Institute of Geophysics and Volcanology), selecting the events comprised in a circle of 100 km radius around the site of Sacred Mountain of Varallo, during the defined AE monitoring periods (Fig.2.18).

Looking at the temporal distribution of earthquakes in relation to the cumulative AE trend, a quite good correspondence between AE peaks and earthquake events can be observed (Figs.2.19,2.20). By applying the modified correlation integral of Grassberger-Procaccia to the data series, we obtain the cumulative probabilities, as a function of the radius of interest r and of the interval of occurrence τ, both considering the peak of Acoustic Emission as earthquake precursor or as aftershock (Tables 2.1-2.4).

The probability values obtained for the period May-June show that, regardless of the distance and of the correlation time, the probability of a seismic event following a peak of Acoustic Emission (*AE Precursor*) is always greater than the probability of the same AE peak being an effect of the damage caused by the earthquake (*AE Aftershock*) (Tables 2.1,2.2). In practice, we see that the monitored structure behaves as a sensitive seismic receptor.

It is interesting to note that, for both monitoring periods, within a radius of 60 km from the monitored site, the AE signals still play their role as seismic precursors, as can be assessed observing the values of the cumulative probability C^{+}. On the

contrary, at distances of 80 km and 100 km, the character of AE occurrence is different (see Tables 2.3,2.4). In particular, we observe a clear reversal of the AE signal character from precursor to aftershock for the second monitoring period (July-September).

More in details, within a radius of 60 km there is a clear tendency of AE signals to anticipate earthquakes, and behave as precursors. At a distance of 80 km AE are precursor signals only in the time window comprised between 2 and 6 weeks, were $C^+ > C^-$. At a distance of 100 km all the AE signals behave as aftershocks, being always $C^+ < C^-$.

In any case, it is worth distinguishing between the environmental contributions due to crustal trembling (external source), and the structural damage contributions (inner source) to AE activity on the Chapel XVII.

To better analyze the results from the second monitoring period (Table 2.3,2.4), it is useful to discriminate the recorded signals assigning thresholds both in frequency and amplitude, which are consistent with the physical nature of Acoustic Emissions detected by the sensors. Looking at the USAM data stored, a good choice to discriminate the recorded signals is setting a frequency threshold equal to 30 kHz, which divides the field VLF (Very Low Frequency) from the field LF (Low Frequency), and a signal amplitude threshold equal to 1 mV. The choice of the thresholds (amplitude and frequency) was based upon empirical considerations in order to emphasize the signals coming farther from the structure, which were characterized by lower frequencies and amplitudes.

The results are shown in Table 2.5 and Table 2.6, where it can be easily recognized that filtered AE signals actually behave like seismic precursor. From a theoretical point of view, lower frequencies allow for the diffusion of the elastic

waves in the masonry bulk, either intact or damaged, while higher frequency waves can propagate only through small heterogeneities (Aggelis, 2011b; Aggelis et al., 2012d; Aggelis et al., 2012e). Moreover, if constant velocity is assumed, the Lamb ratio (Lamb, 1917) implies that the AE wavelength has to be larger than the size of the maximum inhomogeneity in order to travel through the ground up to the structure without significant modifications in its waveform (Landis and Shah, 1995). On the other side, low amplitudes are reasonably related to the fact that an event captured by AE sensors on the monitored structure may have originated from a source physically distant from the monitored site (surrounding micro-seismicity that shakes the whole structure) and therefore is subject to the laws of amplitude damping (Aggelis et al., 2012e).

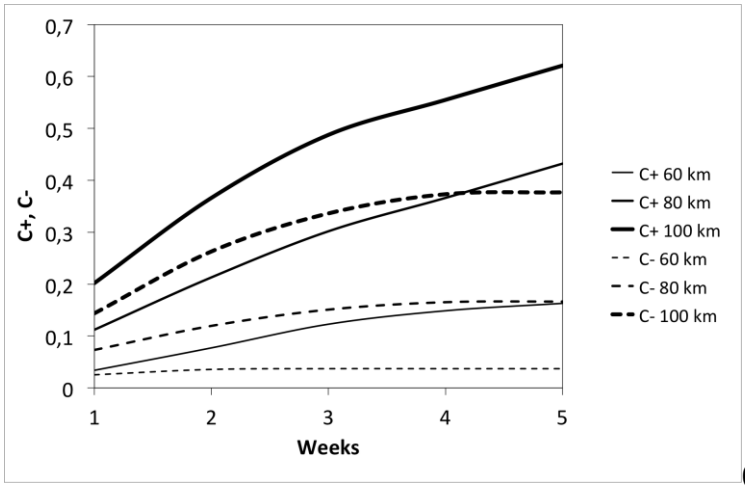

(a)

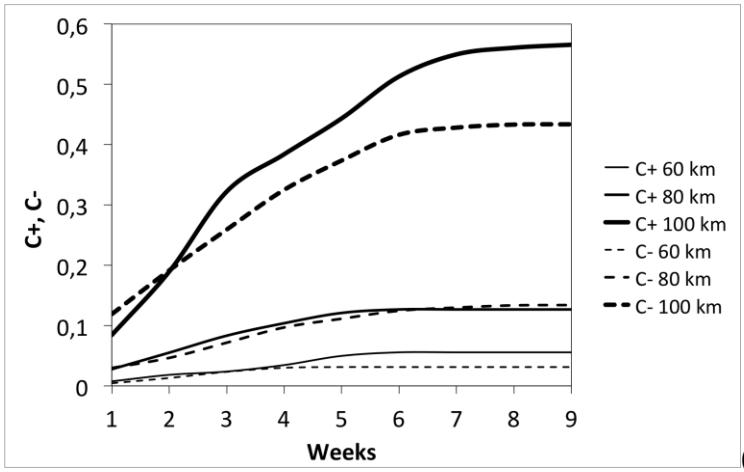

(b)

Figure 2.17 – Evolution of the modified correlation integral for different time windows, during the two monitoring period. (a) Monitoring time from May 9, 2011 to June 16, 2011, see Tables 2.1, 2.2. (b) Monitoring time from July 5, 2011 to September 5, 2011, see Tables 2.5, 2.6**.**

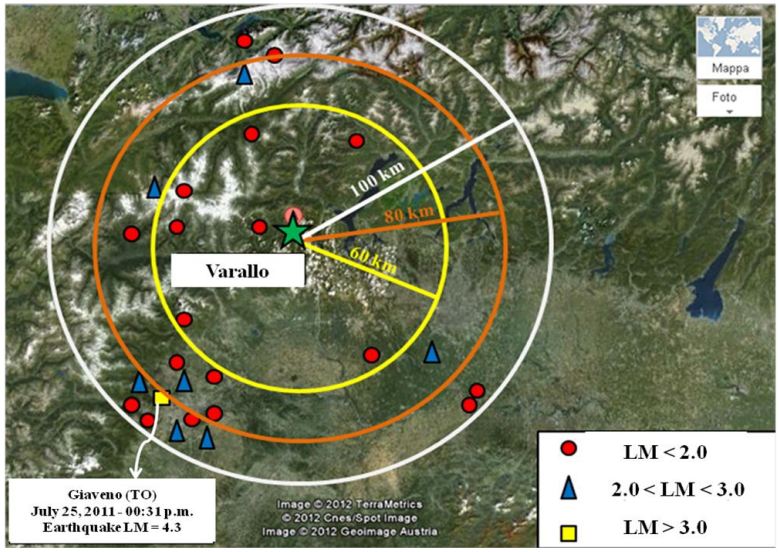

Figure 2.18 – Seisimic events around Varallo (Italy) from May, 2011 to September, 2011 (LM: Local Magnitude).

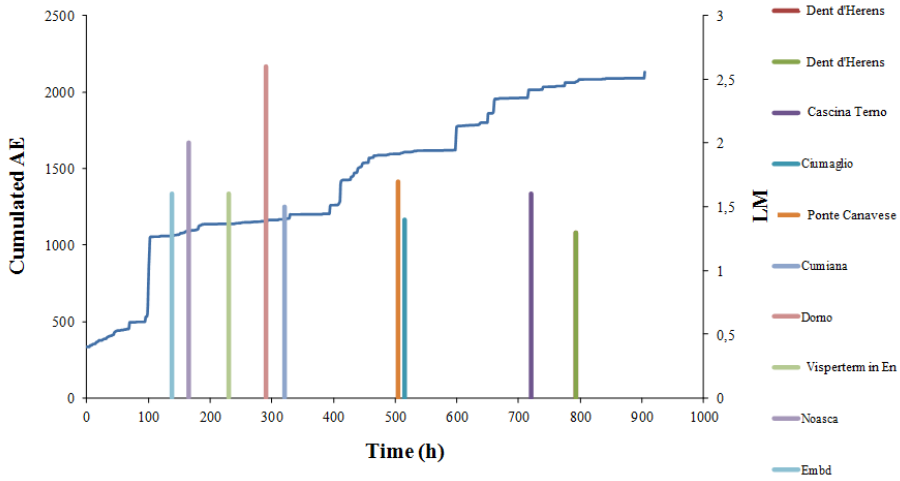

Figure 2.19 – Sacred Mountain of Varallo: cumulated AE and seismic events from May 9, 2011 to June 16, 2011 (LM: Local Magnitude).

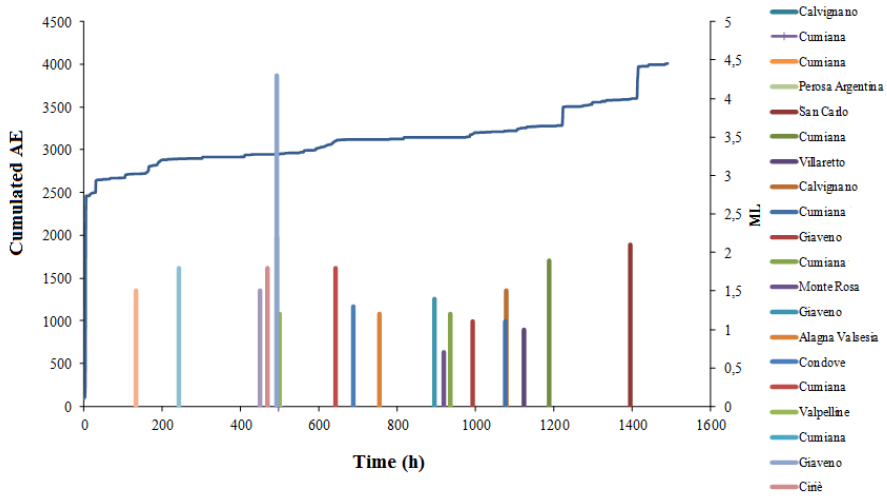

Figure 2.20 – Sacred Mountain of Varallo: cumulated AE and seismic events from July 5, 2011 to September 5, 2011 (LM: Local Magnitude).

Table 2.1 – AE as precursor from May 9, 2011 to June 16, 2011: Cumulative probability $C^{+}(r, \tau)$ for radius r ranging between 60 and 100 km, and time τ varying from 1 week to 5 weeks.

	60 km	80 km	100 km
1 week	0.0339	0.1121	0.2018
2 weeks	0.0772	0.2130	0.3661
3 weeks	0.1228	0.3018	0.4875
4 weeks	0.1487	0.3661	0.5549
5 weeks	0.1630	0.4321	0.6210

Table 2.2 – AE as aftershock from May 9, 2011 to June 16, 2011: Cumulative probability $C^{-}(r, \tau)$ for radius r ranging between 60 and 100 km, and time τ varying from 1 week to 5 weeks.

	60 km	80 km	100 km
1 week	0.0254	0.0732	0.1437
2 weeks	0.0357	0.1196	0.2629
3 weeks	0.0371	0.1509	0.3362
4 weeks	0.0371	0.1652	0.3732
5 weeks	0.0371	0.1665	0.3768

Table 2.3 – AE as precursor from July 5, 2011 to September 5, 2011: Cumulative probability $C^{+}(r, \tau)$ for radius r ranging between 60 and 100 km, and time τ varying from 1 week to 9 weeks.

	60 km	80 km	100 km
1 week	0.0075	0.0278	0.0846
2 weeks	0.0184	0.0552	0.1896
3 weeks	0.0239	0.0833	0.3222
4 weeks	0.0346	0.1040	0.3841
5 weeks	0.0498	0.1210	0.4435
6 weeks	0.0557	0.1268	0.5130
7 weeks	0.0557	0.1268	0.5497
8 weeks	0.0557	0.1268	0.5607
9 weeks	0.0557	0.1268	0.5657

Table 2.4 – AE as aftershocks from July 5, 2011 to September 5, 2011: Cumulative probability $C^{-}(r, \tau)$ for radius r ranging between 60 and 100 km, and time τ varying from 1 week to 9 weeks.

	60 km	80 km	100 km
1 week	0.0045	0.0298	0.1192
2 weeks	0.0132	0.0465	0.1916
3 weeks	0.0234	0.0717	0.2592
4 weeks	0.0301	0.0970	0.3251
5 weeks	0.0313	0.1114	0.3737
6 weeks	0.0313	0.1246	0.4164
7 weeks	0.0313	0.1299	0.4283
8 weeks	0.0313	0.1336	0.4333
9 weeks	0.0313	0.1341	0.4338

Table 2.5 – Filtered AE as precursor from July 5, 2011 to September 5, 2011: Cumulative probability $C^{+}(r, \tau)$ for radius r ranging between 60 and 100 km, and time τ varying from 1 week to 9 weeks.

	60 km	80 km	100 km
1 week	0.0080	0.0290	0.0829
2 weeks	0.0197	0.0592	0.1969
3 weeks	0.0252	0.0866	0.3288
4 weeks	0.0364	0.1081	0.3920
5 weeks	0.0517	0.1248	0.4538
6 weeks	0.0577	0.1308	0.5267
7 weeks	0.0577	0.1308	0.5625
8 weeks	0.0577	0.1308	0.5731
9 weeks	0.0577	0.1308	0.5776

Table 2.6 – Filtered AE as aftershocks from July 5, 2011 to September 5, 2011: Cumulative probability $C^{-}(r, \tau)$ for radius r ranging between 60 and 100 km, and time τ varying from 1 week to 9 weeks.

	60 km	80 km	100 km
1 week	0.0042	0.0294	0.1149
2 weeks	0.0117	0.0464	0.1889
3 weeks	0.0203	0.0681	0.2521
4 weeks	0.0278	0.0935	0.3142
5 weeks	0.0292	0.1074	0.3604
6 weeks	0.0292	0.1202	0.4041
7 weeks	0.0292	0.1253	0.4151
8 weeks	0.0292	0.1292	0.4213
9 weeks	0.0292	0.1297	0.4218

2.7 Laboratory AE Measurements due to Capillary Rise in Mortar

A preliminary experimental test has been set up in Fracture Mechanics Laboratory of the Politecnico di Torino to find out sudden evidences for the recorded AE from Chapel XVII structural monitoring. The purpose is to find a correlation between specific analyzed AE activity and damage of the decorated surface due to different water cycle stages (e.g. immersion, drying and cooling) linked to the phenomenon of capillary rise. A mortar specimen was monitored by means of AE during 60 minutes of immersion in mineral water (Fig.2.21a) with USAM unit above mentioned. The problem is at the present time practically unexplored, although some Authors reported analogous AE activity recorded in similar conditions

(Grossi et al., 1997).

The first evidence is that the evolution of the cumulated AE resembles the kinetics of the capillary rising in the transient regime (Fig.2.21b): this underlies how the two phenomena are correlated. We could see also that the frequency field of AE events registered during the mortar immersion test (Fig.2.21a) reminds the frequency field detected from frescos detachment (Fig.2.14); a probable reason of the decorated surface deterioration may be found in moisture diffusion through the structural support. The normal distribution of the frequencies obtained during the laboratory test (Fig.2.22a) shows a dispersion wider than the AE frequency distribution detected "in situ" (Fig.2.22b). As a matter of fact, the AE signals due to frescos detachment are related to a limited period of damage within the whole life-time of the structure, while the laboratory test investigates the mortar specimen behavior starting from a totally dry condition. Nevertheless, both results show signals in a higher frequency range compared to that produced by the monitored vertical crack (Fig.2.13).

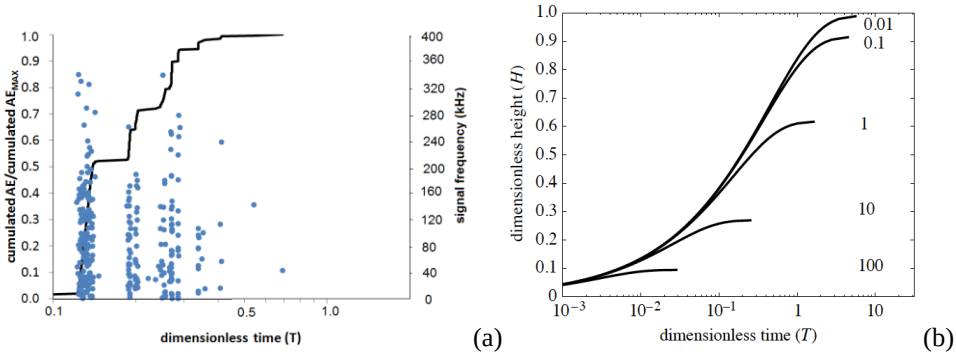

Figure 2.21 – *(a)* Cumulated Number of AE Events during mortar immersion in mineral water with AE Frequencies; *(b)* Dimensionless diagram of the capillary rising. Each curve refers to the dimensionless quantity α, which is a function of the sample thickness, sorptivity and potential evaporation of the micro-environment (Hall and Hoff, 2007).

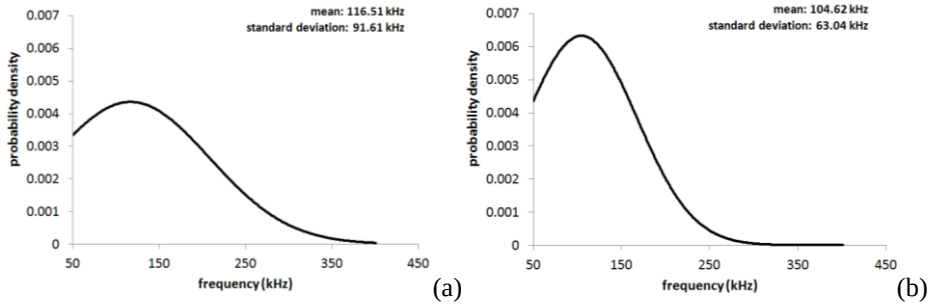

Figure 2.22 – *(a)* Normal distribution of frequencies registered during mortar immersion test; *(b)* Normal distribution of frequencies registered during frescos detachment monitoring.

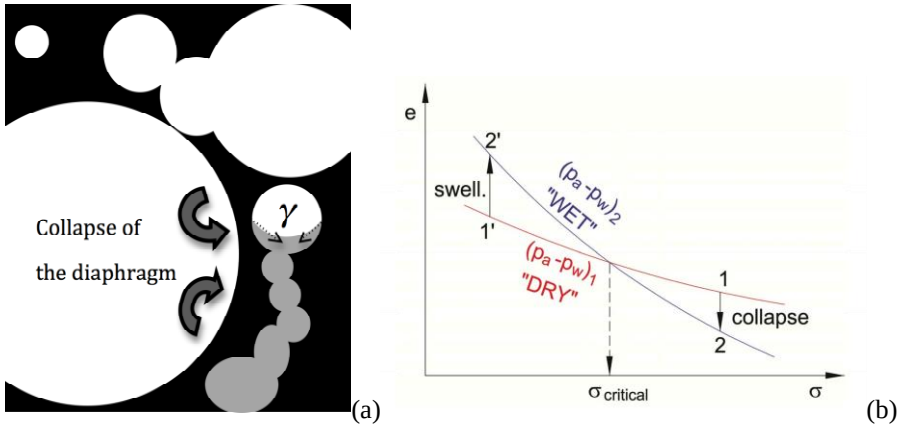

Figure 2.23 – *(a)* Scheme of the collapse of diaphragm between pores of different diameter due to capillary surface tension γ; *(b)* dilatation *e* of an hydrated swelling clay-like material below the critical stress σ_{cr}: "p_a" means air pressure in the pores, while "p_w" water pressure in the pores.

More generally, such a deterioration process characterized by AE activity, could be due to a sort of local rupture of the rigid skeleton of the mortar structure, necessarily leading to microcrack development or to an increase in the number of voids.

Two possible main mechanisms can be assumed, namely due to chemical or mechanical processes. From the chemical point of view, the local damage could be caused by the presence of swelling salts in the mortar components. The crystallization of salts inside the mortar pores is commonly known as *crypto-florescence*. A typical case is sodium sulphate crystallization. A reversible solubility reaction determines the amount of *mirabilite* ($Na_2S0_4 \bullet 10H_2O$) in equilibrium with *thenardite* (Na_2S0_4), as a function of relative humidity and temperature. As the content of water increases, the percentage of *mirabilite* growths, leading to swelling and damage, due to the lower density of *mirabilite*

with respect to *thenardite* (Grossi et al., 1997).

From the mechanical point of view, the rise of water into the porous mortar is influenced by the complex distribution of voids of different size and different degree of connection. Therefore, the presence of water in connected network of small pores (Fig.2.23a), nearby larger empty pores, can realize large unbalanced forces (due to the surface tension γ), which are able to trigger the collapse of the diaphragm. Local ruptures of such kind can be found in the literature about MEMS device (Mastrangelo et al., 1993).

Finally, the presence of very small porosity in the mortar (in the range between 10 and 105 nm) can be at the origin of a swelling behavior similar to the one displayed by unsaturated clay-like materials (Sheng et al., 2008). In this case, the increase in humidity, if the state of stress is below the critical stress, is accompanied by an increase in the volume (Fig. 2.23b). This phenomenon could occur locally in mortar, and the restrained expansion may lead to damage and AE activity.

2.8 Finite Element Modeling: Spectral Dynamic Analysis of the Chapel XVII

The Chapel XVII is discretized with three-dimensional linear pyramid elements, accounting for the accurate geometry of the stone masonry structure. The shape of the cylindrical chapel, and of the above spherical dome are precisely discretized, taking into account the various apertures, the inside internal vault supporting the Mount Tabor installation, and the outside pronao with columns. On the contrary, the wooden roof structure was considered only as an external load. The mesh of

the structure is shown in Fig. 2.24. The finite element model is discretized using 30271 nodes, connected by 129689 elements, and is characterized by 86076 degrees of freedom. The elastic properties assumed for the masonry, and the density, where respectively equal to: E = 2×109 Pa; ν = 0.3; γ = 20 kN/m3. For the dynamic analysis, the Elastic Response Spectrum of Acceleration *Sd (g)* is shown in Fig. 2.25. It is obtained considering the geographic coordinates of the site of investigation, the soil characteristics, a nominal life of the structure equal to 400 years and a probability to exceeding the acceleration spectrum equal to 5% in 400 years. The structural damping of masonry is considered equal to 5%. The vertical component of the Spectrum is neglected (Ministero delle Infrastrutture, 2008).

The dynamic analysis, performed with the commercial finite element code DIANA® (Maine, 2012) allows for a preliminary assessment of the modal behavior of the structure. Table 2.7 shows natural frequencies and periods of the first 20 calculated modes of vibration of Chapel XVII, and percentages of mass involved in each mode of vibration for direction X and Y in the horizontal plane. The first 3 modes of vibration of the structure are shown in Fig. 2.26.

Fig. 2.27 shows the contour of the principal tensile stress during simulated earthquake, reported on the deformed shape of the structure. The total combination of the seismic effects is performed using the Square Root of the Sum of the Squares (SRSS) method. The tensile stresses calculated on the internal wall of the chapel, subjected to dead loads and an earthquake in the X direction, justify the presence of the two symmetric dominant cracks detected by a visual inspection. Fig. 2.28 shows the deformed shape of the structure compared to the initial shape under the effect of the dead loads only. The deformation clearly shows the opening mechanism due to the effect of the pronao settlement, as well as to the thrust of the

internal vault that support the mount Tabor installation.

The FEM analysis provides stress levels under dead loads near to the vertical cracks that are not so high for a stone masonry with mortar joints (see Fig.2.27 and Fig.2.28). Therefore, the stability assessment derived by AE monitoring, reported above, is confirmed and a stable behavior of fractures is identified. On the other hand, the dynamic FEM analysis, in correspondence to the main seismic events locally identifies levels of stress that agree well with the nucleation of microcracks after the arrival of the main seismic shockwave, which are detected as the AE aftershocks abovementioned.

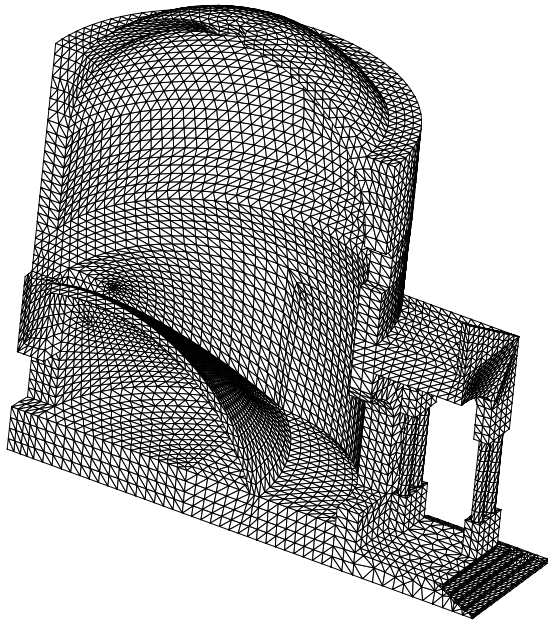

Figure 2.24 – Sacred Mountain of Varallo: Finite element mesh of Chapel XVII. Half of the model.

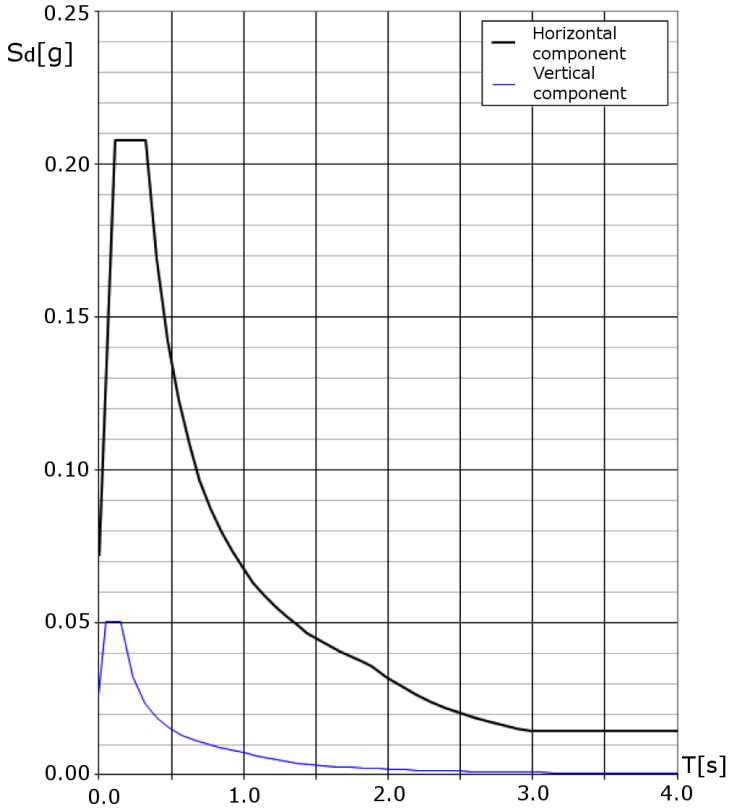

Figure 2.25 – Sacred Mountain of Varallo: Elastic response spectrum of acceleration *Sd (g)*.

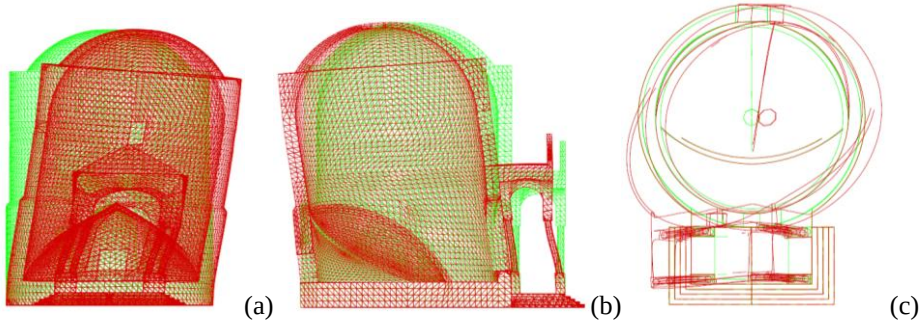

(a) (b) (c)

Figure 2.26 – Sacred Mountain of Varallo: *(a)* Chapel XVII mode 1 of vibration; *(b)* Chapel XVII mode 2 of vibration; *(c)* Chapel XVII mode 3 of vibration (c).

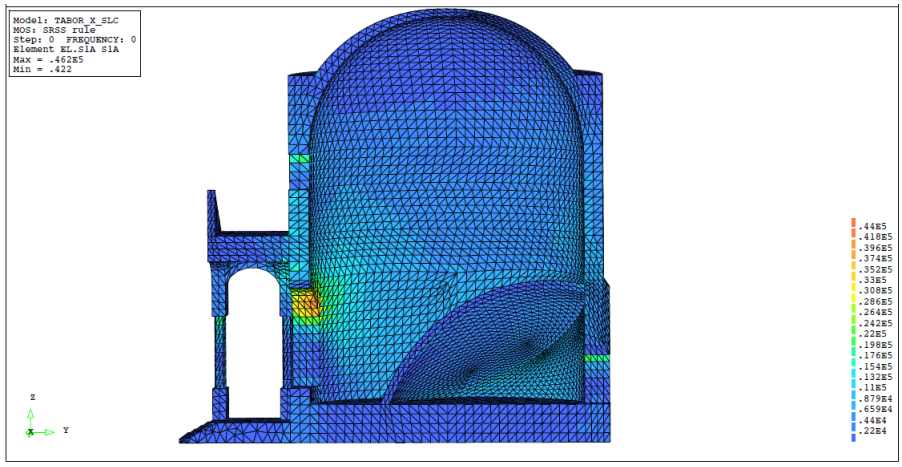

Figure 2.27 – Sacred Mountain of Varallo: Chapel XVII principal SRSS stress contour, measured in Pa, during simulated earthquake in the *X* direction.

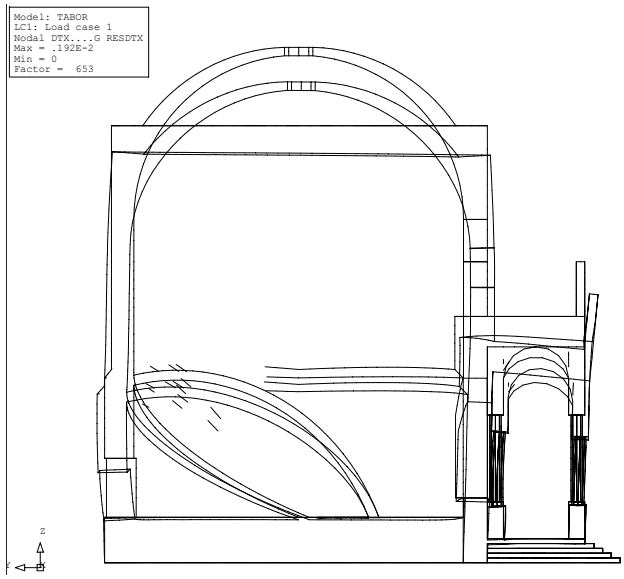

Figure 2.28 – Sacred Mountain of Varallo: Chapel XVII deformed shape.

Table 2.7 – Natural frequencies of the first 20 calculated modes of vibration of Chapel XVII, and percentages of mass involved in each mode of vibration for direction *X* and *Y* in the horizontal plane.

			X Direction		*Y* Direction	
Mode	Frequency [Hz]	Period [s]	%	Cumulated %	%	Cumulated %
1	4.737	0.211	5.31E+01	5.31E+01	5.89E–05	5.89E–05
2	5.162	0.194	5.82E–05	5.31E+01	4.97E+01	4.97E+01
3	8.570	0.117	5.94E–02	5.32E+01	2.61E–07	4.97E+01
4	9.891	0.101	1.20E–01	5.33E+01	1.43E–05	4.97E+01
5	10.087	0.099	1.50E–05	5.33E+01	1.95E–01	4.99E+01
6	13.192	0.076	3.37E+00	5.67E+01	4.59E–06	4.99E+01
7	13.373	0.075	1.68E–04	5.67E+01	2.85E–01	5.02E+01
8	13.881	0.072	6.60E+00	6.33E+01	5.39E–06	5.02E+01
9	14.479	0.069	6.48E–05	6.33E+01	9.44E+00	5.96E+01
10	14.616	0.068	1.13E–04	6.33E+01	3.83E+00	6.35E+01
11	15.633	0,064	2.65E–05	6.33E+01	3.31E–01	6.38E+01
12	17.402	0.057	2.36E–02	6.33E+01	5.14E–06	6.38E+01
13	17.612	0.057	3.66E–06	6.33E+01	5.25E–02	6.38E+01
14	18.031	0.055	5.02E–01	6.38E+01	1.91E–05	6.38E+01
15	18.677	0.054	2.45E–04	6.38E+01	1.28E–01	6.40E+01
16	18.750	0.053	9.08E–02	6.39E+01	1,67E–04	6.40E+01
17	19.165	0.052	6.71E–02	6.40E+01	1.91E–05	6.40E+01
18	19.874	0.050	3.13E–09	6.40E+01	2.02E–01	6.42E+01
19	20.545	0.049	4.58E–01	6.44E+01	7.58E–06	6.42E+01
20	21.578	0.046	5.79E–06	6.44E+01	5.48E–01	6.47E+01

2.9 Concluding Remarks

Chapel XVII of the Sacred Mountain of Varallo, dedicated to the Mount Tabor episode of Christ Transfiguration, shows some structural concern due to cracking and degradation of the high valuable frescos, which tend to detach from the masonry support.

In order to assess the evolution of the phenomena, the results of the Acoustic Emission monitoring program of the Chapel have been provided, together with a structural finite element simulation.

The Finite Element analysis provided the basic mechanism that is taking place in the chapel, which caused two main cracks in the internal walls.

The results of the monitoring show that the large cracks are stable, while the process of detachment of the frescos is evolving cyclically. It seems that the frescos degradation could be mainly related to the diffusion of moisture in the mortar substrate. Some preliminary laboratory tests also confirm that Acoustic Emissions are recorded in mortar samples subjected to moisture diffusion

Besides the canonical use in non-destructive tests, the heuristic potential of Acoustic Emission monitoring of civil and historical structures for earthquakes prediction appears very intriguing. Starting from the assumption that any structure should not be regarded as separated from its environment, a method of correlating AE activity on the Chapel XVII of the Sacred Mountain of Varallo subjected to a long-term monitoring with regional seismicity is investigated. Two qualitatively very similar phenomena such as Acoustic Emission and earthquakes become two aspects of a unique phenomenon, which looks self-similar.

Furthermore, by applying the modified Grassberger-Procaccia correlation

algorithm −with the aim of explaining the correlation between regional seismicity and Acoustic Emission emerging from the Chapel XVII of the Sacred Mountain of Varallo− it is observed that the structure behave as sensitive receptors for earthquakes occurring within a radius of about 100 km, distinguishing environmental contributions to AE activity on the Chapel XVII due to crustal trembling (external source) from contributions due to structural damage (inner source). The accurate finite element model, performed with DIANA ® finite element code for the dynamic analysis of Chapel XVII structure, is utilized to confirm visual inspections and monitoring results of the earthquakes effects.

Chapter 3

SHM of Terracotta Statues: Scaling in Damage by Electrical Resistance Measurements

3.1 Introduction

Contemporary civilization considers the conservation of monuments and art works of past centuries for future generations as an essential duty. For example, Italian historic buildings and monuments are exposed to the action of harsh environment which results in accelerated aging and deterioration.

The latter case is indeed illustrated by Sacro Monte di Varallo, which is made up of 45 Chapels, with similar problems due to the difficult environmental situation, but never identical (De Filippis, 2009). There chapels where the floor is below the level of the ground outside (with the effects of damp, similar to those in the cellars of our houses) others above land level, some surrounded by thick vegetation, therefore in the shade, other well exposed and sunny. The interior decorations are made of different materials which react differently to the ambient humidity: wood terracotta, unfired clay, mortar made with chalk and marble dust, etc. In particular,

the chapel interiors contain over 800 life-size wooden and multicolored terracotta statues illustrating the life, passion, death and resurrection of Christ (Figs.2.3 and 3.1).

Well-reasoned maintenance and intervention programs on the chapel interiors firstly require the use of Structural Health Monitoring (SHM) and non-destructive investigation techniques to assess statues' integrity without altering their state of conservation. Quantitatively evaluating the progressive deterioration of materials is a critical issue due to the treacherous nature of damage phenomena, that may suddenly degenerate into catastrophic failures (Sornette et al., 1998; Johansen and Sornette, 2000; Zapperi et al., 1997). Around 1500, Leonardo da Vinci was already preoccupied with the characterization of fracture by means of mechanical variables (Lemaitre and Chaboche, 1990). However, it is only in 1958 that the development of damage mechanics began. In that year, Kachanov (Kachanov, 1986) published the first paper devoted to a continuous damage variable directed towards modeling the deterioration of materials prior to macroscopic fracture.

Electrical resistance measurements and Acoustic-emission (AE) technique make experimentally accessible the damage variable introduced in damage mechanics (Bridgman, 1932; Russell and Hoskins, 1969; Lemaitre and Dufailly, 1987; Sun and Guo, 2004; Lacidogna et al., 2011b; Niccolini et al., 2013a; Niccolini et al., 2013b; Carpinteri et al., 2013d). The combined application of these non-destructive investigation techniques have already proved to be a powerful tool for damage assessment in rocks and concrete (Chen and Liu, 2008; Niccolini et al., 2012).

In literature research studies investigated the possibility of correlating AE activity in a structure with analogous activity detected on specimens taken from the

structure and tested to failure (Carpinteri and Lacidogna, 2007a; Niccolini et al., 2011; Carpinteri et al., 2013d). Analogously, in the next sections we present in situ and laboratory applications of a simple and inexpensive equipment for electrical resistance measurements. Thus, the evolution of ongoing damage processes in laboratory specimens and terracotta statues is assessed.


(a)
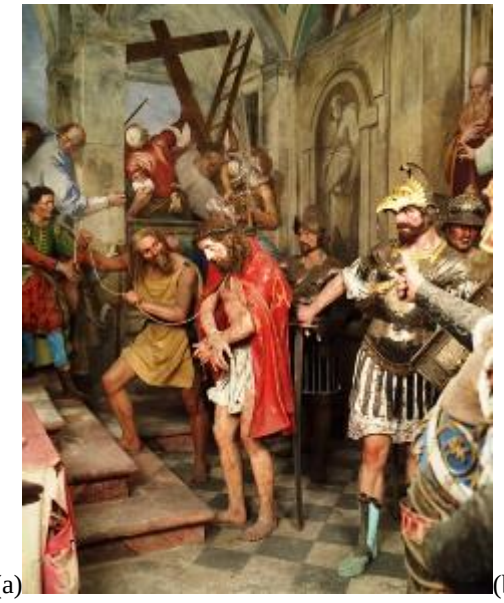
(b)

Figure 3.1 – Sacro Monte di Varallo (Italy): *(a)* Chapel XVI, *The Transfiguration of Christ on Mount Tabor*, A Devoted; *(b)* Chapel XXXV, *The Sentencing of Christ.*

3.2 Damage Variable and its Electrical Resistance Change Representation

The phenomenon of damage from a physical point of view represents surface discontinuities in the form of microcracks, or volume discontinuities in the form of voids, and it is marked by pronounced irreversibility. It can be very difficult to macroscopically distinguish a highly damaged volume element from a virgin one, since depth of cracks or inner defects cannot be quantified or identified. It therefore becomes necessary to imagine internal variables representing the deteriorated state of the material, which are directly accessible to measurements (Lemaitre and Chaboche, 1990)

A damage variable D can be defined by $D_n = S_0/S$, where S is the cross-sectional area (with normal n) of the considered volume element V and S_0 is the total area of the defect traces (microcracks, voids, etc.) on this section (Kachanov, 1986; Lemaitre and Chaboche, 1990; Krajcinovic, 1996; Krajcinovic and Rinaldi, 2005). Considering a distribution of defects without preferred orientation, the damage variable is a scalar quantity: $D_n = D, \ \forall n$. The damage variable D introduced in damage mechanics quantifies the deviation of a brittle material from linear elasticity, $\sigma = E_0(1-D)\varepsilon$, where σ and ε are respectively the stress and the strain in the material, and E_0 is the Young modulus of the undamaged material. In general, $0 \leq D \leq 1$. When $D = 0$ linear elasticity is applicable to the material which is still in undamaged state; as $D \rightarrow 1$ ($\varepsilon \rightarrow \infty$) failure occurs.

In recent years, the correlation of electrical resistance of solids with damage has been investigated as well. As the failure stress is approached, opening of micro and macrocracks causes more void space in the material and consequently a higher

electrical resistance (Bridgman, 1932; Russell and Hoskins, 1969). Some definitions of damage variable based on electrical resistance changes have been developed (Lemaitre and Dufailly, 1987; Sun and Guo, 2004; Chen and Liu, 2008; Lacidogna et al., 2011b), the simplest one being

$$D = 1 - R_0 / R = (R - R_0) / R. \tag{3.1}$$

Where $R - R_0$ is the increase in electrical resistance between the damaged and the undamaged state. When the material ruptures into two parts ($D \to 1$) the electrical resistance becomes infinite ($R \to \infty$), as consistently stated by Eq. (3.1).

3.3 Time-dependent Stress on Laboratory Specimens

A schematic diagram of the equipment used in conducting the experimental study is shown in Fig.3.2. We consider two prismatic mortar specimens (section: 40×40 mm^2, height: 160 mm) enriched with iron oxide to increase the electrical conductivity (Fig.3.3a). The specimens were subjected to uniaxial compression until failure at constant displacement rate of 2 μm s^{-1}. This condition was applied by a servo-hydraulic press MTS (maximum capacity: 500 kN) equipped with control electronics (Fig.3.3b).

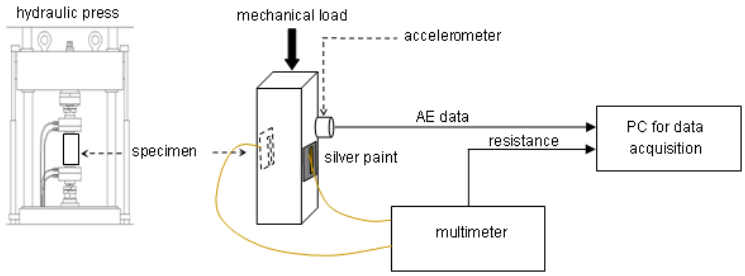

Figure 3.2 – Schematic representation of the laboratory experimental set-up.


(a)


(b)

Figure 3.3 – *(a)* Prismatic Mortar Specimens enriched with 10% of Iron Dioxide; *(b)* Laboratory Experimental Set-up.

Figure 3.4 – Agilent model 34411A Multimeter Detector.

Two types of measurements were carried out on the loaded specimens. Electrical resistance measurements were made with the constant voltage method, using an Agilent 34411A multimeter capable of measuring resistances as high as 1 GΩ (Fig.3.4). Each specimen was connected to the multimeter using two copper electrodes. Prior to testing, the specimen faces on which the electrodes were attached were coated with a conducting silver paint in order to minimize contact resistance (Russell and Hoskins, 1969). Initial resistance measurements were thus made on both specimens with no stress applied. Very close values (R_0 = 0.44 and 0.46 MΩ) were found for the two specimens. Then, the changing resistance R (averaged over 4 s) was measured during loading test until the specimen failed. The resistance at the time of failure was about 12 MΩ for both specimens (Fig.3.5).

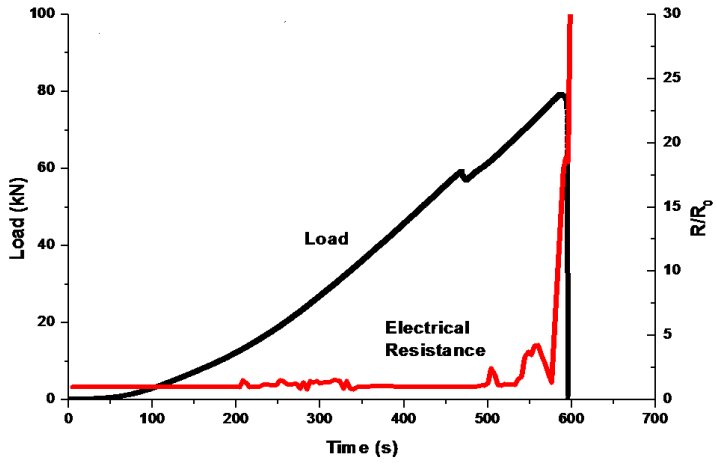

Figure 3.5 – Load vs. time diagram and relative electrical resistance (R/R_0) variation for the prismatic mortar specimen.

Furthermore, acoustic-emission (AE) events associated with microcracks were measured using a calibrated accelerometer mounted on the specimen surface (Cox and Meredith, 1993; Lockner, 1993; Colombo et al., 2003; Niccolini et al., 2012; Carpinteri and Lacidogna, 2007a; Accornero et al., 2012). The sensitivity of the accelerometer is 9.20 pC/m·s^{-2}. AE measurement was made over the range of few hertz to 10 kHz at the sampling rate of 44.1 kHz. Prior to testing, the detection threshold was set in order to filter out spurious noisy signals. Each AE event was characterized by the time of occurrence and the magnitude M, expressed in dB through the relation $M = 20\ log(a_{max}/1\ \mu m\ s^{-2})$, where a_{max} is the peak acceleration on the specimen surface produced by the AE wave.

Fig.3.6 shows results of the two loading tests. On this figure, the axial compressive stress applied to the specimens, the electrical resistance R, the time series of AE event amplitudes and the accumulated number of AE events are

plotted vs. time.

From the stress-time diagrams of Fig.3.6, it is observed that linear elasticity is applicable until the failure stress σ_f has been reached. This behaviour is referred to as brittle failure. Despite the absence of significant deviations from linear elasticity, the increase in electrical resistance and AE activity during the approach to failure indicates that damage is accumulating within the specimens.

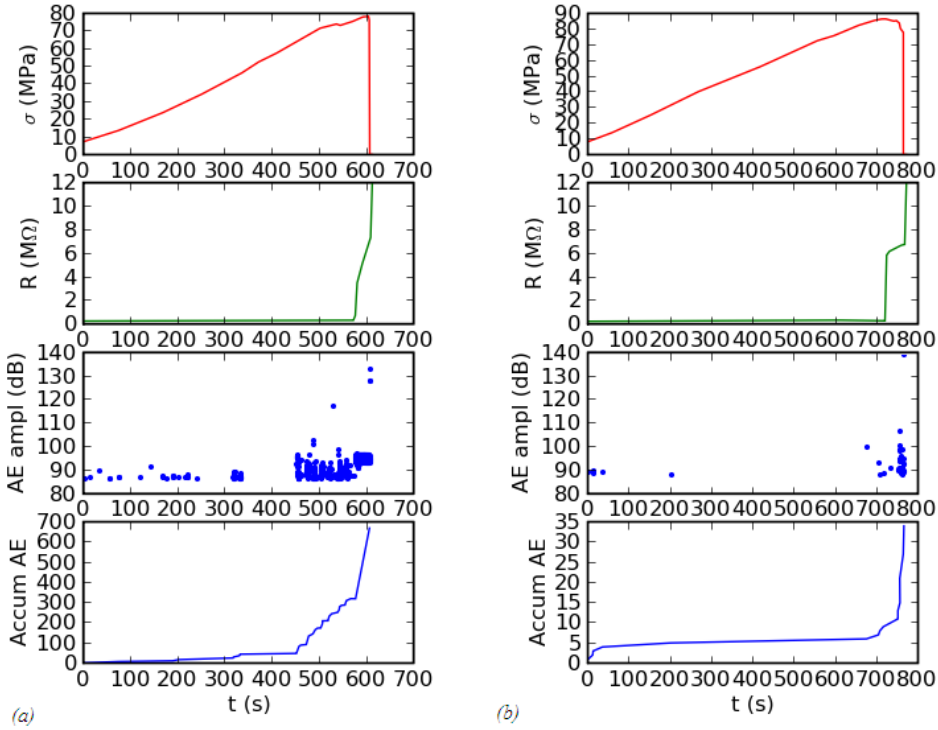

Figure 3.6 – Applied stress, electrical resistance, AE event amplitudes and cumulative AE event number vs. time for mortar specimens (a, b).

We consider the dependence of the electrical resistance R on the non dimensional stress σ/σ_f. A reasonably simple function fitting to the experimental data is a scaling law

$$R(x) = \frac{\beta}{(1-x)^{\alpha}}, \tag{3.2}$$

where $x \equiv \sigma/\sigma_f$ is the normalized stress. The fit yields $\alpha = 0.35 \pm 0.07$, and $\beta = 0.39 \pm 0.09$. In the limit $x \to 0$, there results $R(0) = \beta$, which is statistically indistinguishable from the initial values R_0 observed experimentally.

Now compare the results derived above with damage mechanics model. Looking again at the stress-time diagrams of Fig.3.6, we can assume that the applied stress σ is increased linearly with time

$$\sigma(t) = C\,t, \tag{3.3}$$

where C is a constant. Substitution of Eq. (3.3) into Eq. (3.2) gives

$$R(t) = \frac{\beta}{\left(1-\frac{t}{t_{\mathrm{f}}}\right)^{\alpha}}, \tag{3.4}$$

where $t_f = \sigma_f / C$ is the time of failure. The time evolution $R(t)$ of the electrical resistance is shown in Fig.3.7(a).

Combining Eqs. (3.1) and (3.4), we find power-law scaling of the damage variable D during the approach to failure

$$D(t) = 1 - \frac{R_0}{\beta}\left(1 - \frac{t}{t_f}\right)^{\alpha}. \tag{3.5}$$

The scaling observed in our experiments is the same as that predicted by damage mechanics in the case of linearly time-dependent stress (Turcotte et al., 2002; Turcotte and Shcherbakov, 2003)

$$D(t) = 1 - \left(1 - \frac{t}{t_f}\right)^{1/3}. \tag{3.6}$$

More specifically, the values of parameters α, β and R_0 make the experimental fitting function defined by Eq. (3.5) statistically indistinguishable from the theoretical function defined by Eq. (3.6). This result is in agreement also with the power-law behaviour of cumulative energy associated with acoustic-emission events prior to failure of circular panels of chipboard and fiberglass (Guarino et al., 1998).

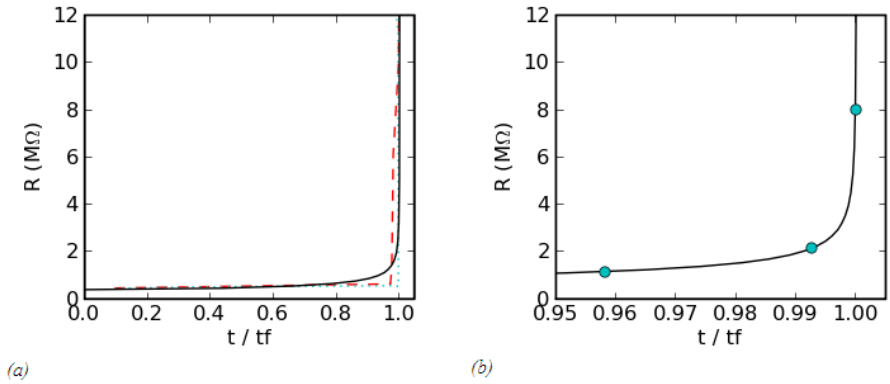

Figure 3.7 – *(a)* Electrical resistance as a function of time to failure t/t_f: dashed and dotted lines represent experimental data from laboratory specimens, while continuous line represents the fitting function given by Eq. (3.4). *(b)* Detail: circles identifying the time to failure t/t_f of the three statues.

3.4 Constant Stress on Terracotta Statues

In-situ damage assessment based on electrical resistance measurements was carried out on three life size terracotta statues located in the Chapel 17 (Fig.3.8), housing the scene of the Transfiguration of Christ on Mount Tabor. The statues present hollows on their hidden sides, appearing polished only on those parts exposed to the gaze of the viewer. They could be at risk of collapse due to the action of harsh environment, including ambient humidity, dust, organic deposits, etc. The resistance was measured on the statues' ankles, which are weak spots due

to their small cross-sections. At the ankle level, the effective load-carrying area element is an annulus of about 30 cm^2. Measured resistances averaged 1.18, 2.16 and 8 MΩ, for the three statues respectively.

The chemical analysis of mortar identified 59.7 wt.% of SiO_2, 21.4 wt.% of CaO, 8.4 wt.% of Fe_2O_3 and 3.3 wt.% of Al_2O_3. This is remarkably close to the chemical composition of historical terracotta, which contents 51.9 wt.% of SiO_2,16.0 wt.% of Al_2O_3, 12.9 wt.% of CaO, 10.3 wt.% of Fe_2O_3 and smaller percentages of other components.

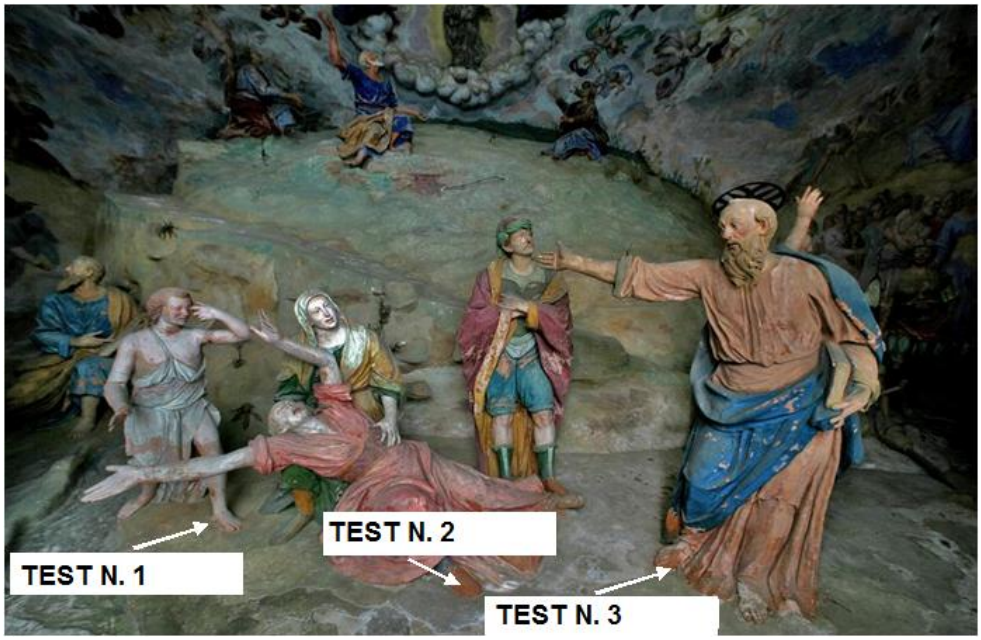

Figure 3.8 – Chapel 17: Labels indicate the monitored portions of terracotta statues.

In the laboratory analysis we considered the case in which the applied stress was a

linearly increasing function of time. Now, we can assume that a constant axial stress σ_0 is applied to the statues' ankles due to dead load.

Generally, if $\sigma_0 \leq \sigma_y$, where σ_y is the yield stress, the material obeys linear elasticity and no damage occurs. If a stress $\sigma_0 > \sigma_y$ is applied and maintained, the material fails in a finite time (Turcotte et al., 2002; Turcotte and Shcherbakov, 2003). The signs of aging and deterioration shown by the statues suggest that stress may exceed the yield limit, especially in the weaker spots.

The close similarity between terracotta ankles and mortar specimens in chemical composition and size suggests analogous electrical properties. Then, it seems reasonable that the electrical resistance of terracotta ankles and mortar specimens could be the same for the particular stress level reached. Furthermore, it has been demonstrated (Turcotte and Shcherbakov, 2003) that dependence of the damage variable D on the time to failure $t/\ t_f$ when the applied stress is constant is given by the same power-law behaviour in Eq. (3.6) for stress increasing linearly with time.

Thus, we can argue that the points specifying the state of the three statues lie on the lifetime curve of mortar specimens. This scaling approach to failure is illustrated in Fig.3.7(b). The predicted values of time to failure $t/\ t_f$ using Eq. (3.4) are 0.957, 0.992 and 0.999 for the three statues, being t = 340 years their age (the last dates back to the 1670s). The residual lifetime of the statues is then estimated, in terms of time $t_f - t$ before the maximum value of electrical resistance is reached in the analyzed elements, at 15, 2.5 and 0.1 years.

Finally, at least one statue seems to require urgent restoration intervention. The application of geopolymer restoration techniques (Hanzlicek et al., 2009) to the unseen part of the statues, ensuring stability and durability without disrupting the aesthetics, may be strongly recommended.

3.5 Concluding Remarks

The damage assessment by means of electrical resistance testing shows agreement with theoretical predictions of continuum damage mechanics. Two cases are considered: (1) the load applied to mortar specimens increases linearly with time from zero until failure and (2) a constant compressive load applied to terracotta statues. Turcotte et al. (Turcotte et al., 2002; Turcotte and Shcherbakov, 2003) theoretically approached the failure of solids using continuum damage mechanics models. They found that the cumulative damage under has a power-law dependence on the time to failure with identical power-law exponent $\alpha = 1/3$ for loading conditions (1) and (2). It is shown that this dependence is in agreement with the solutions obtained in our laboratory experiments using electrical resistance measurements. Furthermore, identical solutions for cases (1) and (2) provide the theoretical support to estimate terracotta statues' residual lifetime by correlating in situ electrical measurements with laboratory measurements.

Thus, the presented methodology should have properly illustrated the need for damaged artworks and more in general for cultural heritage to have a planned preventative maintenance.

Chapter 4

Laboratory Tests for AE Monitoring of Crushing and Fracture Energies in Sculpture and Building Decoration Materials

4.1 Introduction: Compressive Failure Characterization of Heterogeneous Materials

Damage and fracture characterizing the compressive failure of heterogeneous materials such as masonry, marble, rocks in general and concrete are complex processes involving wide ranges of time and length scales, from the micro- to the structural-scale. They are governed by the nucleation, growth and coalescence of microcracks and defects, eventually leading to the final collapse, and to the loss of the classical mechanical parameters, such as nominal strength, dissipated energy density and deformation at failure, as material properties (Carpinteri et al., 2012a). Furthermore, the collapse mechanism is strongly related to the cracking pattern

developing during the loading process. It changes from crushing, for very stocky specimens, to shear failure characterized by the formation of inclined slip bands for intermediate values of slenderness, to splitting for very slender specimens.

Such a variety of failure mechanisms makes the definition of scale-invariant mechanical parameters difficult to be achieved. However, according to experimental evidences (Kotsovos, 1983; Van Mier, 1984), the post-peak phase is characterized by a strong strain localization, independently of the actual collapse mechanism. Consequently, in the softening regime, energy dissipation takes place over an internal surface rather than within a volume, in close analogy with the behavior in tension. According to these evidences, the Overlapping Crack Model (OCM) has been proposed by Carpinteri (Carpinteri et al., 2009a) for modeling the compressive behavior of concrete-like materials. Such a model, dual to the cohesive crack model routinely adopted for quasi-brittle materials in tension, assumes a stress vs. displacement (fictitious interpenetration) law as a material property for the post-peak behavior, to which corresponds an energy dissipation over a surface. This simple model has permitted to explain the well-known size and slenderness effects on the structural ductility, characterizing the mechanical behavior of concrete-like materials subjected to uniaxial and eccentric compression tests (Carpinteri et al., 2009a; Carpinteri et al., 2011a).

The overlapping crack model is very effective in describing the overall behavior of specimens in compression, without going into the details of the cracking pattern, as well as in determining the amount of energy dissipated during the complete loading process. On the other hand, more information on the modalities of energy release and the development of cracking patterns can be obtained on the basis of the acoustic emission (AE) monitoring technique, that proves possible to detect the

occurrence and evolution of stress-induced cracks. Cracking, in fact, is accompanied by the emission of elastic waves which propagate within the bulk of the material. These waves can be received and recorded by transducers applied to the surface of structural elements. This technique, originally used to detect cracks and plastic deformations in metals, has been extended to studies in the field of masonry, rocks and concrete, where it can be used for the diagnosis of structural damage phenomena (Ohtsu, 1996; Carpinteri et al., 2007d). Recently, AE data have been interpreted by means of statistical and fractal analysis (Carpinteri et al., 2007d), showing that the energy release, proportional to the cumulative number of AE events, is a surface-dominated phenomenon. Analogously, also the localization of cracks distribution within the specimen volume by means of the AE technique has physically confirmed the localization of the energy dissipation over preferential bands and surfaces during the damage evolution (Weiss and Marsan, 2003; Carpinteri et al., 2008b; Carpinteri et al., 2008c).

4.2 Theoretical Models

4.2.1 Uniaxial compression

The overlapping crack model proposed by Carpinteri (Carpinteri et al., 2009a) describes the inelastic deformation due to material damage in the post-peak softening regime by means of a fictitious interpenetration of the material, while the bulk material undergoes an elastic unloading. Such a behavior is described by a couple of constitutive laws in compression, in close analogy with the cohesive crack model: a stress vs. strain relationship for the undamaged material (Fig.4.1a), and a stress vs. displacement (fictitious overlapping) relationship describing the

material crushing and expulsion (Fig.4.1b). The latter law describes how the stress in the damaged material decreases by increasing the interpenetration displacement, up to a residual value, σ_r, is reached, to which corresponds the critical value for displacement, w_{cr}. The area below the stress vs. overlapping displacement curve of Fig.4.1b represents the crushing energy, $\mathcal{G}_C$,, which can be assumed, under certain hypotheses, as a size-independent material property.

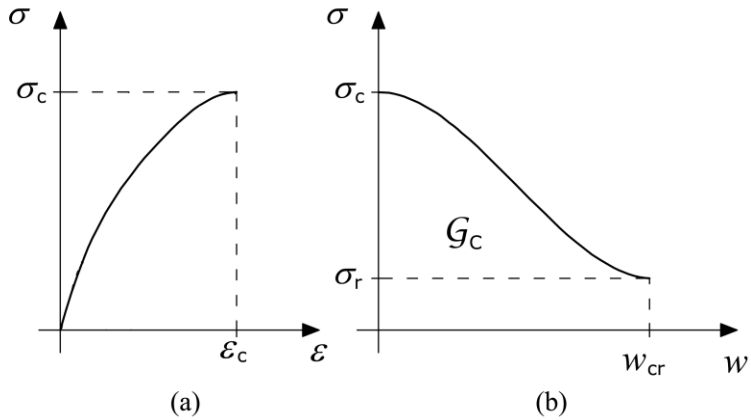

Figure 4.1 – Overlapping Crack Model: *(a)* pre-peak stress vs. strain diagram; *(b)* post-peak stress vs. interpenetration law.

According to the overlapping crack model, the mechanical behavior of a specimen subjected to uniaxial compression (see Fig.4.2) can be described by three schematic stages. A first stage where the behavior is mainly characterized by the elastic modulus of the material: a simple linear elastic stress-strain law can be assumed, or even more complicated nonlinear relationships, taking into account energy dissipation within the volume due to initiation and propagation of microcracks (see Fig.4.2b). By approaching the compressive strength, such microcracks interact forming macrocracks, and, eventually, localizing on a

preferential surface. A second stage where, after reaching the ultimate compressive strength, σ_c, the inelastic deformations are localized in a crushing band. The behavior of this zone is described by the softening law shown in Fig.4.1b, whereas the remaining part of the specimen still behaves elastically (see Fig.4.2c). The displacement of the upper side can be computed as the sum of the elastic deformation and the interpenetration displacement *w*:

$$\delta = \varepsilon l + w \text{ for } w < w_{cr}, \tag{4.1}$$

where *l* is the specimen length. Both ε and *w* are functions of the stress level, according to the corresponding constitutive laws shown in Fig.4.1. While the crushing zone overlaps, the elastic zone expands at progressively decreasing stresses. When $\delta \geq w_{cr}$, in the third stage, the material in the crushing zone is completely damaged and is able to transfer only a constant residual stress, σ_r (see Fig.4.2d).

As a result, very different global responses in the σ–δ diagram can be obtained by varying the mechanical and geometrical parameters of the sample. In particular, the softening process is stable under displacement control, only when the slope $\mathrm{d}\delta/\mathrm{d}\sigma$ in the softening regime is negative, Fig.4.3a. A sudden drop in the load bearing capacity under displacement control takes place when the slope is infinite, Fig.4.3b. Finally, the snap-back instability is avoided, Fig.4.3c, if the loading process is controlled by means of the localized interpenetration or the circumferential strain, the slope $\mathrm{d}\delta/\mathrm{d}\sigma$ of the softening branch being positive. Analogously to quasi-brittle materials subjected to tension, the stability of the overall behavior of specimens in compression depends on geometrical (size and slenderness) and mechanical parameters (crushing energy, compressive strength

and ultimate strain). In accordance with previous studies proposed by the authors in (Carpinteri et al., 2011a), a catastrophic softening (snap-back) occurs when:

$$B = \frac{s_E}{\varepsilon_c \lambda} \leq \frac{1}{2.3}, \tag{4.2}$$

where $\lambda = l/d$ is the specimen slenderness, ε_c is the elastic strain recovered during the softening unloading, and

$$s_{E,C} = \frac{G_C}{\sigma_c d}, \tag{4.3}$$

is the energy brittleness number in compression, proposed by Carpinteri (Carpinteri et al., 2011a).

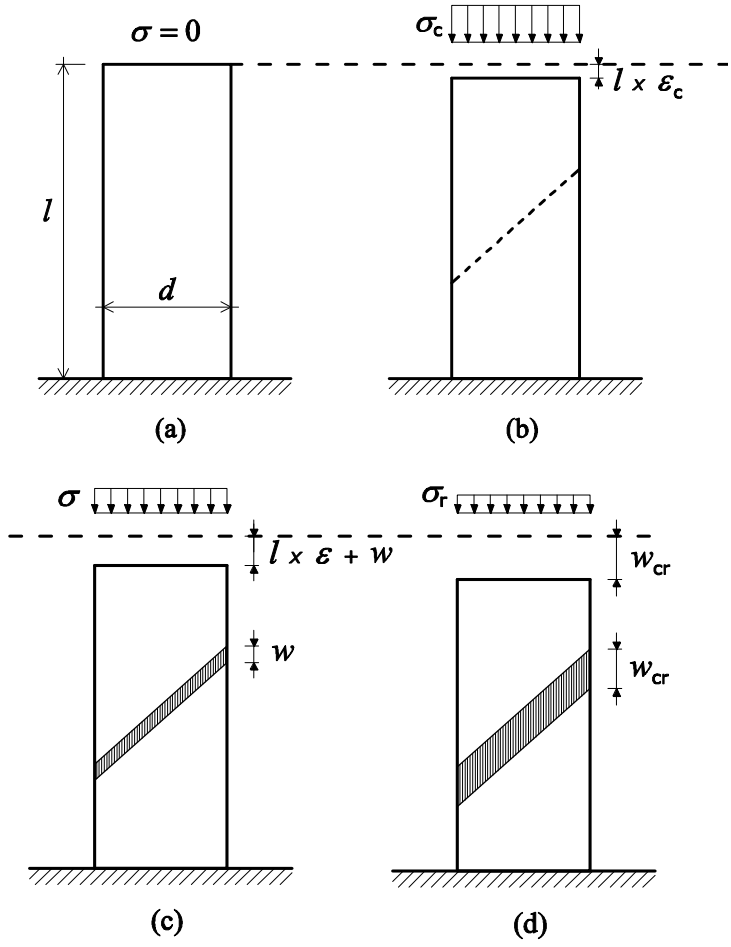

Figure 4.2 – Subsequent stages in the deformation history of a specimen in compression.

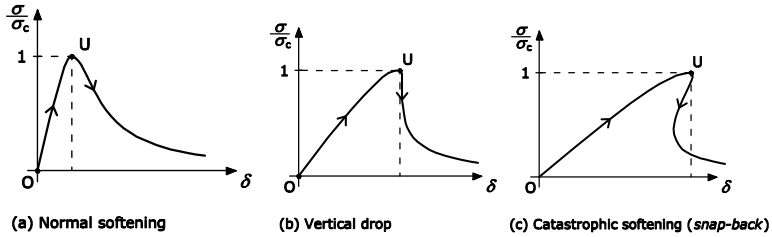

Figure 4.3 – Stress vs. displacement response of a specimen in compression.

An extended validation of the overlapping crack model for concrete-like materials can be found in Carpinteri (Carpinteri et al., 2011a), where specimens of different materials as well as different slenderness and/or size have been considered. For example, the overlapping laws obtained from the results of the compression tests on specimens with different sizes and slendernesses carried out by Ferrara and Gobbi (Ferrara and Gobbi, 1995) are shown in Fig.4.4. The post-peak regime in the stress vs. strain response is largely influenced by the slenderness and the scale of the specimen (Fig.4.4b), whereas the stress vs. displacement curves collapse onto a very narrow band (see fig.4.4c), demonstrating that the σ–w relationship is able to provide a slenderness and size-scale independent constitutive law.

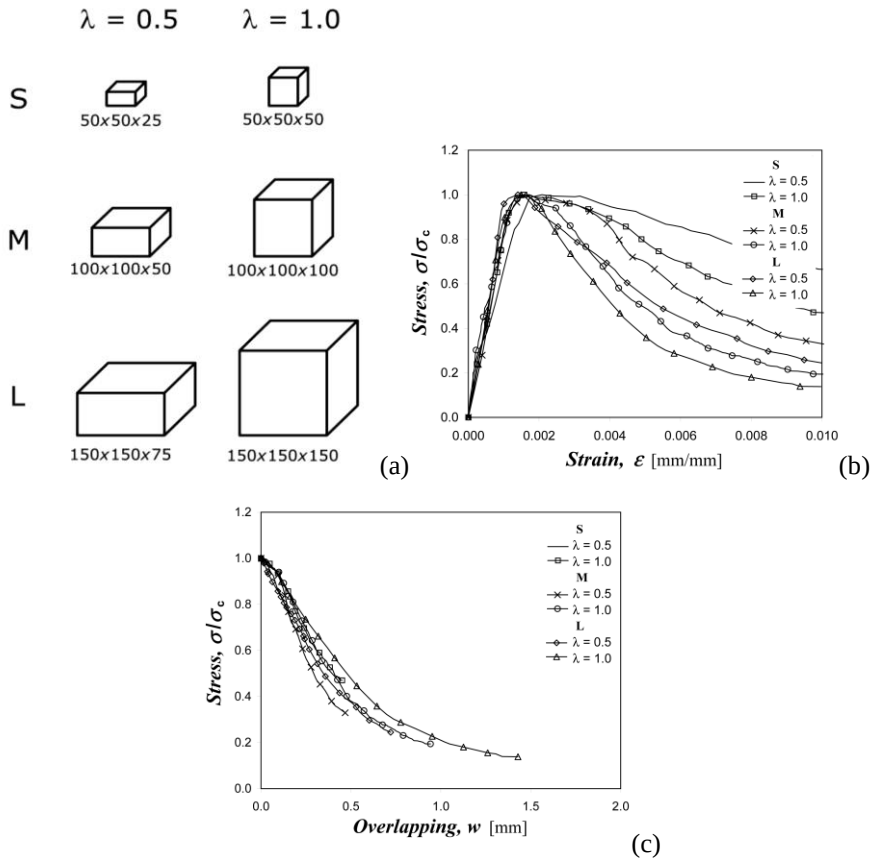

Figure 4.4 – Compression tests on concrete specimens: *(a)* specimens geometry; *(b)* stress vs. strain diagrams; *(c)* overlapping law diagrams.

However, it is to be noted that the overlapping crack model, considered as a scale-invariant constitutive model, is no longer valid when the collapse mechanism significantly changes. In this case, the cracking pattern and the amount of energy dissipation also change significantly. As an example, the shear collapse mechanism determines an high energy dissipation due to friction phenomena

spread within the specimen volume. On the contrary, the splitting failure, typical of slender specimens, gives rise to a lower energy dissipation, due to the propagation of a main longitudinal tensile crack. The stability of the compression phenomenon is still governed by Eq. (4.2), although the crushing energy depends on the failure mechanism.

4.2.2 Three-point bending

From a theoretical point of view, the three-point bending test of plain concrete-like beams can be described by means of the cohesive crack model. A linear-elastic behavior is assumed for the beam up to the maximum tensile stress in the central cross section reaches the ultimate strength. Then, a cohesive crack starts to propagate from the soffit to the extrados of the beam, whereas the rest of the body exhibits an elastic unloading. However, due to the complexity of the process, only the initial linear elastic behavior and the limit case of central cross section completely cracked can be analytically studied (see Fig.4.5) (Carpinteri, 1989). More in details, a linear load vs. deflection relationship is obtained for the former phase, whereas a more complex curve characterizes the post-peak softening phase (Fig.4.6). Analogously to the compression test, the stability of the loading process is governed by a nondimensional parameter. Unstable behavior and catastrophic events are expected when (Carpinteri, 1989):

$$\frac{s_{\mathrm{E,t}}}{\varepsilon_{\mathrm{u}}\lambda} \leq \frac{1}{3}, \tag{4.2}$$

where $\lambda = l/d$ is the beam slenderness, ε_u is the ultimate strain in tension, and $s_{\mathrm{E,t}}$ is the energy brittleness number in tension, proposed by Carpinteri (Carpinteri, 1989). The system is brittle for low brittleness number, high ultimate strain and

large slenderness (Fig.4.6).

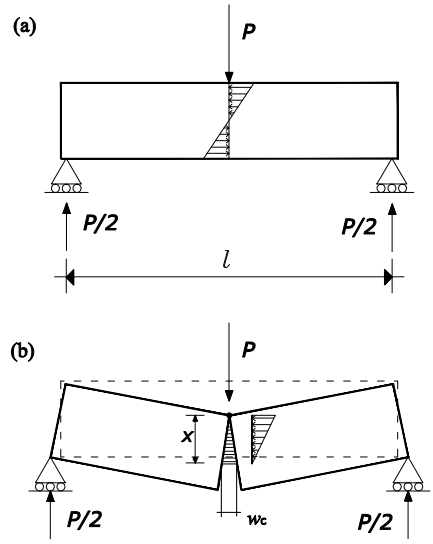

Figure 4.5 – Three-point bending geometry: *(a)* linear elastic phase; *(b)* limit situation of complete fracture with cohesive forces.

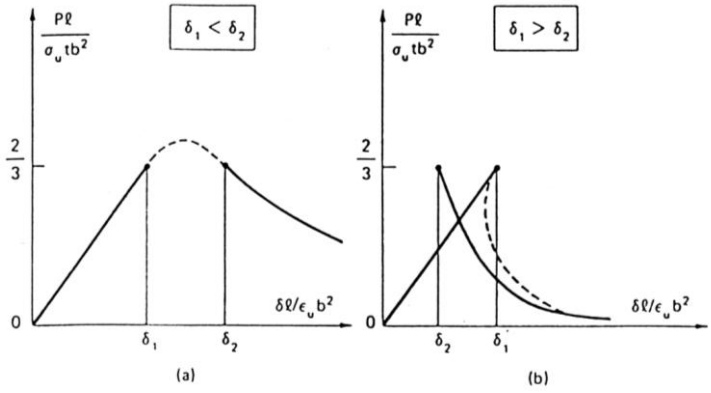

Figure 4.6 – : Load–deflection diagrams: *(a)* ductile; *(b)* brittle condition ($\delta_1=\lambda^3/6$; $\delta_2=s_{E,t}\lambda^2/2\varepsilon_u$).

4.3 Acoustic Emission Testing

The estimation of active cracks is of significant importance for any structural inspection. For an early warning of crack nucleation, the classification of active cracks is a great deal of the AE technique (Grosse and Ohtsu, 2008).

AE signals due to microcracks are detected by AE sensors attached on the surface of the specimen. The signal waveforms are recorded by the AE measurement system. In order to classify active cracks, AE parameters such as rise time and peak amplitude of each signal are considered to calculate the rise angle (RA) value, defined as the ratio of the rise time (expressed in ms) to the peak amplitude (expressed in V) (Grosse and Ohtsu, 2008; RILEM, 2010a; RILEM, 2010b; RILEM, 2010c).

The shape of the AE waveforms is typical of the fracture mode (Fig.4.7). Shear events are characterized by long rise times and usually high amplitudes (Ohno and Ohtsu, 2010; Soulioti et al., 2009; Aggelis, 2011b; Aggelis et al., 2012e; Carpinteri et al., 2013c), whereas low rise time values are typical of tensile crack propagations (Soulioti et al., 2009; Aggelis, 2011a; Aggelis, 2011b; Aggelis et al., 2012e; Carpinteri et al., 2013c). These conditions are synthesized by the RA value (Aggelis, 2011b; Aggelis et al., 2012d; Aggelis et al., 2012e; Carpinteri et al., 2013c).

Another parameter used to characterize the cracking mode is the Average Frequency (AF) expressed in kHz. The AF values are obtained from the AE ringdown count divided by the duration time of the signal. The AE ringdown count

corresponds to the number of threshold crossings within the duration time. In general, the shift from higher to lower values of AF could indicate the shift of the cracking mode from tensile to shear (Ohno and Ohtsu, 2012). Nevertheless, when a cracking process involves the opening of large cracks (Mode I), the frequency attenuation must be a function of this discontinuity. In other words, in this case the wavelength of the AE signals needs to be larger for the crack opening to be overcome, and the shift of the frequencies from higher to lower values could support also a dominant tensile cracking mode (Landis and Shah, 1995; Carpinteri et al., 2007d; Carpinteri et al., 2013c).

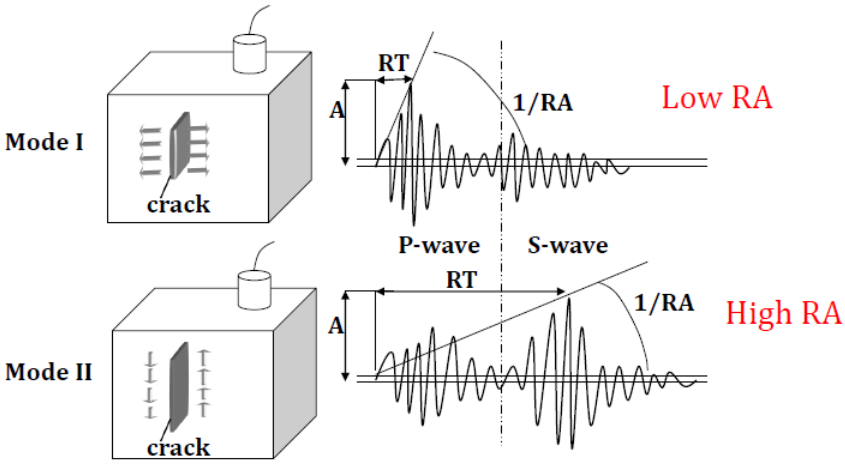

Figure 4.7 – : Typical waveforms of tensile and shear events. *A* is the amplitude and *RT* the rise time (time between the onset and the point of maximum amplitude) of the waveforms (Aggelis et al., 2012d).

4.4 Experimental Tests

4.4.1 Uniaxial compression

The experimental investigation herein presented focuses on the mechanical response of cylindrical specimens of different heterogeneous materials, such as rocks and concrete, subjected to uniaxial compression tests. As regards the rock specimens, three different types have been tested: Luserna stone, Carrara marble, and Syracuse limestone. Luserna stone is a lamellar metamorphic rock deriving from a granitoid protolith quarried in Piedmont (Italy). Carrara marble is a type of white or blue-grey calcite marble quarried in Carrara (Tuscany, Italy) popular for use in sculpture and building décor. Syracuse limestone is a porous calcareous stone obtained from quarries in the area of Plemmirio (Sicily, Italy). All the three rock samples have a slenderness $\lambda = 2.0$, being the diameter $d = 50$ mm and the length $l = 100$ mm. As regards the concrete specimen, a normal strength concrete has been considered, having an average compressive strength equal to 45 MPa. The slenderness of the sample is again $\lambda = 2.0$, though the diameter is equal to 100 mm and the length to 200 mm.

On the basis of previous experiences, a very brittle behaviour, characterized by a snap-back instability, was expected for the Luserna specimen, an intermediate response for the Carrara marble and the normal concrete samples, and a ductile behaviour for the limestone. On the other hand, a correct evaluation of the dissipated and released energies during the complete loading process can be done only if the load–displacement curve is fully detected, post-peak branch included. To this purpose, the loading processes of the Luserna stone, the Carrara marble and the concrete specimens have been controlled by the circumferential strain, that

results to be a monotonic increasing function of time, even in case of global brittle behaviour. An extensometer attached to the ends of a linked chain with roller at each hinge was placed around the cylinders at mid-height, measuring the circumferential expansion. Such a device is particularly effective in controlling the post-peak phase for specimens with slenderness of about 2.0, characterized by a splitting failure mode. The velocity of the circumferential expansion has been set equal to $1x10^{-3}$ mm/s for the Luserna specimen, to $5x10^{-4}$ mm/s for the Carrara specimen, and $2x10^{-3}$ mm/s for the concrete sample. Due to the expected ductile behaviour for the limestone specimen, its loading process was controlled by the longitudinal displacement (piston stroke). In this case, a constant piston velocity was imposed, equal to $1x10^{-3}$ mm/s. In all the cases the load has been applied by means of rigid platens without interposing friction-reducer devices. At this regard, it is worth noting that there is vast amount of literature confirming that the friction effects are very limited in the case of sample slendernesses equal to or larger than 2.0. During the tests, each specimen was monitored by applying a piezoelectric transducer on the sample surface in order to detect acoustic emissions emerging from the compression process. The sensitivity range for the transducer is from 50 to 800 kHz, making possible the detection of high-frequency AEs. The sampling frequency of recording waveforms was set to 1 Msample/s. The AE waves, captured by the sensors, were amplified with 60 dB gain before they have been processed, setting the acquisition threshold level up to 2 mV.

The load vs. circumferential and longitudinal displacement curves obtained from the tests are shown in Figs.4.8a-4.11a. The mechanical response of the Luserna stone is highly unstable in terms of load vs. axial displacement, whereas a global softening behaviour with the presence of several peaks and valleys is obtained in

terms of load vs. circumferential expansion (Fig.4.8a). Carrara marble and normal concrete are characterized by a load vs. axial displacement with perfect vertical drop after the peak load and a smooth softening curve in the load vs. circumferential expansion diagram (Figs.4.9a and 4.10a). Finally, a ductile response in the load vs. axial displacement diagram has been obtained for the Syracuse limestone specimen (Fig.4.11a).

As far as the acoustic emission activity is concerned, in the Luserna stone specimen it is mainly concentrated in the post-peak stage, as clearly evidenced by the cumulated number of AE and the AE count rate diagrams shown in Figs.4.8b,c. The cumulated number of AE events referred to the post-peak regime is about 3200. Analogously, also the Carrara marble and the concrete samples have exhibited significant AE events in the post-peak, even if the cumulated numbers are one order of magnitude lower than that of the Luserna stone (300 for marble and 160 for concrete, as can be deduced from Figs.4.9 and 4.10). On the contrary, almost all of the AE events in the limestone specimen has been detected in the pre-peak stage, as shown in Fig.4.11b. As regards the post-peak regime, the cumulated number of AE is around 400.

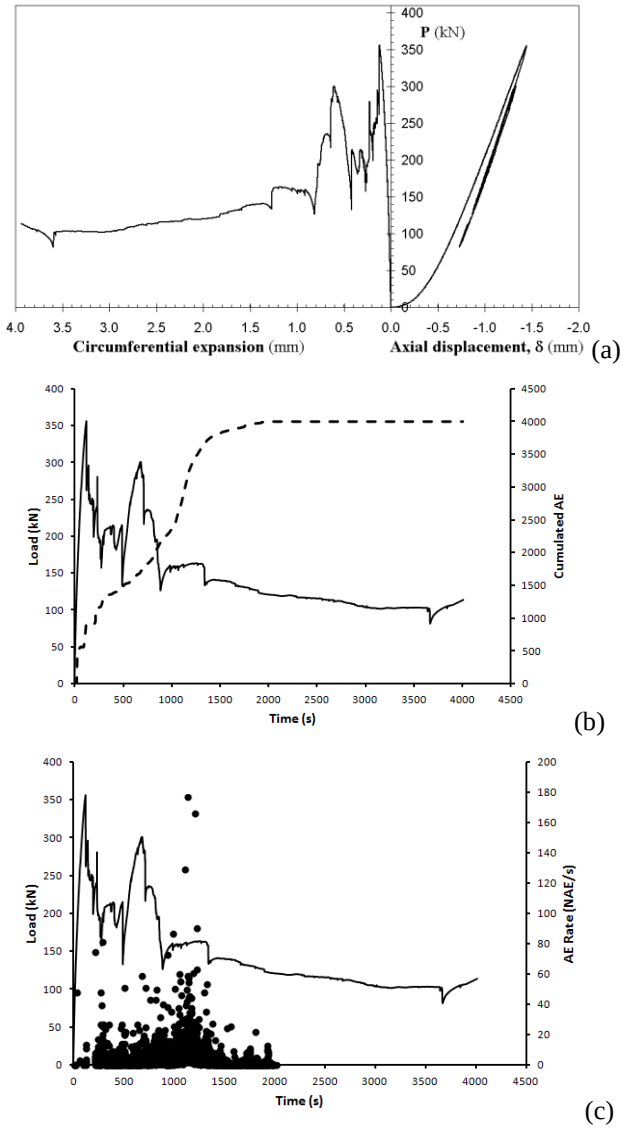

Figure 4.8 – Compression test on the Luserna stone specimen (d = 50 mm, l = 100 mm): *(a)* load vs. circumferential expansion and longitudinal displacement diagrams; *(b)* load vs. time curve with cumulated number of AE and, *(c)* AE count rate.

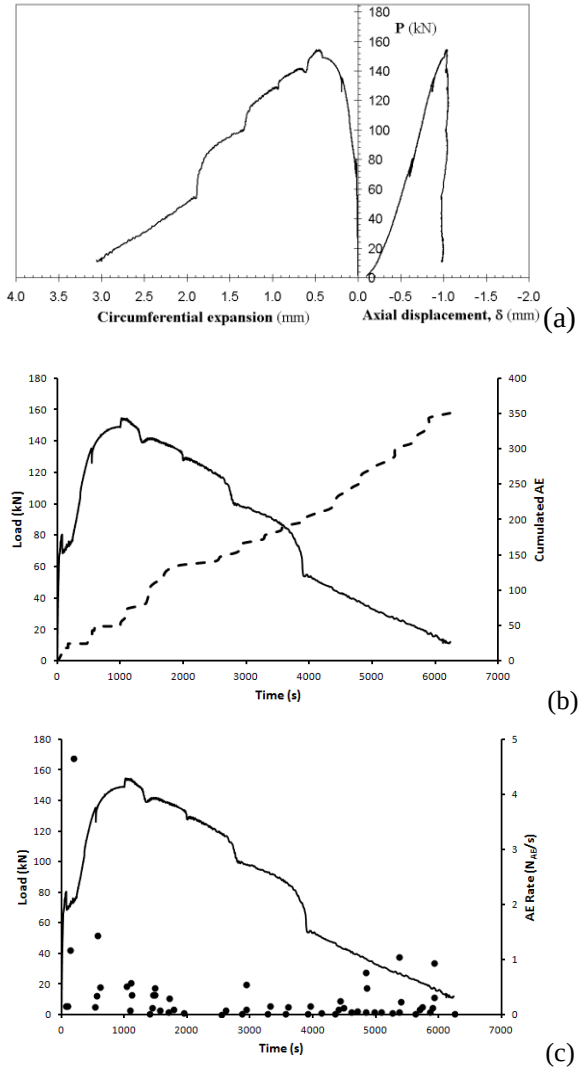

Figure 4.9 – Compression test on the Carrara marble specimen (d = 50 mm, l = 100 mm): *(a)* load vs. circumferential expansion and longitudinal displacement diagrams; *(b)* load vs. time curve with cumulated number of AE and, *(c)* AE count rate.

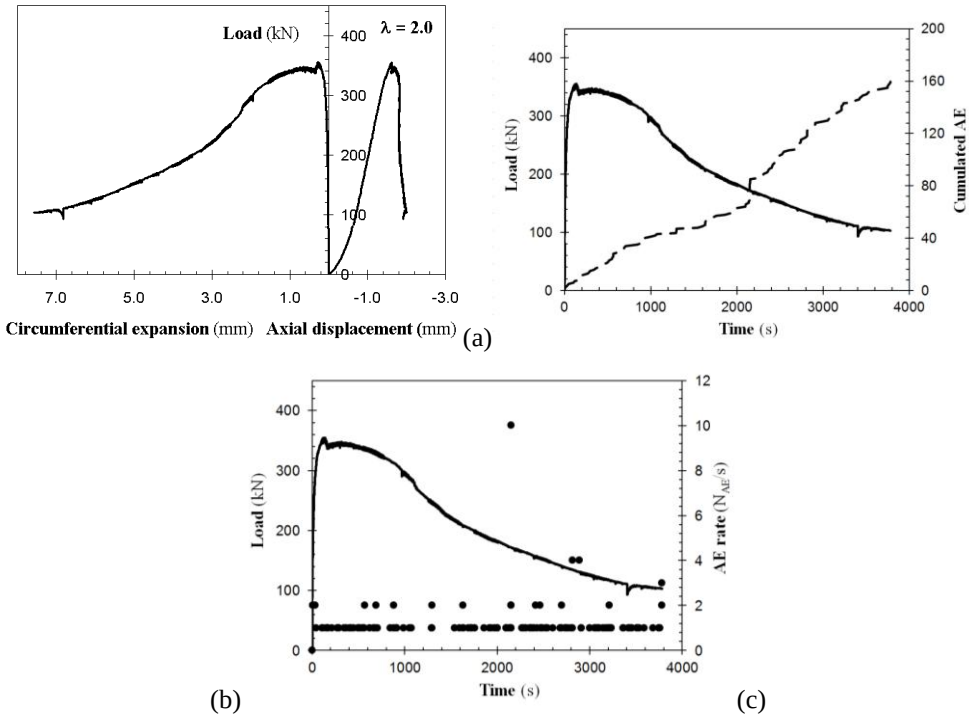

Figure 4.10 – Compression test on the concrete specimen with slenderness λ = 2.0 (d = 100 mm, l = 200 mm): *(a)* load vs. circumferential expansion and longitudinal displacement diagrams; *(b)* load vs. time curve with cumulated number of AE and, *(c)* AE count rate.

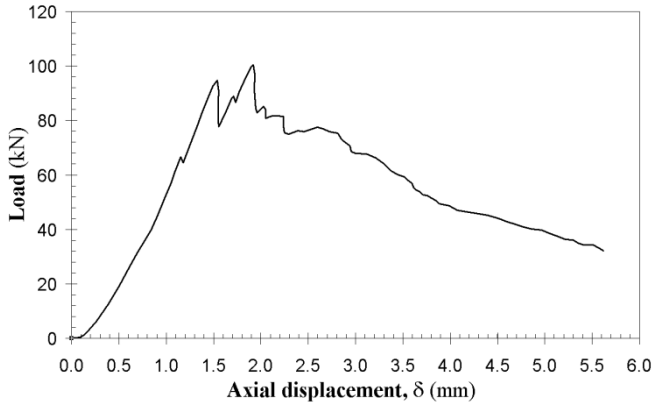

(a)

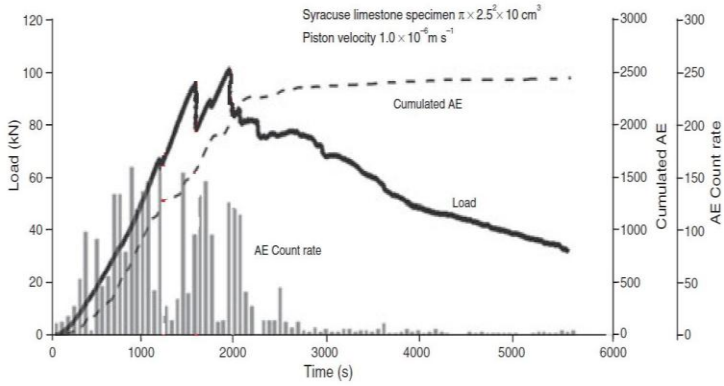

(b)

Figure 4.11 – Compression test on the Syracuse limestone specimen (d = 50 mm, l = 100 mm): *(a)* load vs. longitudinal displacement diagram, and *(b)* load vs. time curve with cumulated number of AE and AE count rate.

4.4.2 Stability of the Loading Process and Energy Release

The mechanical responses obtained for the considered materials can be referred to the three cases shown in Fig.4.3: normal softening, vertical drop and snap-back instability. Such a transition can be obtained either by varying the specimen geometry, the material being the same, or, as in this study, by varying the material properties and keeping the geometric parameters constant. The procedure described in the Section "Scale independent constitutive laws" has been used to derive the overlapping laws for the four considered materials. They are shown in Fig.4.12, in terms of normalized stress vs. overlapping displacement. The values of the strength, the critical interpenetration displacement and the crushing energy are reported in Table 4.1. The crushing energy $\mathcal{G}_C$ has been evaluated as the area beneath the overlapping law comprised between the peak stress, σ_c, and a residual stress equal to $0.2\sigma_c$. On the basis of these mechanical properties and the specimen diameter, the energy brittleness number s_E has been computed for each specimen. The lowest value is that of the Luserna stone sample, equal to 0.0016, and the largest one is that of the Syracuse limestone sample, equal to 0.065. The marble and the concrete specimens present intermediate values for s_E, equal to 0.0065 and 0.0095. The values of the parameter B, defined in Eq.(4.2), are also reported in Table 4.1. They completely agree with the critical condition defined by Eq.(4.2): snap-back instability for $B < 0.43$, and normal softening for $B > 0.43$. The Carrara marble specimen, characterized by a vertical drop in the load–displacement diagram, has $B = 0.41$.

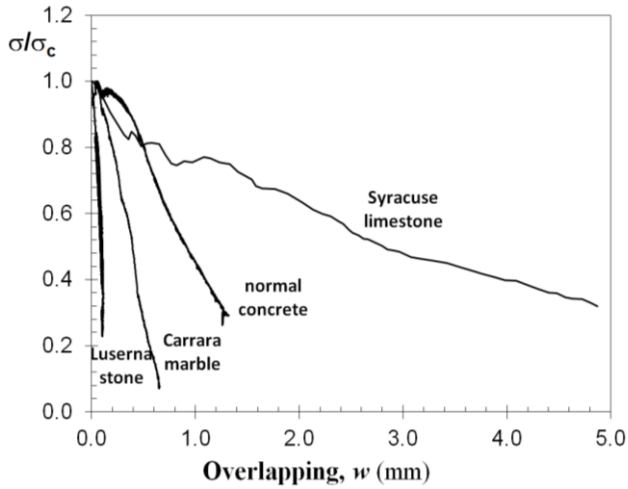

Figure 4.12 – Overlapping constitutive laws for Luserna stone, Carrara marble, Syracuse limestone and normal concrete specimens in compression.

	σ_c (MPa)	ε_c	w_{cr} (mm)	$\mathcal{G}_C$ (N/mm)	s_E	B	$\mathcal{G}_C$ x Area (J)	ΔE (J)
Luserna stone	168	0.0105	0.12	13.90	0.0016	0.079	29.51	186.40
Carrara marble	75	0.0080	0.60	25.35	0.0065	0.410	49.57	57.75
Normal concrete	45	0.0077	1.60	43.00	0.0095	0.620	337.72	272.14
Syracuse limestone	51	0.0180	6.00	165.00	0.0650	1.889	323.89	85.42

Table 4.1 – Mechanical parameters for the three considered materials.

According to the OCM, the energy absorbed in the post-peak phase by the damaging process is equal to the crushing energy times the transversal cross section of the specimen. The values for the four samples are reported in Table 4.1. On the other hand, the elastic strain energy at the peak load, ΔE, represents the maximum energy stored in the specimen, that will be partially absorbed and partially released during the post-peak phase. As can be deduced from the results reported in Table 4.1, the Luserna specimen releases an energy equal to 156.89 J, and the Carrara sample to 8.18 J. On the contrary, the concrete and the limestone specimens requires a supplementary amount of energy, to be provided by the testing machine, for the advancement of the post-peak damaging process (65.58 J and 238.47 J, respectively). As regards the Carrara marble specimen, the value of the crushing energy multiplied by the cross-sectional area is not exactly equal to ΔE, even if the load–displacement diagram has a vertical drop, because the crushing energy is computed up to the residual stress $\sigma_r = 0.2\ \sigma_c$, and not up to a complete failure. The obtained experimental results evidence that the AE activity in the post-peak phase can be directly related to the energy release. The largest number of AE events, in fact, has been detected for the Luserna stone specimen, which, according to the previous calculations, is that releasing the largest amount of energy. Limited AE events have been detected from the Carrara marble specimen, for which the accumulated and the absorbed energies are almost the same, whereas a low AE activity in the post-peak regime has been observed for the limestone specimen.

4.4.3 AE Analysis to Discriminate the Failure Mechanisms

All the specimens described in the previous sections, having a slenderness equal to 2.0, were characterised by a splitting failure, i.e. dominant Mode I failure. In order to verify the capability of the AE in discriminating the types of failure, another specimen of normal concrete, having a diameter equal to 100 mm and slenderness equal to 1.0, has been tested. In this case, the loading process has been controlled by the circumferential strain up to the maximum displacement for the extensometer (point A in Figs.4.13a,b), then, the test control has been switched to the piston stroke.

The load vs. circumferential expansion and the load vs. axial displacement curves for the specimen having slenderness equal to 1.0 are shown in Fig.4.13a. The obtained overall behaviour results to be more ductile then that of the specimen with slenderness equal to 2.0, the post-peak regime being characterized by a normal softening response. Such a result is consistent with the prediction given by the parameter B defined in Eq. (4.2). In this case, in fact, it is equal to 1.24, twice the value referred to the previous specimen. However, the two failure mechanisms are very different: a shear failure with several slip bands characterizes the specimen with $\lambda = 1.0$, whereas a splitting failure is obtained for the specimen with $\lambda = 2.0$. Furthermore, the behaviour of the specimen less slender is also affected by the friction between loading platens and specimen ends. Such an effect yields to an increase in the load carrying capacity and in the energy dissipation.

In this section, AE parameters above mentioned such as rise time, peak amplitude and average frequency are analyzed in order to classify active cracks.

In the case of $\lambda = 1.0$, the cumulative number of AE events at the end of the test is larger than the case with $\lambda = 2.0$ (see Fig.4.13b compared to Fig.4.10b),

representing a higher energy dissipation due to friction. The AE average frequencies decrease from 230 kHz to 190 kHz during the loading test. The load process involves a small shift in frequencies from higher to lower values (Fig.4.14a) and a significant increase in RA values after the peak load is come out (Fig.4.14b). Therefore a dominant presence of shear cracks seems to lead the damage evolution up to the final collapse. The analysis of the energy content obtained by the AE signals (Fig.4.14c), calculated as proportional to the envelope of the signal waveform [8], verifies that the damage evolution carries more powerful signals after the peak load, when the final collapse is approaching. During this test, the amount of released AE signals energy is estimated as 1460 $ms \cdot V \cdot 10^3$.

As regards the specimen with slenderness λ = 2.0, the AE average frequencies decrease from 100 kHz to 50 kHz during the loading test (Fig.4.15a). The loading process involves a shift in frequencies from higher to lower values and a significant decrease in RA values after the peak load (Fig.4.15b). Therefore a dominant presence of tensile cracks seems to lead the damage evolution up to the final collapse. Due to the slenderness of the specimens and the failure mode shown during the experiment (a single large subvertical crack), the shift in frequencies tends to very low values. As a matter of fact, for high frequency waves it is possible to propagate only through small inhomogeneities, whereas low frequency waves can propagate also through large inhomogeneities (Landis and Shah, 1995; Carpinteri et al., 2007d). From the analysis of the energy content obtained from AE signals (Fig.4.15c), also in this case it is verified that the damage evolution carries more powerful signals after the peak load. The amount of released AE signals energy at the end of the test, estimated as 680 $ms \cdot V \cdot 10^3$, is lower than the

previous case.

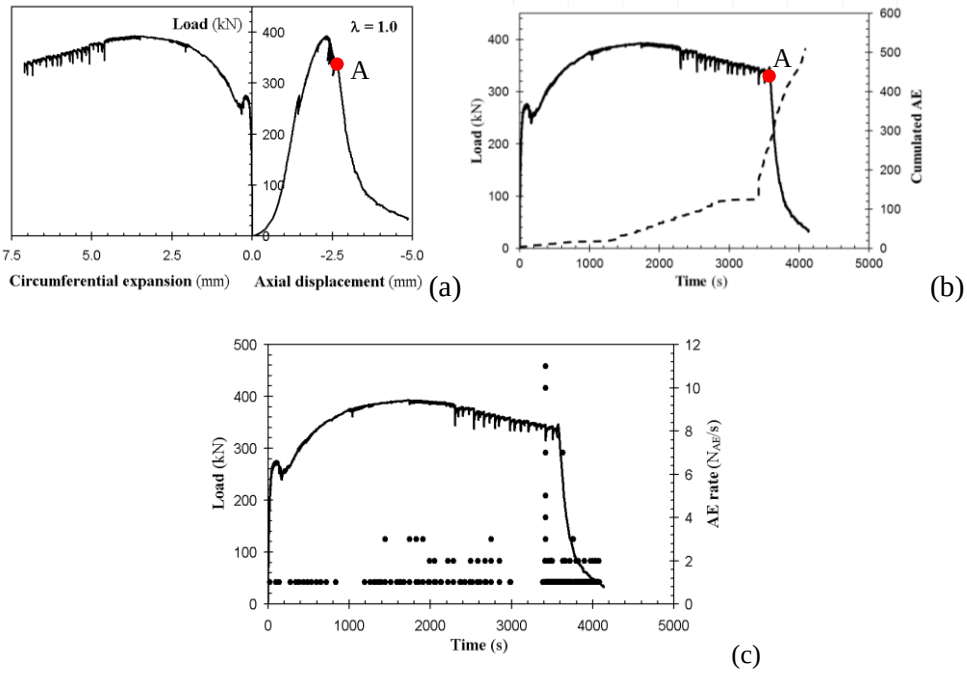

Figure 4.13 – Concrete specimen with slenderness λ = 1.0 (d = 100 mm, l = 100 mm): *(a)* load vs. circumferential expansion and longitudinal displacement diagrams; *(b)* load vs. time curve with cumulated number of AE; *(c)* AE count rate.

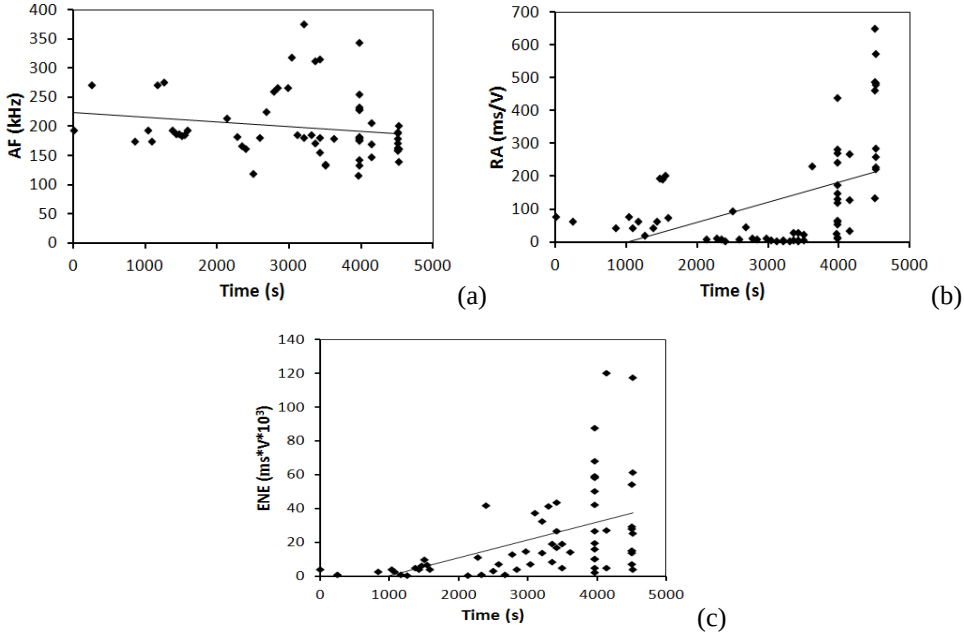

Figure 4.14 – Concrete specimen with slenderness λ = 1.0: *(a)* AF values vs. time; *(b)* RA values vs. time; *(c)* AE signal energy vs. time.

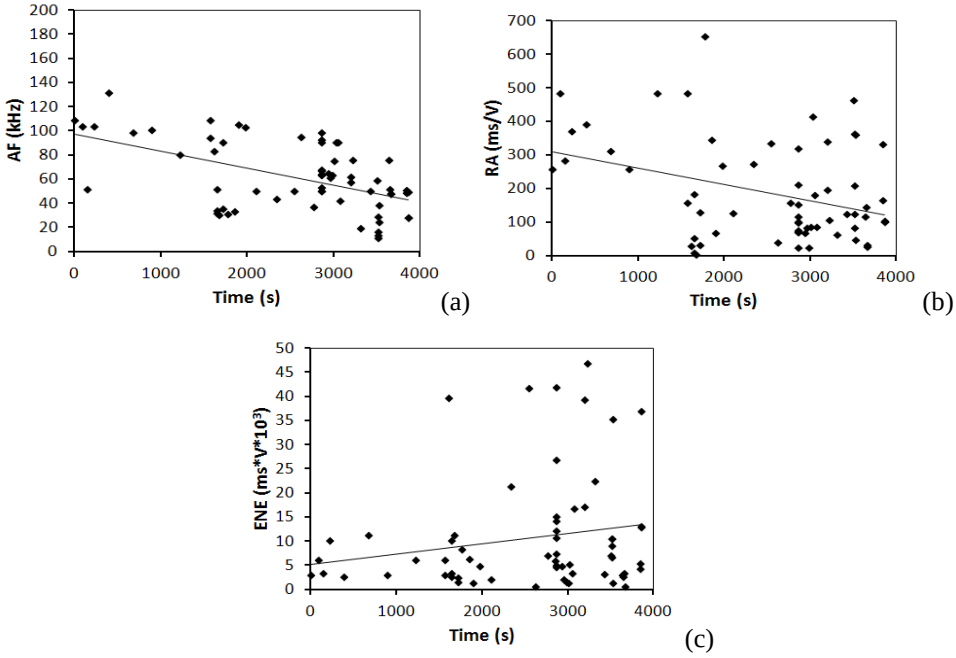

Figure 4.15 – Concrete specimen with slenderness λ = 2.0: *(a)* AF values vs. time; *(b)* RA values vs. time; *(c)* AE signal energy vs. time.

4.4.4 Three-point bending

The results of the three-point bending test performed on a beam having dimensions 100x100x840 mm (Fig.4.16a) are herein reported. From the mechanical point of view, the overall behavior is characterized by a normal softening post-peak phase, as shown in Fig.4.16b. The fracture energy, evaluated according to the RILEM recommendations (RILEM, 1986), is equal to 0.124 N/mm. The corresponding total dissipated energy is equal to 0.62 J.

The AE signals detected from an array of six sensors show characteristics similar

to those of the specimen with slenderness λ=2.0 subjected to compression test. The AE average frequencies range between 180 kHz and 150 kHz (Fig.4.17a). A shift in frequencies from higher to lower values (Fig.4.17a) and a significant decrease in RA values (Fig.4.17b) after the peak load are observed (Fig.4.18b). The evolution of the damage from the initial notch towards a Mode I crack is proved both by the RA and the AF decrease, as in the case of the specimen with slenderness λ=2.0 in compression.

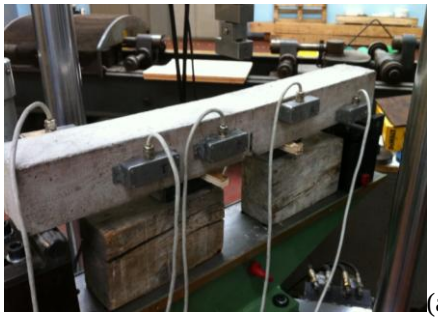
(a)

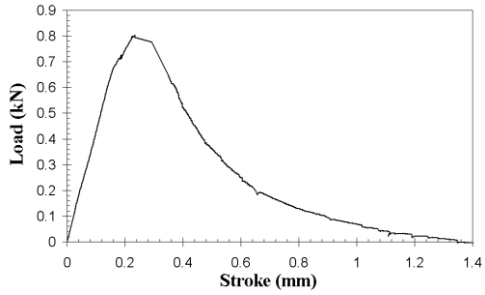

(b)

Figure 4.16 – Three-point bending test: *(a)* experimental setup; *(b)* load vs. deflection curve.

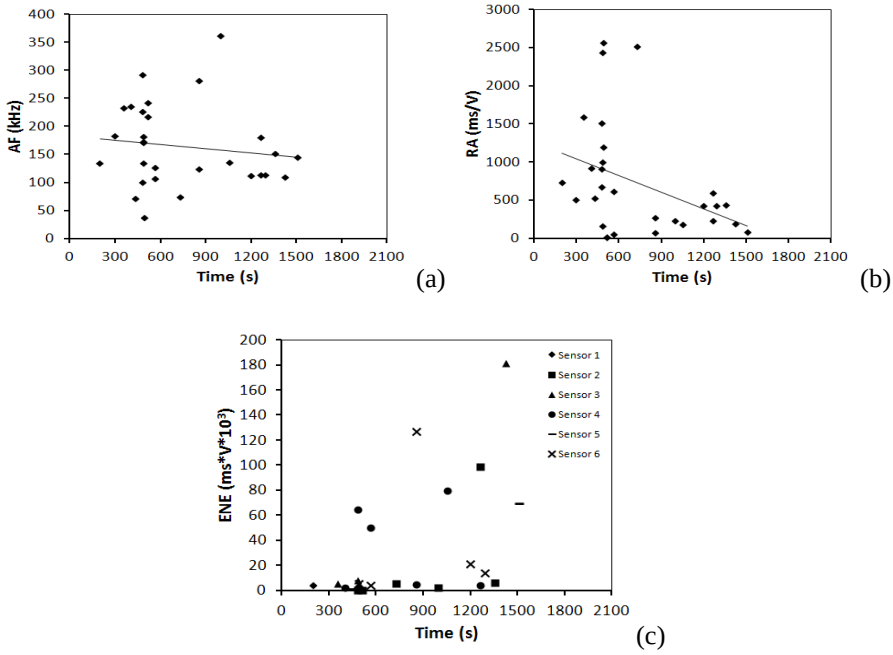

Figure 4.17 – Three-point bending test: *(a)* AF values vs. time; *(b)* RA values vs. time; *(c)* AE signal energy vs. time.

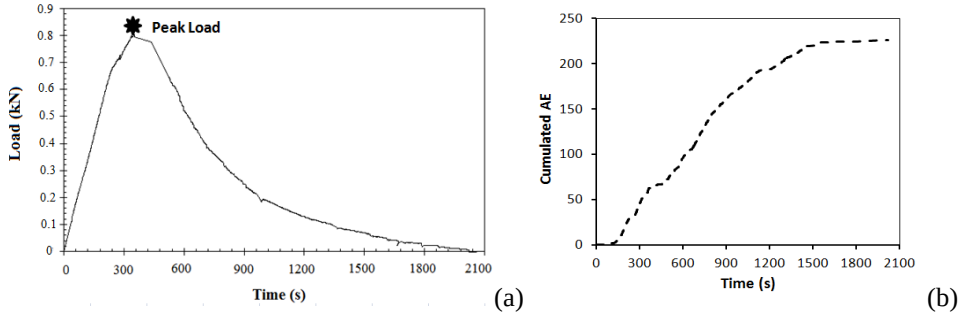

Figure 4.18 – Three-point bending test: *(a)* load vs. time; *(b)* cumulated AE events vs. time.

The RA values obtained from the three-point bending test are considerably higher than the previous two cases, because of the bigger specimen size: as a matter of fact the additional propagation distance from AE sources to sensors, considering attenuation mechanisms, involves an increase in AE signals rise time (Aggelis et al., 2012d; Carpinteri et al., 2013c). Since the longitudinal waves are the fastest type, the delay in each AE signal between longitudinal and shear waves grows with the increasing of the propagation length, and consequently the RA raises from lower to higher values.

The signal energy of the AE events detected during the test are reported in Fig.4.17c, distinctly for each sensor. The average value of the total released AE signals energy is estimated as 126 ms·V·10^3.

4.5 Concluding Remarks

The results of compression tests carried out on cylindrical specimens of sculpture and building decoration materials have been analyzed considering the stability of the loading process and the relationship between absorbed and released energy during the post-peak phase. The following main conclusions may be drawn:

1. The use of the circumferential strain as controlling parameter of the compression tests permits the post-peak branch to be detected, also for a very brittle material such as Luserna stone. This is fundamental to derive the scale-invariant overlapping constitutive law by applying the inverse of Eq. (4.1), that, in its turn, is useful to define the structural brittleness, represented by the dimensionless parameter *B* defined by Eq. (4.22). In particular, for the considered specimen dimensions, Luserna stone results to be the most brittle, and Syracuse

limestone the most ductile.

2. The results depicted in Figs.4.8-4.11 show how the number of AE events in the post-peak regime is proportional to the released energy, that is evaluated as the difference between the elastic strain energy at the peak load and the energy absorbed by the crushing process.

3. The AE results obtained from compression prove that the variation of the AE parameters during the loading process strictly depends on the specimen damage: a decrease in the frequency coupled to low RA values suggest a Mode I crack propagation, whereas a decrease in the frequency coupled to high RA values are obtained in case of Mode II crack propagation. All the monitored damage processes display an increase of AE signal energy content approaching the final failure.

Chapter 5

Conclusions

In order to assess the evolution of the phenomena of cracking and degradation of the high valuable frescos, which tend to detach from the masonry support of Chapel XVII of the Sacred Mountain of Varallo (Italy), the results of the Acoustic Emission monitoring program have been provided, together with structural finite element simulations and complementary laboratory tests.

The Finite Element analysis of Chapel XVII provided the basic mechanism which caused two main cracks in the internal walls. The results of the AE monitoring show that the large cracks are stable, while the process of detachment of the frescos is evolving cyclically. It seems that the frescos degradation could be mainly related to the diffusion of moisture in the mortar substrate. Some laboratory tests also confirm that Acoustic Emissions are recorded in mortar samples subjected to moisture diffusion.

Besides the canonical use in non-destructive tests, the heuristic potential of AE monitoring of historical structures for earthquakes prediction appears very intriguing. Starting from the assumption that any structure should not be regarded as separated from its environment, a method of correlating AE activity on the

Chapel XVII of the Sacred Mountain of Varallo subjected to a long-term monitoring with regional seismicity is investigated. Two qualitatively very similar phenomena such as Acoustic Emission and earthquakes become two aspects of a unique phenomenon, which looks self-similar. Furthermore, by applying the modified Grassberger-Procaccia correlation algorithm −with the aim of explaining the correlation between regional seismicity and Acoustic Emission emerging from Chapel XVII− it is observed that the structure behave as sensitive receptors for earthquakes occurring within a radius of about 100 km, distinguishing environmental contributions to AE activity on the Chapel XVII due to crustal trembling (external source) from contributions due to structural damage (inner source). An accurate finite element model, performed with DIANA® finite element code for the dynamic analysis of Chapel XVII structure, is utilized to confirm visual inspections and monitoring results of the earthquakes effects.

Concerning the valuable artworks kept in Chapel XVII, the damage assessment by means of electrical resistance testing shows agreement with theoretical predictions of continuum damage mechanics. We consider two cases: (1) the load applied to mortar specimens increases linearly with time from zero until failure and (2) a constant compressive load applied to terracotta statues. The cumulative damage has a power-law dependence on the time to failure with identical power-law exponent $\alpha = 1/3$ for loading conditions (1) and (2). In this research, it is shown that this dependence is in agreement with the solutions obtained in laboratory experiments using electrical resistance measurements. Furthermore, identical solutions for cases (1) and (2) provide the theoretical support to estimate the terracotta statues' residual lifetime by correlating in situ electrical measurements with laboratory measurements. Thus, the presented methodology should have

properly illustrated the need for damaged artworks and more in general for cultural heritage to have a planned preventative maintenance.

Moreover, the results of compression tests carried out on cylindrical specimens of sculpture and building decoration materials have been analyzed considering the stability of the loading process and the relationship between absorbed and released energy during the post-peak phase. The use of the circumferential strain as controlling parameter of the compression tests permits the post-peak branch to be detected, also for a very brittle material such as Luserna stone. This is fundamental to derive the scale-invariant overlapping constitutive law and to define the structural brittleness. The results show also how the number of AE events in the post-peak regime is proportional to the released energy, that is evaluated as the difference between the elastic strain energy at the peak load and the energy absorbed by the crushing process. The AE results obtained from compression prove that the variation of the AE parameters during the loading process strictly depends on the specimen damage: a decrease in the frequency coupled to low RA values suggest a Mode I crack propagation, whereas a decrease in the frequency coupled to high RA values are obtained in case of Mode II crack propagation. All the monitored damage processes display an increase of AE signal energy content approaching the final failure.

In conclusion, the stability of the decorated surface structural supports and artworks was investigated by innovative Acoustic Emission (AE) and non-destructive methods already experimentally tested in the field of artistic and monumental Italian cultural heritage. The AE techniques allowed to assess separations, defects and damage phenomena regarding the decorated surfaces and the masonry supports. Innovative monitoring methods allowed to distinguish a

well preserved artwork in comparison to a damaged one.

The data collected during the experimental tests conducted in situ were interpreted with Fracture Mechanics models and methodologies.

The research activity has shown how the design of the most appropriate monitoring technique turns out to be crucial for the historical structure as well as the selection of the most suitable repair products in terms of durability and compatibility.

References

Accornero, F., Invernizzi, S., Lacidogna, G., and Carpinteri, A., Acoustic Emission and damage analysis of decorated surface structural supports, *Proceedings of the 19th European Conference on Fracture*, Kazan, Russia, 2012.

Accornero, F., Invernizzi, S., Lacidogna, G., and Carpinteri, A., Stability assessment of masonry arches by evolutionary fracturing process analysis, *Proceedings of the 21th Congress of the Italian Society of Theoretical and Applied Mechanics*, Torino, Italy, 2013.

Aggelis, D.G., *Characterization of Advanced Structural Materials by Acoustic Emission Indices*, Nova Science Publishers Inc, 2011a.

Aggelis, D.G., Classification of cracking mode in concrete by acoustic emission parameters, *Mechanics Research Communications*, **39**:153-157, 2011b.

Aggelis, D.G., Soulioti, D.V., Sapouridis, N., Barkoula, N.M., Paipetis, A.S., and Matikas, T.E., Acoustic emission characterization of the fracture process in fibre reinforced concrete, *Construction and Building Materials*, **25**:4126-4131, 2011c.

Aggelis, D.G., Tsimpris, N., Chai, H.K., Shiotani, T., and Kobayashi, Y., Numerical simulation of elastic waves for visualization of defects, *Construction and Building Materials*, **25**(4):1503-1512, 2011d.

Aggelis, D.G., Barkoula, N.M., Matikas, T.E., and Paipetis, A.S., Acoustic structural health monitoring of composite materials: Damage identification and evaluation in cross ply laminates using Acoustic Emission and ultrasonics, *Composites Science and Technology*, **72**:1127-1133, 2012a.

Aggelis, D.G., Leonidou, E., and Matikas, T.E., Subsurface crack determination by one-sided ultrasonic measurements, *Cement and Concrete Composites*, **34**:140-146, 2012b.

Aggelis, D.G., and Matikas, T.E., Effect of plate wave dispersion on the acoustic emission parameters in metals, *Computers and Structures*, **98-99**:17-22, 2012c.

Aggelis, D.G., Mpalaskas, A.C., Ntalakas, D., and Matikas, T.E., Effect of wave distortion on acoustic emission characterization of cementitious materials, *Construction and Building Materials*, **35**:183-190, 2012d.

Aggelis, D.G., Shiotani, T., Papacharalampopoulos, A., and Polyzos, D., The influence of

propagation path on acoustic emission monitoring of concrete, *Structural Health Monitoring*, **11**:359-366, 2012e.

Aggelis, D.G., Soulioti, D.V., Barkoula, N.M., Paipetis, A.S., and Matikas, T.E., Influence of fiber chemical coating on the acoustic emission behavior of steel fiber reinforced concrete, *Cement and Concrete Composites*, **34**:62-67, 2012f.

Akaike, H., Markovian representation of stochastic processes and its application to the analysis of autoregressive moving average processes, *Annals of the Institute of Statistical Mathematics*, **26**:363-387, 1974.

Aki, A., A probabilistic synthesis of precursory phenomena, *Earthquake Prediction: An International Review*, M. Ewing Series (D. W. Simpson and P. G. Richards, Eds.), **4**:566-574, 1981.

Aki, K., and Richards, P., *Quantitative Seismology Theory and Methods*, W.H. Freeman, 1980.

Alessi, G., *Libro dei Misteri*, Anastatic Copy. Bologna, 1974.

Anzani, A., Binda, L., Carpinteri, A., Lacidogna, G., and Manuello, A., Evaluation of the repair on multiple leaf stone masonry by acoustic emission, *Materials and Structures*, **41**:1169-1189, 2008.

Anzani, A., Binda, L., Carpinteri, A., Invernizzi, S., and Lacidogna, G., A multilevel approach for the damage assessment of historic masonry towers, *Journal of Cultural Heritage*, **11**:459-470, 2010.

Balageas, D., Fritzen, C.P., and Güemes, A., *Structural Health Monitoring*, Wiley, 2010.

Boller, C., Chang F.K., and Fujino, Y., *Encyclopedia of Structural Health Monitoring*, Wiley, 2009.

Bolt, B.A., *Earthquakes*, W.H. Freeman, 1978.

Botvina, L.R., Damage evolution on different scale levels, *Physics of the Solid Earth*, **47**:859-872, 2011.

Botvina, L.R., Shebalin, P.N., and Oparina I.B., (2001) A mechanism of temporal variation of seismicity and Acoustic Emission prior to macrofailure, *Doklady Physics*, **46**:119-123, 2001.

Bridgman, P.W., The effect of homogeneous mechanical stress on the electrical resistance of crystals, *Physical Review*, **42**, 1932.

Bruneau, M., and Potel, C., *Materials and Acoustics Handbook*, Wiley, 2009.

Carpinteri, A., Size effects on strength, toughness, and ductility, *Journal of Engineering Mechanics*, **115**:1375-92, 1989.

Carpinteri, A., Scaling laws and renormalization groups for strength and toughness of disordered materials, *International Journal of Solids and Structures*, **31**:291-302, 1994.

Carpinteri, A., *Structural Mechanics Fundamentals*, Taylor & Francis, 2013.

Carpinteri, A., and Pugno, N., Fractal fragmentation theory for shape effects of quasi-brittle materials in compression, *Magazine of Concrete Research*, **54**:473-480, 2002.

Carpinteri, A., Lacidogna, G., and Pugno, N., Time-scale effects on acoustic emission due to elastic waves propagation in monitored cracking structures, *Physical Mesomechanics*, **8**:77-80, 2005.

Carpinteri, A., and Lacidogna, G., Structural Monitoring and Integrity Assessment of Medieval Towers, *Journal of Structural Engineering ASCE*, **11**:1681-1690, 2006a.

Carpinteri, A., Lacidogna, G., and Pugno, N., Richter's laws at the laboratory scale interpreted by Acoustic Emission, *Magazine of Concrete Research*, **58**:619-625, 2006b.

Carpinteri, A., and Lacidogna, G., Damage evolution of three masonry towers by Acoustic Emission, *Engineering Structures*, **29**:1569-1579, 2007a.

Carpinteri, A., Invernizzi, S., and Lacidogna, G., Structural assessment of a XVII Century masonry vault with AE and numerical techniques, *International Journal of Architectural Heritage*, **1**(2):214-226, 2007b.

Carpinteri, A., Lacidogna, G., Niccolini, G., Acoustic Emission monitoring of medieval towers considered as sensitive earthquake receptors, *Natural Hazards and Earth System Sciences*, **1**:1-11, 2007c.

Carpinteri, A., Lacidogna, G., and Pugno N., Structural damage and life-time assessment by Acoustic Emission monitoring, *Engineering Fracture Mechanics*, **74**:273-289, 2007d.

Carpinteri, A., Invernizzi S., ,Lacidogna, G., Manuello, A., and Binda, L., Stability of the vertical bearing structures of the Syracuse Cathedral: experimental and numerical evaluation, *Materials and Structures*, **42**(7):877-888, 2008a.

Carpinteri, A., Lacidogna, G., Niccolini, G., and Puzzi, S., Critical defect size distributions in concrete structures detected by the acoustic emission technique, *Meccanica*, **43**:349-363, 2008b.

Carpinteri, A., Lacidogna, G., and Puzzi, S., Prediction of cracking evolution in full scale structures by the b-value analysis and Yule statistics, *Physical Mesomechanics*, **11**:260-271, 2008c.

Carpinteri, A., and Lacidogna, G., *Acoustic Emission and Critical Phenomena from Structural Mechanics to Geophysics*, Taylor & Francis, 2008d.

Carpinteri, A., Corrado, M., Mancini, G., and Paggi, M., The overlapping crack model for uniaxial and eccentric concrete compression tests, *Magazine of Concrete Research*, **61**:745-757, 2009a.

Carpinteri, A., Invernizzi, S., and Lacidogna, G., Historical brick-masonry subjected to double flat-jack test: Acoustic emissions and scale effects on cracking density, *Construction and Building Materials*, **23**:2813-2820, 2009b.

Carpinteri, A., Lacidogna, G., Invernizzi, S., Manuello, A., and Binda, L., Stability of vertical bearing structures of the Syracuse Cathedral: Experimental and numerical evaluation, *Materials and Structures*, **42**:877-888, 2009c.

Carpinteri, A., Lacidogna, G., and Manuello, A., The *b*-value analysis for the stability investigation of the ancient Athena temple in Syracuse, *Strain*, **47**:e243-e253, 2009d.

Carpinteri, A., Lacidogna, G., and Niccolini, G., Fractal analysis of damage detected in concrete structural elements under loading, *Chaos, Solitons and Fractals*, **42**:2047-2056, 2009e.

Carpinteri, A., Lacidogna, G., and Puzzi, S., From criticality to final collapse: Evolution of the b-value from 1.5 to 1.0, *Chaos, Solitons and Fractals*, **41**:843-853, 2009f.

Carpinteri, A., Cardone, F., and Lacidogna, G.,. Energy emissions from failure phenomena: Mechanical, electromagnetic, nuclear, *Experimental Mechanics*, **50**:1235–1243, 2010a.

Carpinteri, A., Invernizzi, S., Lacidogna, G., and Manuello, A., Preservation, safeguard and valorization of masonry decorations in the architectural historical heritage of Piedmont (Italy), *Advanced Materials Research*, **133-134**:1015-1020, 2010b.

Carpinteri, A., Corrado, M., and Paggi, M., An analytical model based on strain localization for the study of size-scale and slenderness effects in uniaxial compression tests, *Strain*, **47**:351-362, 2011a.

Carpinteri, A., Lacidogna, G., and Manuello A., The *b*-value analysis for the stability investigation of the ancient Athena Temple in Syracuse, *Strain*, **47**:243-253, 2011b.

Carpinteri, A., Lacidogna, G., Manuello, A., and Niccolini, G., A study on the structural stability of the Asinelli Tower in Bologna, *Proceedings of the 20th Congress of the Italian Society of Theoretical and Applied Mechanics*, Bologna, Italy, 2011c.

Carpinteri, A., Lacidogna, G., and Niccolini, G., Damage analysis of reinforced concrete buildings by the acoustic emission technique, *Structural Control & Health Monitoring*, **18**:660-673, 2011d.

Carpinteri, A., Corrado, M., and Lacidogna, G., Three different approaches for damage domain characterization in disordered materials: Fractal energy density, *b*-value

statistics, renormalization group theory, *Mechanics of Materials*, **53**:15-28, 2012a.

Carpinteri, A., Invernizzi, S., Lacidogna, G., and Accornero, F., Acoustic Emission monitoring of frescos degradation in a XVII Century chapel of the Sacred Mountain of Varallo (Italy), *Structural Analysis of Historical Constructions*, Jerzy Jasinko (ed), Wroclaw, Poland, 2012b.

Carpinteri, A., Xu, J., Lacidogna, G., and Manuello, A., Reliable onset time determination and source location of acoustic emissions in concrete structures, *Cement & Concrete Composites*, **34**:529-537, 2012c.

Carpinteri, A., Corrado, M., and Lacidogna, G., Heterogeneous materials in compression: Correlations between absorbed, released and acoustic emission energies, *Engineering Failure Analysis*, **33**:236-250, 2013a.

Carpinteri, A., Lacidogna, G., and Accornero, F., Evolution of fracturing process in masonry arches, *Journal of Structural Engineering ASCE*, In Print, 2013b.

Carpinteri, A., Lacidogna, G., Accornero, F., Mpalaskas, A.C., Matikas, T.E., and Aggelis, D.G., Influence of damage in the acoustic emission parameters, *Cement & Concrete Composites*, **44**:9-16, 2013c.

Carpinteri, A., Lacidogna, G., Invernizzi, S., and Accornero, F., The Sacred Mountain of Varallo renaissance complex in Italy: Damage analysis of decorated surfaces and structural supports, *Meccanica*, In Print, 2013d.

Carpinteri, A., Lacidogna, G., Invernizzi, S., and Accornero, F., The Sacred Mountain of Varallo in Italy: Seismic risk assessment by Acoustic Emission and structural numerical models, *The Scientific World Journal*, In Print, 2013e.

Carpinteri, A., Lacidogna, G., Manuello, A., Niccolini, G., and Accornero, F., Correlation between Acoustic Emission and Seismicity in the Sacred Mountain of Varallo Renaissance Complex in Italy, *Proceedings of the 13th International Conference on Fracture*, Beijing, China, 2013f.

Chen, B., and Liu, J., Damage in carbon fiber-reinforced concrete, monitored by both electrical resistance measurement and acoustic emission analysis, *Construction and Building Materials*, **22**, 2008.

Colombo, S., Main, I.G., and Forde, M.C., Assessing damage of reinforced concrete beam using ‘‘*b*-value’’ analysis of acoustic emission signals, *Journal of Materials in Civil Engineering ASCE*, **15**:280-286, 2003.

Cox, S.J.D., and Meredith, P.G., Microcrack formation and material softening in rock measured by monitoring acoustic emission, *International Journal of Rock Mechanics and Mining Sciences and Geomechanics Abstracts*, **30**, 1993.

De Filippis, E., *Sacro Monte of Varallo,* Borgosesia, 2009.

De Filippis, E., Tulliani, J.M., Sandrone, R., Scarzella, P., Palmero, P., Lombardi Sertorio, C., and Zerbinatti, M., Analisi degli intonaci della Cappella del Calvario al Sacro Monte di Varallo, *ARKOS*, **12**:38-45, 2005.

Di Battista, E., Lacidogna, G., Invernizzi, S., Accornero, F., and Carpinteri, A., Acoustic Emission and fracture energy dissipation in notched concrete beams subjected to three-point bending tests, *Proceedings of the 21th Congress of the Italian Society of Theoretical and Applied Mechanics,* Torino, Italy, 2013.

Enoki, M., and Kishi, T., Theory and analysis of deformation moment tensor due to microcracking, *International Journal of Fracture*, **38**:295-310, 1988.

Ferrara, G., and Gobbi, M.E., Strain softening of concrete under compression, *Report to RILEM Committee 148 SCC,* ENEL-CRIS Laboratory, Milano, Italy, 1995.

Grassberger, P., and Procaccia, I., Characterization of strange attractors, *Physical Review Letters*, **50**:346-349, 1983.

Gregori, G.P., and Paparo, G., Acoustic Emission: A diagnostic tool for environomental sciences and for non destructive tests (with a potential application to gravitational antennas), in: *Metereological and Geophysical Fluid Dynamics*, Schroeder, Bremen, 2005.

Gregori, G.P., Paparo, G., Poscolieri, G., and Zanini, A., Acoustic Emission and released seismic energy, *Natural Hazards and Earth System Sciences*, **5**:777-782, 2005.

Grosse, C., Reinhardt, H., and Dahm, T., Localization and Classification of Fracture Types in Concrete with Quantitative Acoustic Emission Measurement Techniques, *NDT&E International*, **30**(4):223-230, 1997.

Grosse, C.U., and Ohtsu, M., *Acoustic Emission Testing*, Springer, 2008.

Grossi, C.M., Esbert, R.M., Suarez del Rio, L.M., Montoto, M., and Laurenzi-Tabasso, M., Acoustic Emission monitoring to study sodium sulphate crystallization in monumental porous carbonate stones, *Studies in Conservation*, 42:115-125, 1997.

Guarino, A., Garciamartin, A., and Ciliberto, S., An experimental test of the critical behavior of fracture precursors, *European Physical Journal B*, **6**, 1998.

Hall, C., and Hoff, W.D., Rising damp: Capillary rise dynamics in walls, *Proceedings of the Royal Society A*, **463**:1871-1884, 2007.

Hanzlicek, T., Steinerova, M., Straka, P., Perna, I., Siegl, P., and Svarcova, T., Reinforcement of the terracotta sculpture by geopolymer composite, *Materials and Design*, **30**, 2009.

Hirata, T., A correlation between b-value and the fractal dimension of earthquakes, *Journal of Geophysical Research*, **94**:7507-7514, 1989.

Hudson, J.A., Brown, E.T., and Fairhurst, C., Shape of the complete stress-strain curve for rock, in: E.J. Cording (Ed.), *Stability of Rock Slopes (Proceedings of the 13th Symposium on Rock Mechanics)*, American Society of Civil Engineers, New York, 1972.

Invernizzi, S., Lacidogna, G., Manuello, A., and Carpinteri, A., AE monitoring and numerical simulation of a 2-span model masonry arch bridge subjected to pier scour, *Strain*, **47**(2):158-169, 2011.

Jansen, D.C., and Shah, S.P., Effect of length on compressive strain softening of concrete, *Journal of Engineering Mechanics*, **123**:25-35, 1997.

Johansen, A., and Sornette, D., Critical ruptures, *European Physical Journal B*, **18**, 2000.

Kachanov, L.M., *Introduction to Continuum Damage Mechanics*, Martinus Nijhoff, 1986.

Kaiser, J., *An Investigation into the Occurrence of Noises in Tensile Tests, or a Study of Acoustic Phenomena in Tensile Test*, PhD Dissertation, Technical University of Munchen, 1950.

King, G.C.P., The accommodation of large strains in the upper lithosphere of the Earth, *Pure and Applied Geophysics*, **121**:761-815, 1983.

Kordatos, E.Z., Aggelis, D.G., and Matikas, T.E., Monitoring mechanical damage in structural materials using complimentary NDE techniques based on thermography and Acoustic Emission, *Composites Part B: Engineering*, **43**:2676-2686, 2012.

Kotsovos, M.D., Effect of testing technique on the post-ultimate behaviour of concrete in compression, *Materials and Structures*, **16**:3-12, 1983.

Krajcinovic. D., *Damage Mechanics*, Elsevier, 1996.

Krajcinovic, D., and Rinaldi, A., Statistical Damage Mechanics, *Journal of Applied Mechanics*, **72**, 2005.

Kurz, J.H., Finck, F., Grosse, C.U., and Reinhardt, H.W., Stress drop and stress redistribution in concrete quantified over time by the b-value analysis, *Structural Health Monitoring*, **5**:69-81, 2006.

Lacidogna, G., Carpinteri, A., Manuello, A., Durin, G., Schiavi, A., Niccolini, G., and Agosto, A., Acoustic and electromagnetic emissions as precursor phenomena in failure processes, *Strain*, **47**:144-152, 2011a.

Lacidogna, G., Carpinteri, A., Manuello, A., Niccolini, G., Agosto, A., and Borla, O., Acoustic emission and electrical properties of quasi-brittle materials under

compression, *Proceedings of Conference & Exposition on Experimental and Applied Mechanics SEM*, Uncasville, CT (USA), 2011b.

Lacidogna, G., Accornero, F., Corrado, M., and Carpinteri, A., Crushing and fracture energies in concrete specimens monitored by Acoustic Emission, *Proceedings of the 8th International Conference on Fracture Mechanics of Concrete and Concrete Structures FraMCoS-8*, J.G.M. Van Mier, G. Ruiz, C. Andrade, R.C. Yu and X.X. Zhang (Eds), Toledo, Spain, 2013a.

Lacidogna, G., Invernizzi, S., Accornero, F., and Carpinteri, A., The Sacred Mountain of Varallo complex in Italy: Correlation between structural damage and local seismicity, *Proceedings of the 21th Congress of the Italian Society of Theoretical and Applied Mechanics*, Torino, Italy, 2013b.

Lagrange, J.-L., *Méchanique Analitique*, Desaint, Paris, 1788.

Lamb, H., On waves in an elastic plate, *Proceedings of the Royal Society A*, **93**:114-128, 1917.

Landis, E.N., and Shah, S.P., Frequency-dependent stress wave attenuation in cement-based materials, *Journal of Engineering Mechanics*, **121**:737-743, 1995.

Lemaitre, J., and Chaboche, J.L., *Mechanics of Solid Materials*, Cambridge University Press, 1990.

Lemaitre, J., and Dufailly, J., Damage measurements, *Engineering Fracture Mechanics*, **28**, 1987.

L'Hermite, R.G., Volume change of concrete, *Proceedings of the 4th International Symposium on the Chemistry of Cement*, Washington D.C., United States, 1960.

Lockner, D., The role of acoustic emissions in the study of rock fracture, *International Journal of Rock Mechanics and Mining Sciences and Geomechanics Abstracts*, **7**, 1993.

Lockner, D.A., Byerlee, J.D., Kuksenko, V., Ponomarev, A. and Sidorin, A., Quasi static fault growth and shear fracture energy in granite, *Nature*, **350**:39-42, 1991.

Loland, K.E., Continuous damage model for load-response estimation of concrete, *Cement and Concrete Research*, **10**:395-402, 1989.

Ministero delle Infrastrutture, Decreto 14 Gennaio 2008: Norme Tecniche per le Costruzioni, *Gazzetta Ufficiale della Repubblica Italiana*, **29**, 2008.

Main, I.G., A modified Griffith criterion for the evolution of damage with a fractal distribution of crack lengths: Application to seismic event rates and *b*-values, *Geophysical Journal International*, **107**:353-362, 1991.

Main, I.G., Damage mechanics with long-range interactions: Correlation between the seismic b-value and the two point correlation dimension, *Geophysical Journal International*, **111**:531-541, 1992.

Main, I.G., A damage mechanics model for power-law creep and earthquake aftershock and foreshock sequences, *Geophysical Journal International*, **142**:151-161, 2000.

Maine, J., *DIANA. Finite Element Analysis User's Manual. Release 9.4.4.*, TNO DIANA bv, Delft, 2012.

Mandelbrot, B., *The Fractal Geometry of Nature*, W.H. Freeman, 1982.

Manthei, G., Eisenblätter, J., and Dahm, T., Moment tensor evaluation of Acoustic Emission sources in salt rock, *Construction and Building Materials*, **15**:297-309, 2001.

Mastrangelo, C.H., Hsu, C.H., Mechanical stability and adhesion of microstructures under capillary forces - Part II: Experiments, *Journal of Micro-electromechanical Systems*, **2**(1):44-55, 1993.

Niccolini, G., Carpinteri, A., Lacidogna, G., and Manuello, A., Acoustic Emission monitoring of the Syracuse Athena Temple: Scale invariance in the timing of ruptures, *Physical Review Letters*, **106**:108503, 2011.

Niccolini, G., Borla, O., Lacidogna, G., Schiavi, A., and Carpinteri, A., Failure precursors in rocks and concrete, *Proceedings of the 19th European Conference on Fracture*, Kazan, Russia, 2012.

Niccolini, G., Borla, O., Accornero, F., Lacidogna, G., and Carpinteri, A., Mechanical damage of historical terracotta statues analyzed by electrical resistance measurements, *Proceedings of the 21th Congress of the Italian Society of Theoretical and Applied Mechanics*, Torino, Italy, 2013a.

Niccolini, G., Borla, O., Accornero, F., Lacidogna, G., and Carpinteri, A., Scaling in damage by electrical resistance measurements, *International Journal of Damage Mechanics*, In Print, 2013b.

Occhi Villavecchia, G., *Le Tecniche Acustiche per la Diagnostica ed il Monitoraggio dei Dipinti Murali*, PhD Dissertation, La Sapienza University of Rome, 2013.

Ohno, K., and Ohtsu, M., Crack classification in concrete based on Acoustic Emission, *Constructions and Building Materials*, **24**:2339-2346, 2010.

Ohtsu, M., Acoustic Emission characteristics in concrete and diagnostic applications, *Journal of Acoustic Emission*, **6**(2):99-108, 1987.

Ohtsu, M., Simplified moment tensor analysis and unified decomposition of Acoustic Emission source: Application to in-situ hydrofracturing test, *Journal of Geophysical Research*, **96**:6211-6221, 1991.

Ohtsu, M., The history and development of acoustic emission in concrete engineering, *Magazine of Concrete Research*, **48**:321-330, 1996.

Ohtsu, M., Basics of Acoustic Emission and applications to concrete engineering, *Materials Science Research International*, **4**(3):131-140, 1998.

Ohtsu, M., and Ono, K., A generalized theory of Acoustic Emission and Green's functions in half space, *Journal of Acoustic Emission*, **3**(1):124-133, 1984.

Ohtsu, M., and Watanabe, H., Quantitative damage estimation of concrete by Acoustic Emission, *Construction and Building Materials*, **15**:217-224, 2001.

Ohtsu, M., Uchida, M., Okamoto, T., and Yuyama, S., Damage assessment of reinforced concrete beams qualified by Acoustic Emission, *ACI Structural Journal*, **99-**S42:411-417, 2002.

Okubo, S., and Nishimatsu, Y., Uniaxial compression testing using a linear combination of stress and strain as the control variable, *International Journal of Rock Mechanics and Mining Sciences and Geomechanics Abstracts*, **22**:323-330, 1985.

Paipetis, A.S., and Aggelis, D.G., Damage Assessment in Fibrous Composites Using Acoustic Emission, in: Wojciech Sikorski (Ed.), *Acoustic Emission*, InTech, 2012.

Rao, M.V.M.S., and Prasanna Lakshmi, K.J., Analysis of b-value and improved b-value of acoustic emissions accompanying rock fracture, *Current Science*, **89**:1577-1582, 2005.

Richter, C.F., *Elementary Seismology*, W.H. Freeman, 1958.

RILEM 50-FMC Committee, Determination of the fracture energy of mortar and concrete be means of three-point bend tests on notched beams, *Materials and Structures*, **18**:286-90, 1986.

RILEM Technical Committee TC212-ACD: Ohtsu, M., Shiotani, T., Shigeishi, M., Kamada, T., Yuyama, S., Watanabe, T., Suzuki, T., Van Mier, J.G.M., Vogel, T., Grosse, C., Helmerich, R., Forde, M.C., Moczko, A., Breysse, D., Ivanovich, S.A., Sajna, A., Aggelis, D., and Lacidogna, G., Acoustic Emission and related NDE techniques for crack detection and damage evaluation in concrete: Measurement method for acoustic emission signals in concrete, *Materials and Structures*, **43**:1177-1181, 2010a.

RILEM Technical Committee TC212-ACD: Ohtsu, M., Shiotani, T., Shigeishi, M., Kamada, T., Yuyama, S., Watanabe, T., Suzuki, T., Van Mier, J.G.M., Vogel, T., Grosse, C., Helmerich, R., Forde, M.C., Moczko, A., Breysse, D., Ivanovich, S.A., Sajna, A., Aggelis, D., and Lacidogna, G., Acoustic Emission and related NDE techniques for crack detection and damage evaluation in concrete: Test method for damage qualification of reinforced concrete beams by Acoustic Emission, *Materials and Structures*, **43**:1183-1186, 2010b.

RILEM Technical Committee TC212-ACD: Ohtsu, M., Shiotani, T., Shigeishi, M., Kamada, T., Yuyama, S., Watanabe, T., Suzuki, T., Van Mier, J.G.M., Vogel, T., Grosse, C., Helmerich, R., Forde, M.C., Moczko, A., Breysse, D., Ivanovich, S.A., Sajna, A., Aggelis, D., and Lacidogna, G., Acoustic Emission and related NDE techniques for crack detection and damage evaluation in concrete: Test method for classification of active cracks in concrete by Acoustic Emission, *Materials and Structures*, **43**:1187-1189, 2010c.

Rundle, J.B., Turcotte, D.L., Shcherbakov, R., Klein, W., and Sammis, C., Statistical physics approach to understanding the multiscale dynamics of earthquake fault systems, *Reviews of Geophysics*, **41**:1-30, 2003.

Russell, J.E., and Hoskins, E.R., Correlation of electrical resistivity of dry rock with cumulative damage, *Proceedings of the 11th U.S. Symposium on Rock Mechanics*, Berkeley, 1969.

Scholey, J.J., Wilcox, P.D., Wisnom, M.R., and Friswell, M.I., Quantitative experimental measurements of matrix cracking and delamination using Acoustic Emission, *Composites: Part A*, **41**:612–623, 2010.

Scholz, C.H., The frequency-magnitude relation of microfracturing in rock and its relation to earthquakes, *Bulletin of the Seismological Society of America*, **58**:399-415, 1968.

Sheng, D., Gens, A., Fredlund, D.G., and Sloan, S.W., Unsaturated soils: From constitutive modelling to numerical algorithms, *Computers and Geotechnics*, **35**:810-824, 2008.

Shiotani, T., Evaluation of long-term stability for rock slope by means of acoustic emission technique, *NDT&E International*, **39**(3):217-228, 2006.

Shiotani, T., Fujii, K., Aoki, T., and Amou, K., 1994. Evaluation of Progressive Failure using AE Sources and Improved b-value on Slope Model Tests, *Progress in Acoustic Emission*, **7**:529-534, 1994.

Shiotani, T., Li, Z., Yuyama, S., and Ohtsu, M., Application of the AE improved *b*-value to quantitative evaluation of fracture process in concrete materials, *Journal of Acoustic Emission*, **19**:118-133, 2001.

Shiotani, T., Aggelis, D.G., and Makishima, O., Global monitoring of large concrete structures using acoustic emission and ultrasonic techniques, *Journal of Bridge Engineering ASCE*, **14**(3):188-192, 2009.

Soulioti, D., Barkoula, N.M., Paipetis, A., Matikas, T.E., Shiotani, T., and Aggelis, D.G., Acoustic emission behavior of steel fibre reinforced concrete under bending, *Construction and Building Materials*, **23**:3532-3536, 2009.

Sornette, D., Leung, K.T., and Andersen, J.V., Conditions for abrupt failure in the democratic fiber bundle model, *Physical Review Letters***, 80,** 1998.

Sun, B., and Guo, Y., High-cycle fatigue damage measurement based on electrical resistance change considering variable electrical resistivity and uneven damage, *International Journal of Fatigue*, **26**, 2004.

Turcotte, D.L., *Fractals and Chaos in Geology and Geophysics*, Cambridge University Press, 1997.

Turcotte, D.L., Newman, W.I., and Shcherbakov, R., Micro and macroscopic model for rock fracture, *Geophysical Journal International*, **152**, 2002.

Turcotte, D.L., and Shcherbakov, R., Damage and self-similarity in fracture, *Theoretical and Applied Fracture Mechanics*, **39**, 2003.

Van Mier, J.G.M., *Strain softening of concrete under multiaxial compression*, PhD Dissertation, Eindhoven University of Technology, The Netherlands, 1984.

Watanabe, T., Hosomi, M., Yuno, K., and Hashimoto, C., Quality evaluation of shotcrete by acoustic emission, *Construction and Building Materials*, **24**:2358–2362, 2010.

Weiss, J., Fracture and fragmentation of ice: a fractal analysis of scale invariance, *Engineering Fracture Mechanics*, **68**:1975-2012, 2001.

Weiss, J., and Marsan, D., Three-dimensional mapping of dislocation avalanches: clustering and space/time coupling, *Science*, **299**:89-92, 2003.

Zapperi, S., Ray, P., Stanley, H.E., and Vespignani, A., First-order transition in the breakdown of disordered media, *Physical Review Letters*, **78**, 1997.